# DEVELOPMENT OF THE DUAL DC SQUID MAGNETOMETER AND AGING IN NON-EQUILIBRIUM DYNAMICS

A Thesis Submitted to the School of Graduate Studies and Research

in Partial Fulfillment of the

Requirements for the Degree

Master of Science

Christina M. Rost

Indiana University of Pennsylvania

May 2012

Indiana University of Pennsylvania
School of Graduate Studies and Research
Department of Physics

We hereby approve the thesis of

Christina M. Rost

Candidate for the degree of Master of Science

_____ _____

Gregory G. Kenning, Ph.D.
Professor of Physics, Advisor

_____ _____

A. J. Haija, Ph.D.
Professor of Physics

_____ _____

Majid Karimi, Ph.D.
Professor of Physics

_____ _____

Devki N. Talwar, Ph.D.
Professor of Physics

ACCEPTED

_____ _____

Timothy Mack, Ph.D.
Dean
School of Graduate Studies and Research

Title: Development of the Dual DC SQUID Magnetometer and Aging in Non-Equilibrium Dynamics

Author: Christina M. Rost

Thesis Committee Chair: Dr. Gregory Kenning

Thesis Committee Members: Dr. Devki N. Talwar
Dr. Majid Karimi
Dr. A.J. Haija

The metallic spin-glass CuMn has been prepared for studies pertaining to the 'End of Aging'. A highly specialized machine known as a dual DC SQUID magnetometer has been developed and assembled to perform low temperature measurements of the thermoremanent magnetization (TRM) of this material. The spin glass is cooled below its glass transition temperature and held in an external field for some waiting time, where aging takes place. After the field is cut to zero, the TRM decay is recorded for long measurement times. This process is repeated for various measurement temperatures and waiting times, and then analyzed under the premise of system improvement and potential determination of the 'end of aging'. All experiments have been completely automated using National Instruments LabVIEW interfacing.

ACKNOWLEDGEMENTS

I would sincerely like to thank my parents, brother, friends and fiancé for all of their love and support.

I would like to express the highest appreciation for my advisor, Dr. Gregory Kenning, for his guidance and undying enthusiasm for physics.

I would also like to extend my gratitude to all members, past and present, of the IUP Physics Department for their generosity, support and acceptance. Thank you!

TABLE OF CONTENTS

1. INTRODUCTION…….…….....1
2. THEORETICAL AND EXPERIMENTAL CONCEPTS……4
2.1. Ferromagnetism, Antiferromagnetism and Spin Glasses……..4
2.2. Theoretical Models……...10
2.3. Experimental Concepts of Aging in Spin Glasses……25
3. DEVELOPMENT OF THE EXPERIMENTAL APPARATUS……30
3.1. SQUIDs and Signal Control…….32
3.2. Temperature Control…….37
3.2.1. Temperature Controller……...37
3.2.2. Temperature Sensors……..38
3.2.3. Heat Supply Circuit……...39
3.2.4. Sapphire Rod……40
3.3. Magnetic Field……..43
3.4. Data Collection…….47
3.5. Helium Dewar and Level Detection…….47
3.6. Automation and Programming…….51
3.6.1. Interface Set-Up……51
3.6.2. Long Time TRM Decay Measurement Program……..53
3.6.3. Standard TRM Measurement Program…….…....59
4. DATA……...…...61
4.1. Sample Characterization…….…..62
4.2. Initial Data Output…….…...64
5. CONCLUSIONS……...……..73

REFERENCES……..75

APPENDICES……...77

Appendix A - Magnetometer Drawings……..……...77

Appendix B - Automation Programming…….…….…….82

LIST OF TABLES

3.1 Pin Assignments for Temperature Control System……..…….37

3.2 List of GPIB Addresses and Aliases…….…….……46

LIST OF FIGURES

2.1 The left image is ferromagnetic alignment, the right image is antiferromagnetic……..….5

2.2 Metallic Spin Glass (Heisenberg Model). Sketch of magnetic ions randomly distributed throughout a metallic host lattice…….……....7

2.3 Plot of the RKKY interaction……..8

2.4 Representation of antiferromagnetic Ising spin system with frustration……..…...9

2.5 The image on the left is a simulation of a ferromagnetic system. The right is an antiferromagnetic system. These images were produced through a simulation in zero-field for this thesis using *Java Simulations for Statistical Physics*- an open source physics project……11

2.6 Plot of the "self-consistent transcendental function", Eq. 2.11, in zero-field. The intersection between the two functions mark possible solutions, both stable and unstable [10]…….12

2.7 The matrix structure during the replica symmetry breaking process introduced by Parisi [11]. From left to right: 0 step symmetry breaking, 1 step symmetry breaking, 2 step symmetry breaking. All diagonal elements are zero.…….…...17

2.8 Probability distribution P(q) for different magnetic phases [11]. (a) Paramagnetism (b) Ferromagnetism (c) Spin Glass.……...…….....20

2.9 Hierarchical structure of spin glass states [8,12]…….……..21

2.10 Hierarchical structure of the barrier model [12]…….……...…23

2.11 Energy landscape with metastable states of magnetization MFC, separated by barriers [11]……..……...…….……..24

2.12 $M=M_{FC}$ and M=0 manifolds [11]……...25

2.13 S(t) graph displays curve maxima denoting the location of $t_w$ [13].……26

2.14 Different TRM scaling methods with various cooling times [16].……....28

2.15 Curve fitting to the logarithmic decay at $t>>t_w$ for various measurement temperatures below $T_g$ [14]..…….....29

3.1 Equipment Arrangement……30

3.2 Internal Dewar schematic……..…….……...31

3.3 SQUID circuitry. *Diagram borrowed from Quantum Design*……..…….34

3.4 SQUID Probe Assembly. *Diagram borrowed from Quantum Design* ……..…...…....35

3.5 Axial Gradiometers……37

3.6 Cernox 1050-SD Temperature Sensor. *Diagram adapted from LakeShore* ……..……...39

3.7 Thermal Conductivity of various materials [17]…..…….....….41

3.8 Sapphire Rod Configuration……..41

3.9 Temperature Control Connection Diagram…….…..…….42

3.10 Solenoid. The solenoid fits tightly directly over the axial gradiometers, as shown on the right.…….……..…..……...44

3.11 Current dissipation rate…….….45

3.12 Solenoid Circuit. The solenoid is connected to a twisted pair of single core wires that lead to a 5-pin military style connector above the top of the flange. Only pins 1 and 4 are used; the positive and negative lead, respectively…….....…..45

3.13 Helium Dewar……...…50

3.14 LabVIEW programming example……...……..51

3.15 GPIB Connection Arrangement……..…...52

3.16 Initialization sequence for programming using VISA control standards. Keithley multimeters appear far later in the program due to GUI organization, however they still initialize with the other equipment……..……..54

3.17 LakeShore heating protocol…….…..55

3.18 LakeShore cooling protocol……...55

3.19 The Agilents turn off the solenoid, the SQUID controller performs a global reset, the Keithleys set precision, and measurements begin…….56

3.20 Final data point measurement……....57

3.21 Long Time TRM Measurement System Interface…….…..……..58

3.21 Standard TRM measurement system interface……..59

4.1 FCZFC sample characterization……62

4.2 Plot of the de Almeida-Thouless line, corresponding to the boundary between paramagnetic and spin-glass states [19]. Stable and unstable refer to stability of replica symmetry……63

4.3 ZTRM measurement before machine adjustments……...….65

4.4 Initial TRM decay measurement after setting corrections…….....66

4.5 Fast Baseline Protocol……67

4.6 Slow Baseline Protocol……..68

4.7 S(t) curve for $0.96(0.95T_g)$ and $0.97(0.95T_g)$……....69

4.8 0.9, 0.95, 0.96, $0.97t_g$ runs……..70

4.9 Mylar Hysteresis. Top: Full Hysteresis Curve. Bottom: Magnified curve about field = 0……...……72

A.1 Full Structural Assembly……...78

A.2 Top half of magnetometer……..79

A.3 Bottom half of magnetometer……80

A.4 Close-up of pick-up coil and solenoid in G10 encasement……..……..81

B.1 Standard TRM decay program……...83

B.2 Long-time ZTRM decay program……..89

# CHAPTER 1

# INTRODUCTION

The spin glass state has been the cause for much inquiry and discussion in condensed matter physics since its discovery in 1972 [1]. Noted for its magnetically frustrated and structurally frozen disorder, the spin glass is a unique classification marked by a cusp in its susceptibility curve. This cusp is said to represent a temperature at which a second order phase transition occurs. While there are many different types of materials that exhibit spin glass (SG) properties, including but not limited to insulating, amorphous, and semiconductor spin glasses, this work focuses solely on the original subject of the discovery: the metallic spin glass.

Several models have been developed in order to describe spin glasses and their aging process. We focus on one particular model, the mean-field model. We also introduce the theoretical evolution of the spin glass phase. This is done through the introduction of the Edwards-Anderson (EA) model for a finite system [2] and the infinite-range model by Sherrington and Kirkpartick (SK) [3]; which builds upon the work of the EA model, compensating for spin interactions between larger distances. The Parisi [4] solution and its replica-symmetry-breaking (RSB) scheme details a hierarchical structure of states separated by energy barriers. Parisi's solution is believed to give the correct solution to the SK model. Unfortunately, the energy barriers between these states are infinite, making dynamic transitions between states impossible. In order to overcome this theoretical issue, a barrier model has been developed. This model makes use of the hierarchical theory of Parisi, but implements finite barrier sizes, allowing for dynamical transitions between states.

Aging is the time evolution of a dynamic system, i.e. the gradual process that takes place as a system approaches equilibrium. Experimentally, aging can be seen through decays in the thermoremanent magnetization (TRM). In a TRM measurement, the sample is cooled through its glass transition temperature in an applied magnetic field and held at a measurement temperature in the field for a waiting time, where the system ages. When the field is switched off, the spins decay towards a new equilibrium configuration. An inflection point can be seen in the response curve, roughly occurring at the time equivalent in which the sample was held in the field. This can be further confirmed through plotting the function S(t) vs. log t and observing a notable peak. Through the observation of this response, it has been determined that the spin glass holds a memory of its time spent in the field (i.e. its age). Interestingly, with a fast cooling protocol in place and well as a large measurement time, the time-dependent response function transitions into a logarithmic curve independent of the waiting time. This term indicates an 'End of Aging'. It has been noticed that as we increase the measurement temperature closer to the transition point, the quicker the curve shifts into this logarithmic term. With this knowledge in mind, we intended on making TRM decay measurements closely approaching the transition temperature, allowing us to potentially examine the "End of Aging" in an experimentally tangible amount of time. The following work illustrates the entire process; from the design and construction of the experimental apparatus to the results of the initial data output.

This thesis is organized rather non-traditionally, as it is meant to act as not only a scientific explorative but also as a guide to a very unique automated machine known as "the SQUID". Chapter 2 discusses many of the theoretical concepts behind the experiments done on spin glasses, including but not limited to ferromagnetism and antiferromagnetism, the Ising model, replica theory, aging, and the barrier model. Chapter 3 includes all pertinent information

concerning the dual DC SQUID magnetometer, i.e. “the SQUID”. This entails the physical structure of the system, including the commercially made measurement equipment and their alterations, as well as custom machined pieces. The end of Chapter 3 discusses the two automation programs built with National Instruments LabVIEW specifically for studying the aging phenomenon. The drawings and program schematics pertaining to this chapter can be found in appendices A and B, respectively. In chapter 4, we take a look at the preliminary data output of the machine, and discuss improvements made through data analysis. Finally, chapter 5 concludes the work done during this thesis project.

# CHAPTER 2

# THEORETICAL AND EXPERIMENTAL CONCEPTS

Spin glasses are a complicated system to express theoretically and even more-so to understand experimentally. A comprehension of this type of magnetic phase relies on many fundamental concepts in magnetism, thermodynamics and statistical mechanics. In this chapter, these concepts are discussed. Later, various theoretical models are introduced from the Ising model, through replica theory, to the Parisi solution and its assertion of a phenomenological barrier model. Finally, the chapter concludes with the experimental concepts pertaining to aging.

## 2.1 Ferromagnetism, Antiferromagnetism and Spin Glasses

Every physical system has magnetic properties. Each particle, atom, or molecule has an associated magnetic dipole moment that can be influenced by other dipoles in the same system or by an applied external field. How these moments interact defines the type of magnetism a system exhibits. Although there are a plethora of magnetism classifications, this section will only describe the two most common and useful in the understanding of this work: ferromagnetism and antiferromagnetism.

Ferromagnetism is the result of a quantum mechanical phenomenon known as exchange interaction, first treated by Heisenberg in 1928. J, known as the exchange constant, is derived from electron spin and the Pauli-Exclusion principle. It takes into consideration the antisymmetry of a fermion wavefunction, as well as rules of exchange symmetry. The equation for the exchange constant can be written [5] as:

$$J_{ij} = -2\frac{Vl^2 - U}{1 - l^4}. \quad (2.1)$$

Here, V is the "Coulomb integral", l is the "overlap integral", and U is the "exchange integral". If J is positive, the spins are in a parallel alignment indicating ferromagnetism. If J is negative the spin alignment is antiparallel, indicative of antiferromagnetism. A representation of this can be seen in Fig. 2.1. Thus, the general Hamiltonian, or total energy, can be written as:

$$H = -\sum_{ij} J_{ij} s_i \cdot s_j. \quad (2.2)$$

It is well known that most physical systems demonstrate preference for a lowest possible energy state. Since a ferromagnet has parallel spin alignment, both $s_i$ and $s_j$ of Eq. 2.2 would be 1, and J would be positive. Therefore the Hamiltonian would be negative, indicating a decrease in the total energy of the system. The same treatment can be applied to antiferromagnetism. The difference with antiferromagnetism is that the spins are anti-parallel, with J negative and $s_i \cdot s_j = -1$; thus the Hamiltonian is again negative.

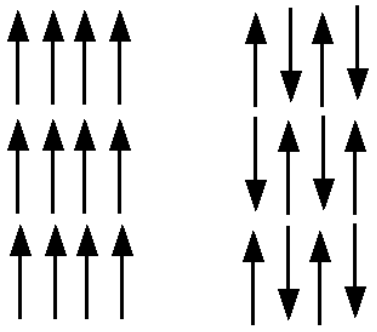

Figure 2.1: The left image is ferromagnetic alignment, the right image is antiferromagnetic.

A unique property of ferromagnetism is the existence of domains, initially discovered by Weiss in 1907 [6]. Domain formation is the result of spontaneous magnetization of small regions of

spins within a material, due to a "molecular field". One spin can induce parallel alignment in neighboring spins through the exchange interaction. If a ferromagnet is cooled below its phase transition temperature, known as the Curie temperature (see proceeding paragraphs), in zero-field, these domains will form in directions such that the net magnetization of the entire system is zero. The application of an external magnetic field can influence the change in domain boundary [7]. Domains that are already favorable in the applied field tend to drive an orientation shift of neighboring spins. If a field is strong enough, all of the domains contained within the material align, and the material is said to be saturated. This can be seen through observations of magnetization vs. field measurements. Once the field is removed, the system attempts to recover its previous equilibrium state. If the ferromagnet is "soft", domain walls will shift back such that the net magnetization reaches zero. If the ferromagnet is "hard", the domain walls remain relatively rigid, and the system is said to be permanently magnetized.

In antiferromagnetism, the spins have a 'checkered' pattern pertaining to an alternating spin-up, spin-down arrangement. This pattern tends to be a trait at low temperatures and holds no net magnetic moment. An example of the patterns formed by both ferromagnetism and antiferromagnetism, using a simulation program, can be seen in Fig. 2.5.

At high enough temperatures, the thermal energy of the system is large enough to overcome the exchange energy, $T > |J|$, destroying the alignment of the magnetic moments. In ferromagnetism, this is called the Curie temperature. Again, this can be seen through observation of the susceptibility and is governed by the Curie-Weiss law:

$$\chi = \frac{C}{T-\theta_C}, \tag{2.3}$$

where C is the material specific Curie constant, T is the temperature of the system, and $\theta_C$ is the Curie temperature. Below the Curie temperature, ferromagnetic order is present. Above this critical point, the net magnetization goes to zero and the system is paramagnetic. Analogous to the Curie temperature is the critical point in antiferromagnetism, known as the Néel temperature, with a similar relation,

$$\chi = \frac{C}{T+\theta_N}. \tag{2.4}$$

At this critical temperature, the system will go through a second order phase transition, in this case from antiferromagnetic to paramagnetic.

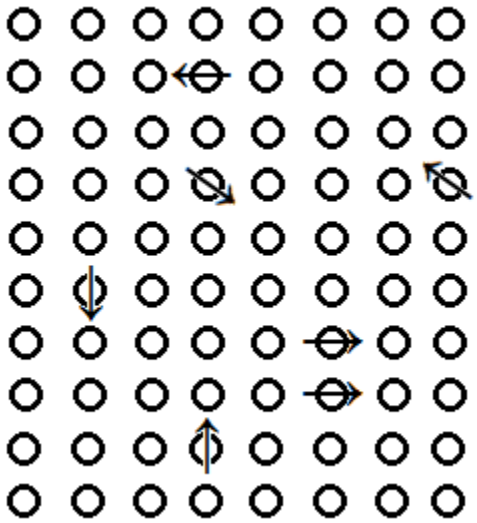

Figure 2.2: Metallic Spin Glass (Heisenberg Model). Sketch of magnetic ions randomly distributed throughout a metallic host lattice.

Spin glasses are a highly unique system characterized by magnetic frustration, quenched structural disorder, and anisotropy. There are several types of spin glasses. The 'classical' spin glass, the exclusive subject of this work, is generally an alloy with transition metal ions randomly dispersed within a noble metal host, illustrated in Fig. 2.2. Examples of such systems are CuMn, AuMn, AuFe and AgMn. Other types of spin glasses include insulating spin glasses ($Fe_xZn_{1-x}F_2$), semiconductor spin glasses ($Cd_{1-x}Mn_xTe$), and amorphous spin glasses ($a\text{-}Fe_xB_{1-x}$). Since our work pertains to the metallic spin glass, all future explanation of spin glasses should only be considered for this type of system.

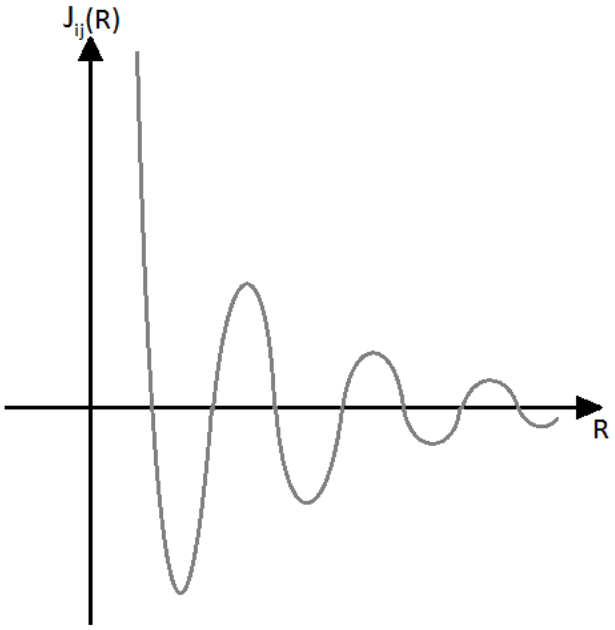


Figure 2.3: Plot of the RKKY interaction.

In a metallic spin glass, the scattering of the conduction electrons through the host material induces a spin polarization of neighboring electrons, causing long range, oscillatory (flipping between ferromagnetic and antiferromagnetic bonds) exchange interactions. This exchange

interaction is known as the RKKY interaction. The RKKY (Ruderman-Kittel-Kasuya-Yoshida) interaction is an indirect exchange characterized by a coupling coefficient (i.e. exchange constant), J, of the form [8]:

$$J(\vec{R}) = J_0 \frac{\cos(2k_F R + \emptyset_0)}{(k_F R)^3}; \tag{2.5}$$

$J_0$ and $\varphi_0$ are constants, and $k_F$ is the Fermi wave number of the host metal. Depending on the distance between ion pairs, the coupling function may be positive or negative, indicating ferromagnetic or antiferromagnetic bonds, respectively.

This oscillatory effect between such bonds of the RKKY interaction (Fig. 2.3) leads to frustration between spins within the system. Frustration occurs when the system is unable to satisfy all possible ground states. A common example is the following:

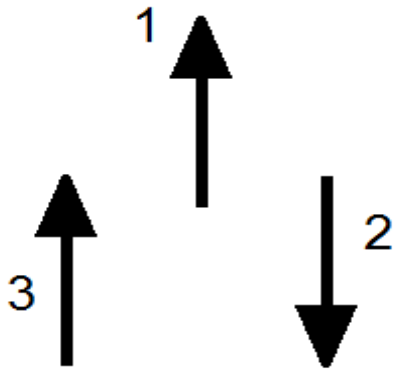


Figure 2.4: Representation of antiferromagnetic Ising spin system with frustration.

Suppose one has an Ising-type (one dimensional spin) system with only 3 antiferromagnetic spin interactions as shown in Fig. 2.4. Even though antiferromagnetic bonds 1,2 and 2,3 are satisfied, bond 1,3 is left such that it is not in its lowest energy configuration. No matter what way this

system is oriented, there will always be one set of spins where the bond is left unsatisfied. When this frustration is combined with the structural disorder of the spin glass, there tends to be no long range order of magnetization.

## 2.2 Theoretical Models

There are many models used to describe the dynamics of magnetism, the most common of which is the Ising Model. This model is perhaps one of the simplest and most useful models used to describe natural systems in statistical mechanics.

The Hamiltonian in a zero external field H is given as above in Eq. (2.1):

$$H = -\frac{1}{2}\sum_{ij} J_{ij} s_i \cdot s_j. \tag{2.6}$$

Unlike the Heisenberg model that includes three degrees of motion per spin, the Ising system only allows for one: spin up or spin down. Proposed by William Lenz in 1920, the model was not formally solved until 1925 for a one-dimensional ferromagnetic system by Lenz's student, Ernst Ising, who found that there is no phase transition above 0K. Nearly two decades later, Lars Onsager solved the Ising Model for a two-dimensional system under no external field. Onsager found that a phase transition does occur in two dimensions.

Currently, it is still thought unrealistic to solve the Ising model exactly for three dimensions as it falls into the NP-Complete category [9]. However, with the advancement of computer processing, Monte Carlo type simulations have been further developed to aid in the understanding of the complexity of two-dimensional systems under varying field and temperature conditions. In Fig. 2.5, Monte Carlo simulations show an example of both a ferromagnetic and an antiferromagnetic system.

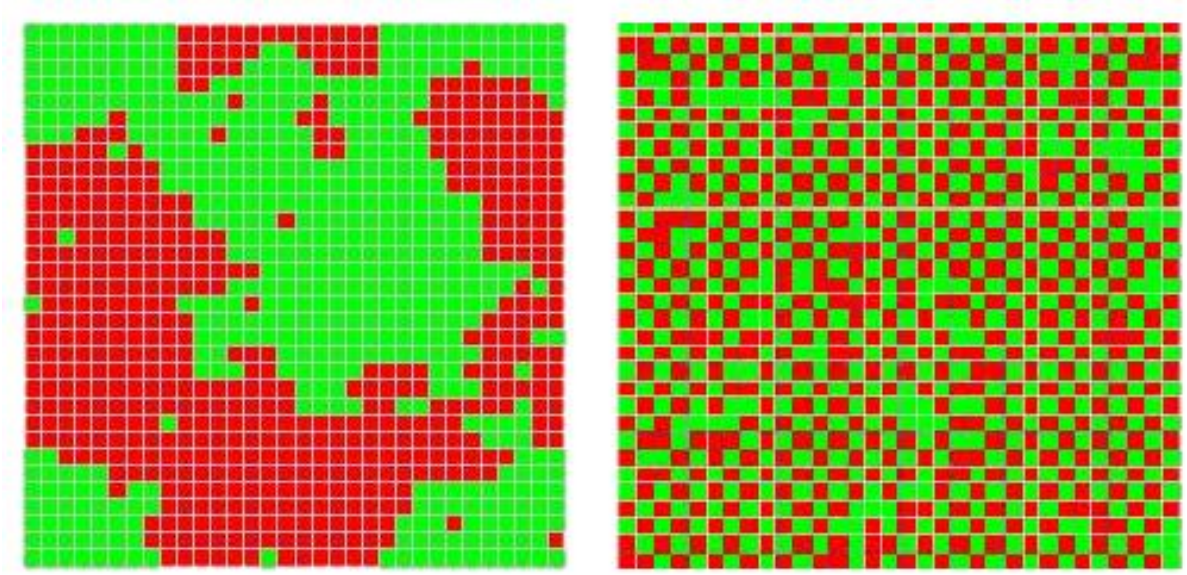

Figure 2.5: The image on the left is a simulation of a ferromagnetic system. The right is an antiferromagnetic system. These images were produced through a simulation in zero-field for this thesis using *Java Simulations for Statistical Physics*- an open source physics project.

Due to the complexity of the thermodynamics of the Ising model in two dimensions (with an external field) and in three dimensions, an approximation treatment has been developed. This treatment, known as mean field theory, allows one to assume that each spin experiences the same 'effective' magnetic field produced by nearest neighbors. As an example, we will introduce this theory using the model for ferromagnetism. This effective field, $H_{eff}$ takes the form [10]:

$$H_{eff} = J\sum_{j=1}^{q} s_j + \mu H = Jqm + \mu H \qquad (2.7)$$

where the sum is over the number of nearest neighbors, q, of spin i, and H is the applied field.

The right hand side of Eq. (2.7) shows m as the average of the magnetization per spin, $s_j$. The result of this approximation is that a system of N interacting spins can now be described as one spin interacting with an effective field dependent on all other spins.

The partition function for a spin, $s_1$, in $H_{eff}$ is

$$Z_1 = \sum_{s_1=\pm 1} e^{\frac{s_1 H_{eff}}{kT}}. \tag{2.8}$$

Through substitution of $H_{eff}$,

$$Z_1 = e^{\frac{Jqm+\mu H}{kT}} + e^{\frac{-(Jqm+\mu H)}{kT}} = 2\cosh[\frac{Jqm+\mu H}{kT}]. \tag{2.9}$$

Thus, the free energy per spin is

$$f = -kTlnZ_1 = -kTln(2\cosh\left[\frac{Jqm+\mu H}{kT}\right]) \tag{2.10}$$

and

$$m = -\frac{\partial f}{\partial H} = \tanh\left[\frac{Jqm+\mu H}{kT}\right]. \tag{2.11}$$

Eq. (2.11) is said to be a "self-consistent transcendental function" that allows one to derive the critical temperature at which a phase transition occurs [10]. A plot of this function is shown in Fig. 2.6.

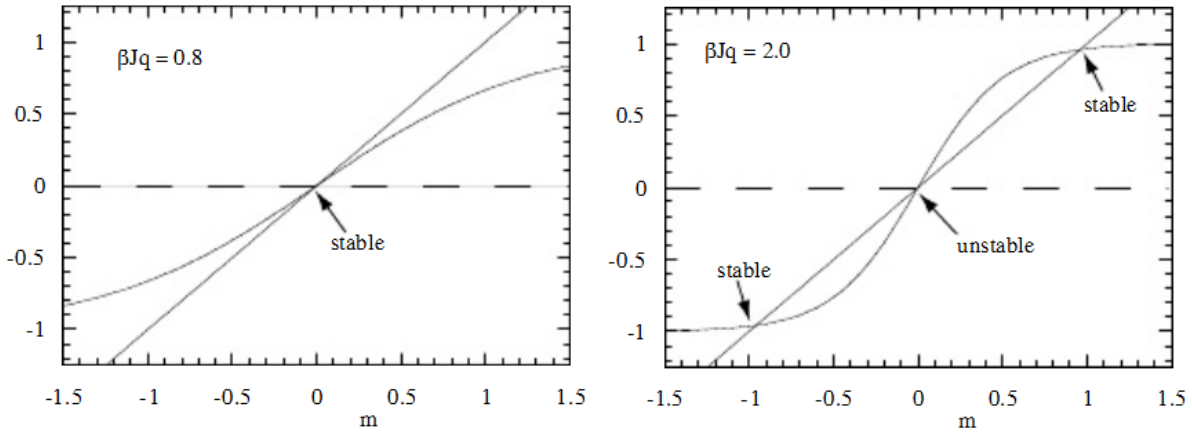


Figure 2.6: Plot of the "self-consistent transcendental function", Eq. 2.11, in zero-field. The intersection between the two functions mark possible solutions, both stable and unstable [10].

There have been several attempts to theoretically understand spin-glasses since the initial discovery of such systems in 1972 [1]. The first mean field model of the spin glass was derived by Edwards and Anderson (EA) in 1975 [2]. This "bond disorder" model introduces a description of spin glasses by using mean field theory to derive the various equilibrium thermodynamic relationships.

In order to mimic the ferromagnetic and antiferromagnetic interactions characteristic of a metallic spin glass, EA begin their model by constructing an array of spins [2]. They describe the overall energy of the lattice by the Ising Hamiltonian in zero-field:

$$H = -\frac{1}{2}\sum_{ij} J_{ij} s_i \cdot s_j. \tag{2.12}$$

The exchange constant, $J_{ij}$, is randomly chosen through a Gaussian probability distribution, and is only applied to nearest neighbors [7]:

$$P(J_{ij}) = [2\pi(\Delta J_{ij})^2]^{-\frac{1}{2}} \times e^{\left[\frac{-(J_{ij}-\bar{J}_{ij})^2}{2(\Delta J_{ij})^2}\right]}. \tag{2.13}$$

Since the exchange constant is used to determine the individual spin orientations on the lattice, the free energy of the ensemble [2] can be written as a function of $J_{ij}$:

$$F = \int f(J_{ij}) P(J_{ij}) dJ_{ij}. \tag{2.14}$$

Through the use of the free energy, one is treating the system as quenched; as working with the partition function would correspond to an annealed system [3]. The issue with averaging the free energy is that one must sum over all possible configurations of $J_{ij}$, thus averaging over all possible ln(Z) values. This is indeed a formidable and possibly impossible task, so EA uses a mathematical method known as the replica trick.

This replica trick relies directly on the averaging of the free energy component, ln Z(x), by using a mathematical identity (Eq. 2.15) [8].

$$[lnZ(x)]_{ave} = \lim_{n\to 0} \frac{1}{n}([Z^n(x)]_{ave} - 1). \quad (2.15)$$

For any positive integer n, $Z^n(x)$ can be written in terms of n identical replica systems:

$$Z^n(x) = \prod_{\alpha=1}^{n} Z_\alpha(x) = e^{-\sum_{\alpha=1}^{n} H(x,s_i^\alpha)/kT}, \quad (2.16)$$

where $Z_\alpha(x)$ is the partition function of the αth replica.

Through use of mean field theory, the above equation can be expressed as

$$[Z^n(x)]_{ave} \equiv Tr_{[s_i^\alpha]}\,[e^{-\frac{H_{eff}(n)}{kT}}]. \quad (2.17)$$

The use of the replica trick leads to the order parameter $q = \langle s_i^\alpha s_i^\beta \rangle$, where $\alpha \neq \beta$ [8]. As will be seen in the next few theories, q plays a very important role in spin glass models. Edwards and Anderson understood q to conclude the following [2]:

Consider the same spin at time t = 0, and t > 0:

$$q = \langle s(0) \cdot s(t) \rangle, \quad (2.18)$$

- if q = 0, the spins are uncorrelated, and the system is paramagnetic.
- if $q \neq 0$, the spins are correlated, and a phase transition must occur.

This phase transition turns out to appear in the susceptibility at $T_g$:

- At $T > T_g$ the system exhibits a disordered paramagnetic state.

- At $T < T_g$ the spin glass will become semi-ordered with various degenerate ground states.

Above the critical transition temperature, the paramagnetic state follows a Curie-Weiss Law. Below $T_g$, the susceptibility takes the form:

$$\chi = \frac{a}{T} - O(T_g - T)^2, \tag{2.19}$$

and as $T << T_g$,

$$\chi = \frac{a}{T}\left(\frac{3}{2\pi}\right)^{\frac{1}{2}}\left(\frac{T}{T_g}\right). \tag{2.20}$$

When $T \rightarrow 0$, $\chi$ becomes temperature independent.

Sherrington-Kirkpatrick hypothesized [3] that the mean-field theory for spin glasses introduced by Edwards-Anderson should become exact in an infinite-range model. Their model is characterized by the EA order parameter, $q = < s_i^{\alpha} s_i^{\beta} >$, using N Ising spins with the same Hamiltonian, Eq. (2.12), and probability, Eq. (2.13). This probability function remains consistently the same without regard to spin distance. While this is a physically unrealistic assumption, Sherrington and Kirkpatrick knew that the mean field theory of ferromagnetism becomes exact in the infinite-range limit [3,8], thus they hypothesized the same result could come of spin glasses.

Following the replica trick, the SK model's $[Z^n]_{av}$ takes the form [8]:

$$[Z^n]_{av} = \sum_{\{s_i^\alpha = \pm 1\}} \int_{-\infty}^{\infty} [\prod_{<ij>} P(J_{ij}) dJ_{ij}] e^{\beta \sum_{<i,j>} J_{ij} \sum_{\alpha=1}^{n} s_i^\alpha s_j^\alpha}, \quad (2.21)$$

where α = 1,2…,n denotes a replica.

Thus free energy is [3]

$$F = NkTln(Z) = NkT\{\frac{-\tilde{J}^2(1-q)^2}{(2kT)^2} + \frac{\tilde{J}_0 m^2}{2kT} - (2\pi)^{-\frac{1}{2}} \int e^{-\frac{Z^2}{2}} \ln[2\cosh(\frac{\tilde{J}q^{\frac{1}{2}}Z}{kT} + \frac{\tilde{J}_0 m}{kT})] dz\}. \quad (2.22)$$

Here, q and m satisfy the following simultaneous equations, and indicate that magnetic order sets in as kT gets smaller than either J or $J_0$, whichever is greater [8]:

$$q = 1 - (2\pi)^{-\frac{1}{2}} \int e^{-\frac{Z^2}{2}} sech^2(\frac{\tilde{J}q^{\frac{1}{2}}Z}{kT} + \frac{\tilde{J}_0 m}{kT}) dz, \quad (2.23)$$

$$m = (2\pi)^{-\frac{1}{2}} \int e^{-\frac{Z^2}{2}} tanh(\frac{\tilde{J}q^{\frac{1}{2}}Z}{kT} + \frac{\tilde{J}_0 m}{kT}) dz. \quad (2.24)$$

If $J_0 > J$, the system appears to be ferromagnetic, but if $J_0 < J$ the system is in the spin-glass state and m remains zero.

The obtained susceptibility is of the form:

$$\chi(T) = \frac{[1-q(T)]}{\{kT - \tilde{J}_0[1-q(T)]\}}. \quad (2.25)$$

Above $T_g$, where q = 0, χ follows the Curie-Weiss law. As with the EA model, the susceptibility exhibits a cusp at $T_g$.

The SK model, also known as the Replica Symmetric model, found an analytical solution for q, which led to the following relationships for specific heat and internal energy [8]:

$$C = \frac{J^2}{2T^2}, \text{ T} > \text{T}_g \tag{2.26}$$

and

$$-U = \frac{J^2}{2T}(1 - q^2). \tag{2.27}$$

This replica symmetric solution was thoroughly examined by other scientists, and evidence was found proving failure of this model at very low temperatures. There, at T→0, the entropy turns out to be a negative number.

Georgio Parisi [4] came up with a solution to the SK model, where the symmetry in the order parameter ($q_{\alpha\beta} = q$) is broken. For this solution, called Replica-Symmetry-Breaking (RSB), consider an n x n matrix, divided along its diagonal by $m_1$ x $m_1$ blocks. Each of these blocks is divided again, along the diagonal, into more subdivisions; see Fig. 2.7 [11].

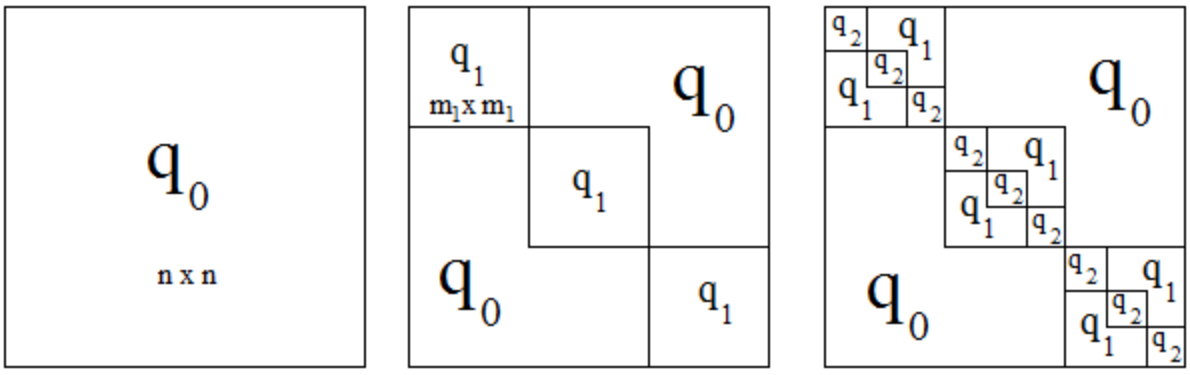


Figure 2.7: The matrix structure during the replica symmetry breaking process introduced by Parisi [11]. From left to right: 0 step symmetry breaking, 1 step symmetry breaking, 2 step symmetry breaking. All diagonal elements are zero.

All elements within the diagonal are zero. As iterations of this process continue to infinity, the Parisi order parameter, q(x) is obtained. Here, $0 \leq x \leq 1$ and x is a continuous variable corresponding to the value of a subdivision in the matrix, and representing an infinite number of order parameters. In the SK solution, these divisions are taken to zero, thus $q(x) = q_0$ and is independent of x. All pertinent information obtained through replica-symmetry-breaking is contained within q(x), and can be accessed by the following equation:

$$-\lim_{n\to 0} \frac{1}{n} \sum_{\alpha\beta} q_{\alpha\beta} = \int_0^1 q(x)dx \, . \tag{2.28}$$

A simple way to code this information [4] is to formally define $q(x) = q_i$ for $m_1 < x < m_{i+1}$, and $0 < x < 1$. In a finite system ($i \to N$), this function turns out to be a constant piecewise function whose form as $N \to \infty$ becomes two individual functions:

$$q(x) = \frac{1}{3}x + O(\tau^2), \; x \leq 3\tau, \tag{2.29}$$

$$q(x) = \tau + O(\tau^2), \; x \geq 3\tau. \tag{2.30}$$

Here $\tau$ is proportional to $T_c - T$. The physical implication of q(x) is that symmetry breaking does not occur suddenly and only at $T_g$, but continuously occurs for all $T \leq T_g$. This can be better explained by introducing the probability distribution for various overlaps among individual equilibrium states,

$$P(q) = \langle \sum_{\alpha\beta} e^{-(F_\alpha + F_\beta)} \delta(q_{\alpha\beta} - q) \rangle, \tag{2.31}$$

where $F_\alpha$ and $F_\beta$ are the free energies of state $\alpha$ and state $\beta$, respectively. Through observation of the function P(q), it can be seen that the spin glass distribution is unique in comparison to other forms of magnetism (see Fig. 2.8) [11]. In paramagnetism, there is only one thermodynamic

state. This state can be represented by a delta function at q = 0. In ferromagnetism, there are two possible states below the Curie temperature, either spins aligned up or down. Thus, two delta functions located at ± $m^2$ compose P(q). Unlike the previous two magnetic systems, a spin glass is continuous below its transition temperature, as previously mentioned. This can be represented by a continuous curve between two delta functions located at ± $q_{max}(T)$, where $q_{max}$ is the maximum overlap between states. This is the Edwards-Anderson order parameter, where all states are considered identical.

From the Parisi Solution, the susceptibility can be written as:

$$\chi = \frac{1}{kT}\int_0^1 [1 - q(x)]dx. \tag{2.32}$$

χ(T) can be obtained through substituting the value of q(x) for a particular temperature. The Parisi solution to the SK model has been found to resolve the issue of negative entropy.

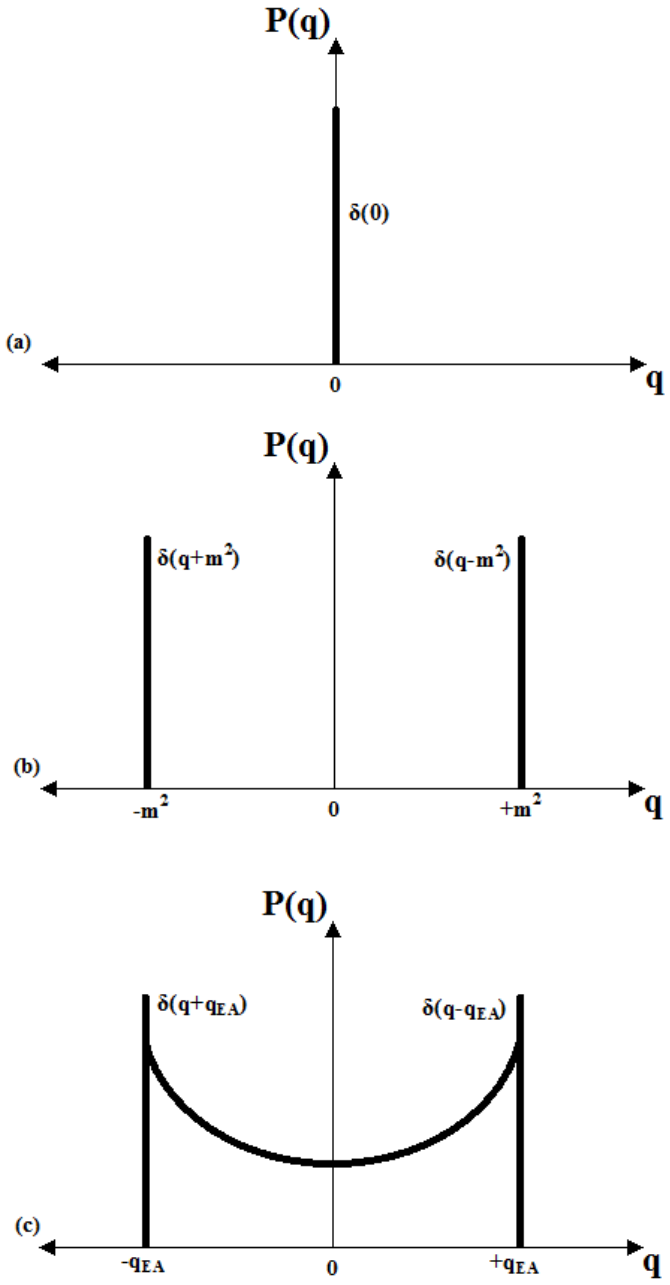


Figure 2.8: Probability distribution P(q) for different magnetic phases [11]. (a) Paramagnetism (b) Ferromagnetism (c) Spin Glass.

An alternative way of looking at the Parisi solution is through a hierarchical tree model, as shown in Fig. 2.9 [8]. The bottom branches of the tree represent n replicas of the system. The vertical axis on the left hand side of this tree represents the value of q, analogous to the matrix element of the RSB scheme.

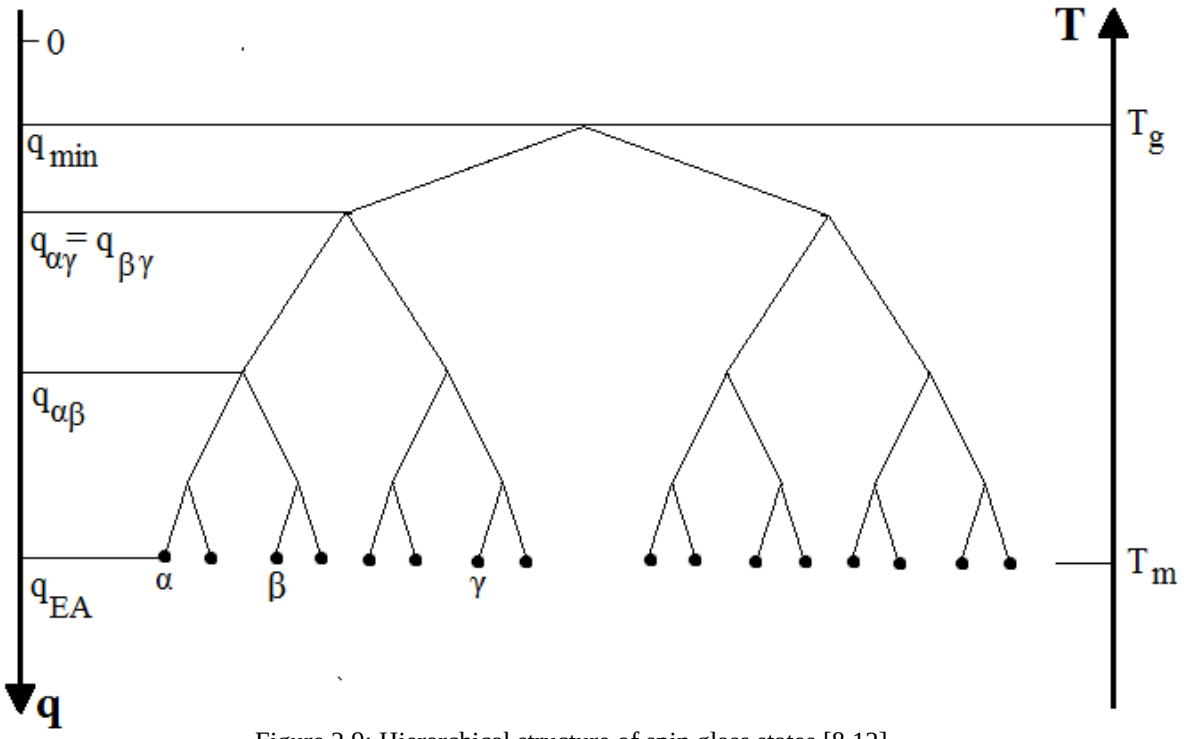


Figure 2.9: Hierarchical structure of spin glass states [8,12].

An interesting correlation is made if the replicas on the bottom of the tree are considered states of the system. In this instance, q is denoted as the overlap function defined as

$$q_{\alpha\beta} = \frac{1}{N}\sum_i S_i^{\alpha} S_i^{\beta}. \tag{2.33}$$

This overlap represents a quantitative measurement of the similarity between two states. As can be deduced from observation of Fig. 2.9, the maximum overlap between states is the Edwards-Anderson order parameter, where all states are identical. This corresponds to the Parisi order

parameter at x = 1. As q decreases along the vertical axis to $q_{min}$ and as T increases to $T_g$, there is an ever increasing degree of difference between the states. This is represented by the amount of branches a state would have to traverse in order to replicate another state.

The problem with the application of the Parisi solution, and its infinite-dimensional pure states, is that in order for one state to replicate another, it would have to exert an infinite amount of energy to do so. In a free energy landscape this would mean each state is separated by infinite barriers, resulting in no dynamics. We know from experiment, to be discussed in the next section, that spin glasses are a very dynamic system given the fact that they age, and even hold a memory of their age as evident in the thermoremanent magnetization.

A "configuration disorder" model known as the barrier model [13] has been developed using the knowledge of the hierarchical landscape of Parisi and applies it to finite-sized barriers. Let us introduce a free energy landscape that evolves as T decreases below $T_g$ (Fig. 2.10). The number of relative free energy minima, i.e. metastable states, $N_s$, increases exponentially as a function of temperature, shown in Eq. 2.34 [12].

$$N_S = e^{\frac{8}{81}Nt^6} \tag{2.34}$$

and

$$t = 1 - \frac{T}{T_g}. \tag{2.35}$$

Consequently, the complexity of the energy landscape also increases, leading to many energy barriers separating the states [12]. The formation of such barriers and their relationship to aging can be viewed as follows:

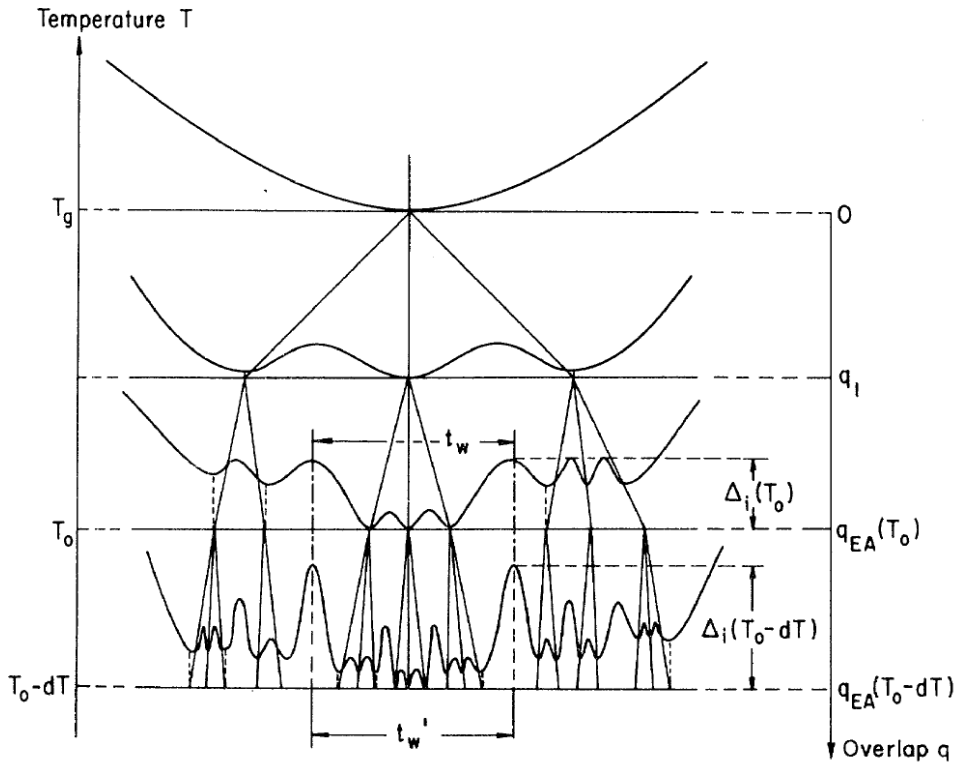


Figure 2.10: Hierarchical structure of the barrier model. [12]

As the spin glass is cooled below $T_g$ in an applied field, H, a free energy landscape (Fig. 2.11) is formed with N metastable states of constant magnetization $M_{FC}$, separated by barriers of height $\Delta_{\alpha\beta}$. As the system is held in H for a waiting time, $t_w$, at constant temperature $T_o < T_g$ it ages by overcoming these energy barriers and occupying subsequent metastable states. The highest barrier overcome during the waiting time is determined by [11,12]:

$$\Delta_{max} = k_b T ln(\frac{t_w}{\tau_o}), \tag{2.36}$$

and the rate of surmounting a barrier varies under the Arrhenius law:

$$\frac{1}{\tau_{\alpha\beta}} = \frac{1}{\tau_0} e^{-\frac{\Delta_{\alpha\beta}}{T}} \tag{2.37}$$

where $\tau_o$ is a microscopic characteristic time. The amount of phase space occupied is characterized by the highest barrier overcome during $t_w$ [12].

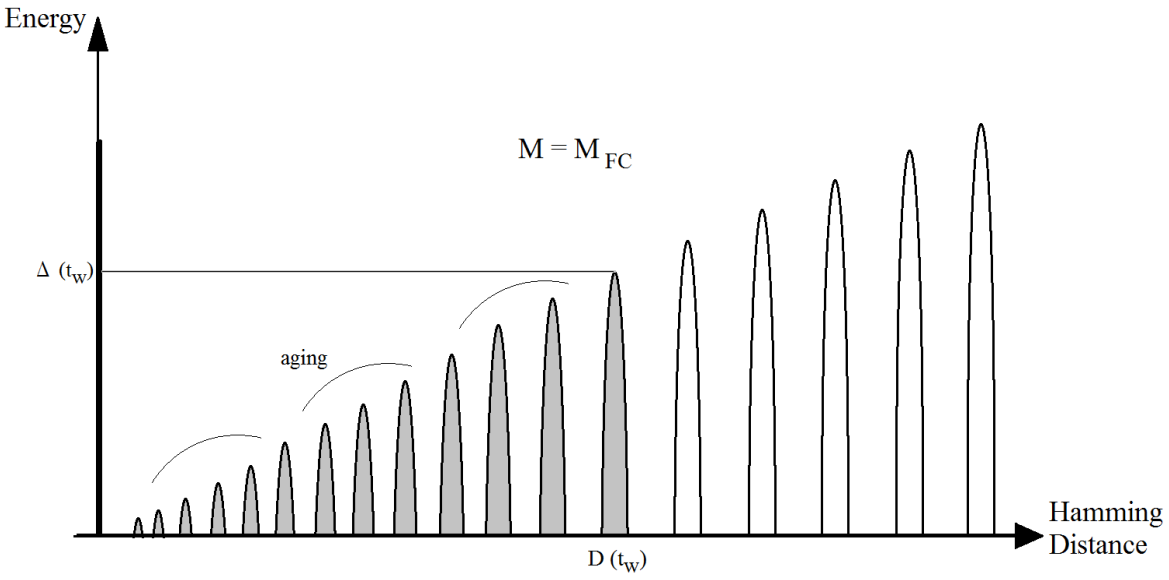


Figure 2.11: Energy landscape with metastable states of magnetization MFC, separated by barriers [11].

As the field is cut to zero after $t_w$, two rather closely related processes occur. The first of which is a new set of metastable states emerges with a constant magnetization of zero, replacing the $M_{FC}$ manifold. The second is that the difference between the Zeeman energies, $E_Z$, of the two manifolds, where

$$E_Z = HM_{FC}, \tag{2.38}$$

causes the barriers with $\Delta_{\alpha\beta} < E_Z$ in the first manifold to collapse, instantaneously emptying previously occupied states (Fig. 2.12). Conversely, those states with $\Delta_{\alpha\beta} > E_Z$ remain unaffected, as this is the irreversible part of the magnetization decay, the TRM.

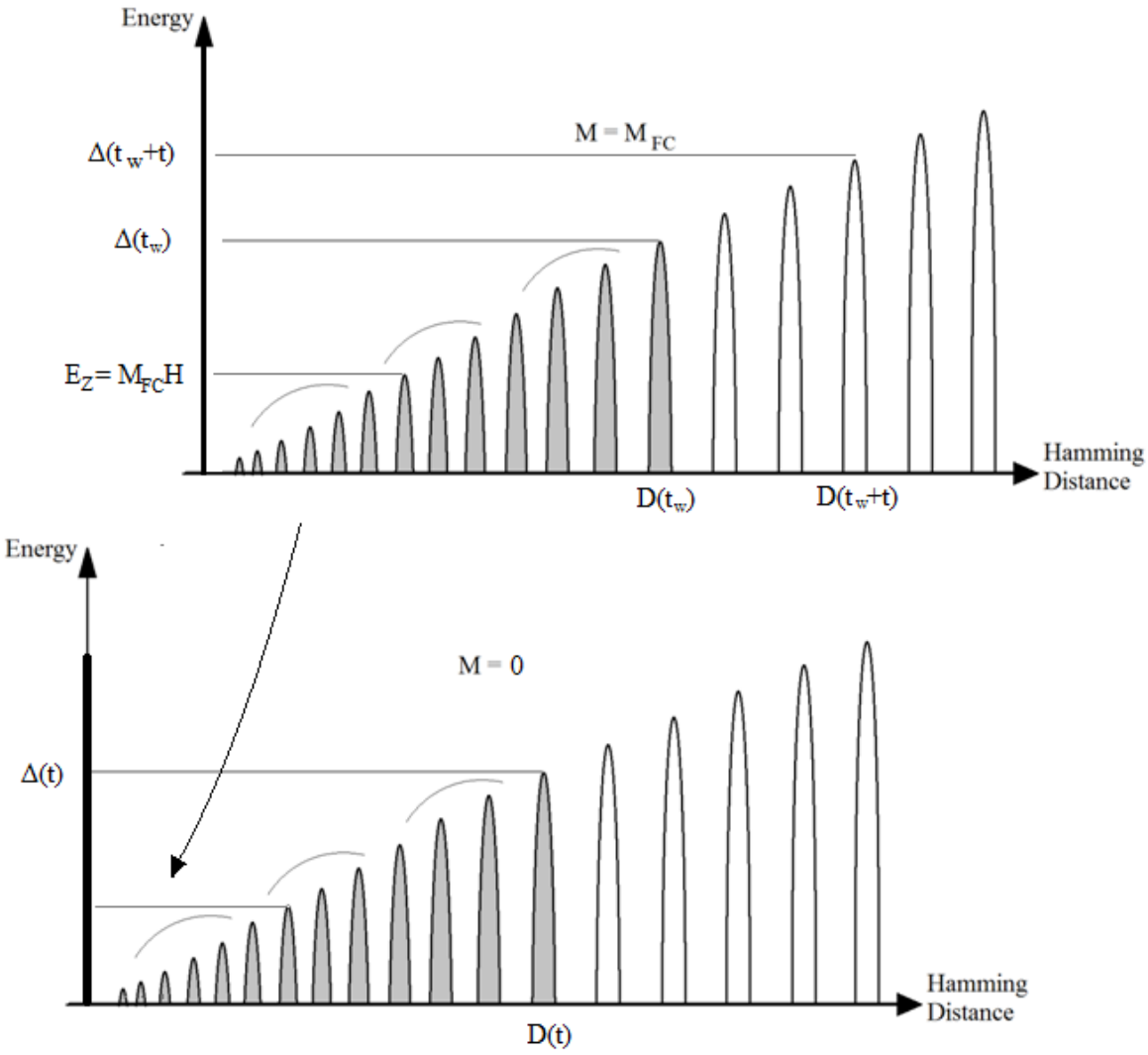


Figure 2.12: $M=M_{FC}$ and $M=0$ manifolds [11].

## 2.3 Experimental Concepts of Aging in Spin Glasses

The topics discussed in the theoretical section of this chapter, particularly the barrier model, can be explored through analysis of the thermoremanent magnetization, the common measurement taken for such aging experiments. As briefly introduced in theory, the experimental procedure is as follows:

A spin glass is rapidly cooled (cooling time approximately 20s) through $T_g$ to a measurement temperature $T_m$ in an applied external field. The external field is left on for a specific amount of time, $t_w$, known as the waiting time, where the system undergoes aging. After $t_w$ expires, the field is turned off in one step and the spin glass TRM begins to decay. By studying the response of several different $t_w$, it has been found that each individual decay is dependent on the amount of time the system spent in the external field (its age), indicative of memory. Making the correlation between theory and experiment, this 'memory' is defined by the largest barrier overcome during $t_w$. One can confirm this time dependence through a plotting the function S(t) vs. log(t), where:

$$S(t) = -\frac{1}{H}\frac{dM}{d[log(t)]}, \tag{2.39}$$

as can be seen in Fig. 2.13 [13].

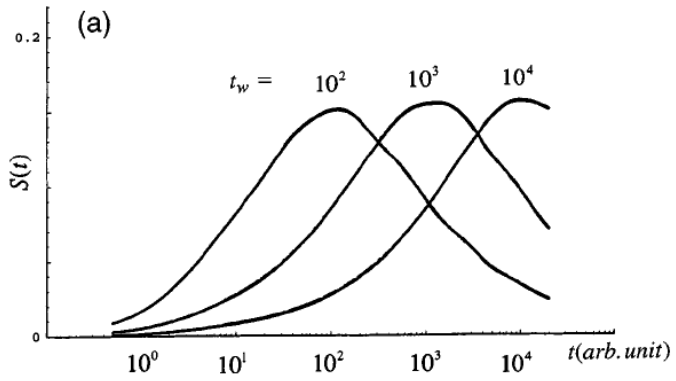


Figure 2.13: S(t) graph displays curve maxima denoting the location of $t_w$ [13].

Scaling TRM decays onto a master curve has led to the identification of a possible explanatory function. This function describes the nature of the decay and though analysis can give the response curve of the sample at any given age [15]. The true mathematical expression for such a curve has been a heavy topic of discussion, including relationships such as power laws, stretched exponentials and the like, but all of these prospects include a scaling parameter μ with the following attributes [16]:

- if $\mu < 1$ the system is said to be sub-aged.
- if $\mu > 1$ the system is super-aged
- if $\mu = 1$ the system is fully aged.

It was found later [17] that the full magnetization decay can be written as:

$$M(t, t_w) = M_0 \left(\frac{t}{t_w}\right) + \left(\frac{t_w}{C}\right)^{-x} \sum_{i=1}^{2} \frac{a_i}{\lambda_i + x} \left[1 - \left(\frac{t}{t_w}\right)^{\lambda_1 + x}\right], \tag{2.40}$$

where x is a parameter that controls all deviations of aging defined as

$$x = \frac{1}{ln(\frac{t_M^*}{\tau})}, \tag{2.41}$$

and λ is an aging term, dependent on both t and $t_w$, of the form:

$$\lambda = \frac{t_w}{1-\mu} [(1 - \frac{t}{t_w})^{1-\mu} - 1]. \tag{2.42}$$

Through an analysis of three standard scaling techniques [16], it was found that the overall effective cooling rate of the sample has a dramatic impact on the scaling of these curves (Fig. 2.14). It was also found that through the subtraction of a small power-law term, Eq. (2.43), from the decay further improves scaling.

$$M(t) = A(\frac{\tau_0}{t})^{\alpha}, \tag{2.43}$$

where A = 0.06, α = 0.02 and $\tau_0 = 10^{-12}$s.

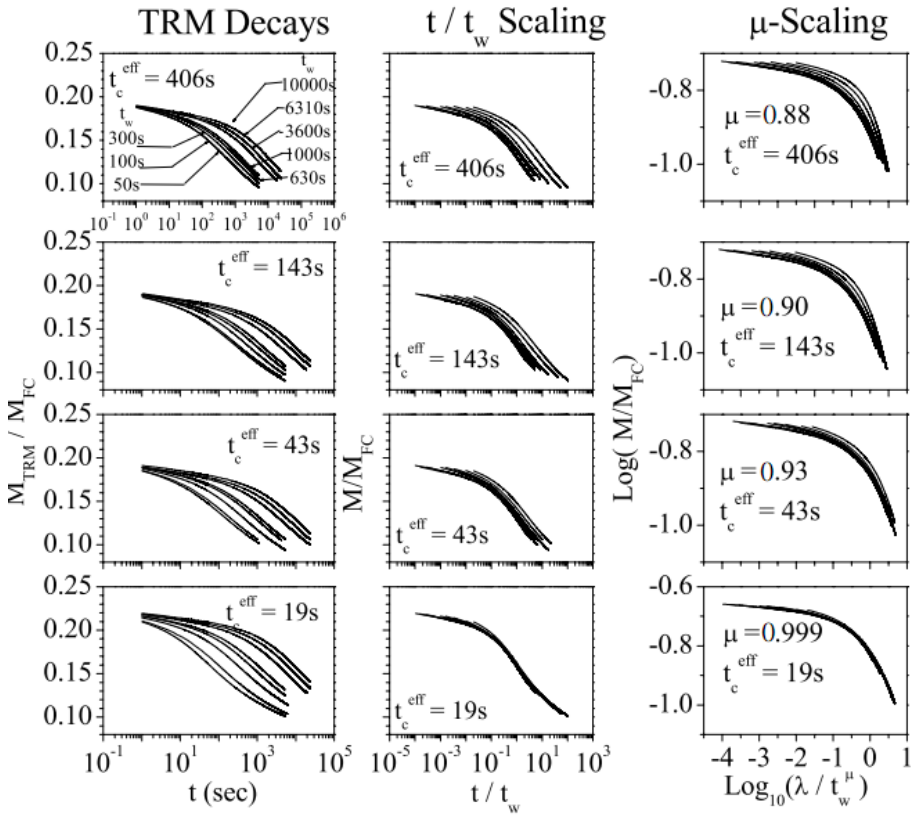


Figure 2.14: Different TRM scaling methods with various cooling times [16].

TRM decays with $t_w = 0$ or ZTRM decays with fast cooling protocols have lead to the discovery of a logarithmic decay far into $t_m$ [14]. It was found that this decay is not an additive term, nor is it dependent on $t_w$. It allows one to find the fluctuation time scale, defining the lower cut-off point in the hierarchal model. As the measurement temperature is increased closer to $T_g$, the TRM is noted to approach this logarithmic term much quicker (Fig. 2.15). Since this term has no

dependence on the aging of the system, it has been denoted to mark the end of the aging process [14]. Our purpose in this thesis is to probe this logarithmic decay in the hopes that it will open the door to new processes, whether that be a decay, an equilibrium state, or a new phenomenon altogether.

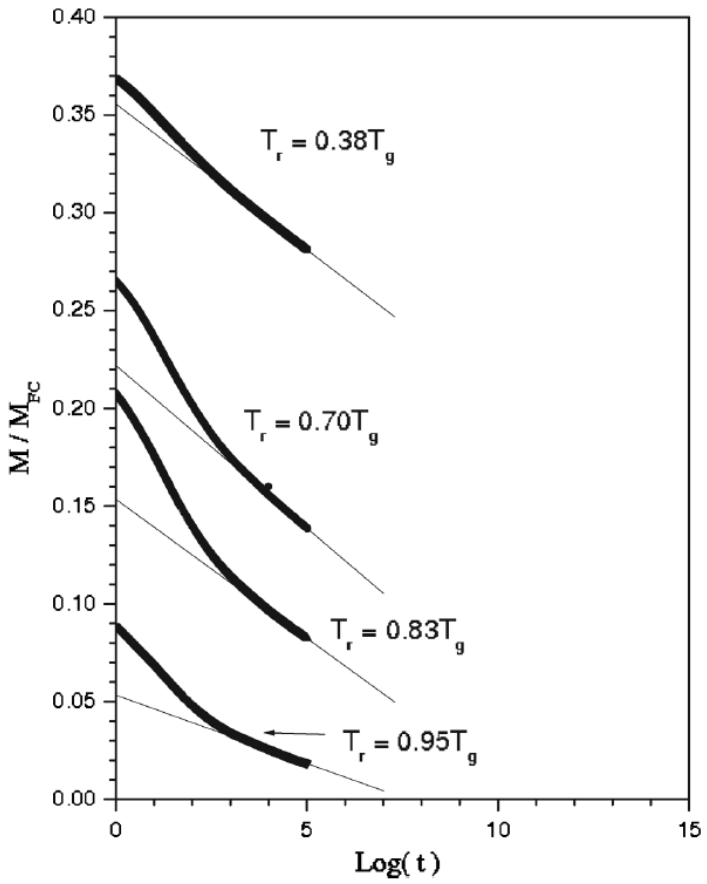


Figure 2.15: Curve fitting to the logarithmic decay at $t>>t_w$ for various measurement temperatures below $T_g$ [14].

CHAPTER 3

# DEVELOPMENT OF THE EXPERIMENTAL APPARATUS

In order to reliably perform the experiments on aging in non-equilibrium systems previously discussed in this thesis, it was required that a piece of equipment be built with excellent signal to noise ratio as well as unparalleled temperature control. It is now understood that thermoremanent magnetization (TRM) decays are dependent on the waiting time, $t_w$. It is also known that the signal decay over the course of the measurement time would become increasingly smaller. Hence, a DC SQUID (Superconducting Quantum Interference Device) magnetometer was the ideal candidate for this experimental work. This chapter discusses the main components of the magnetometer and their characteristics.

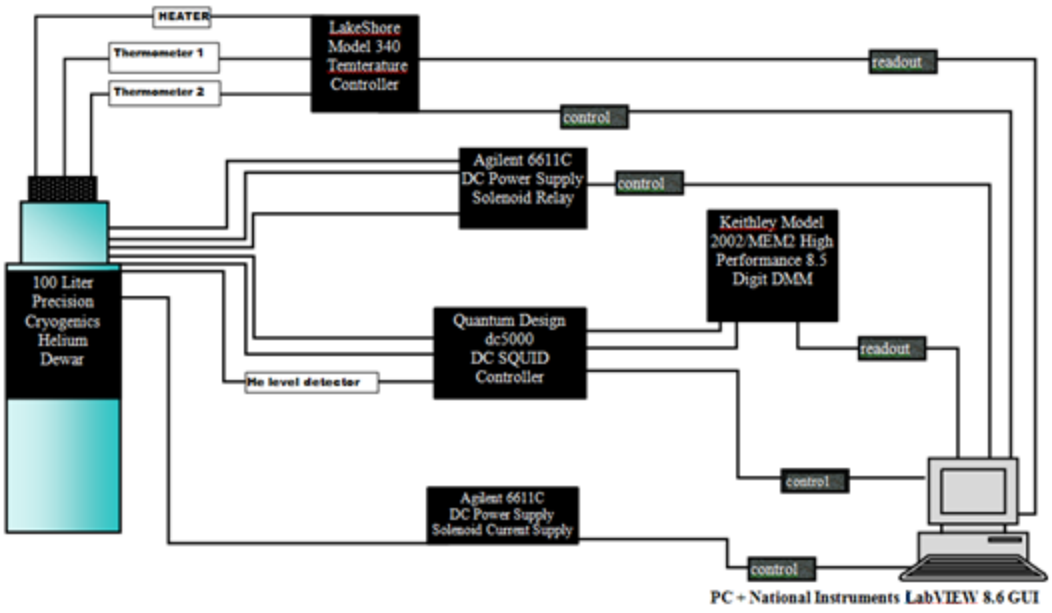


Figure 3.1: Equipment arrangement.

The dual DC SQUID magnetometer (DDSM) consists of five major components, all of which play a critical role in the proper function of the system. Fig. 3.1 displays the connection arrangement for the entire system. The magnetometer components, including two SQUIDs, two temperature sensors, a heater, helium level detector and a solenoid, located inside the Dewar, are connected to the LabVIEW interface via their respective controller units.

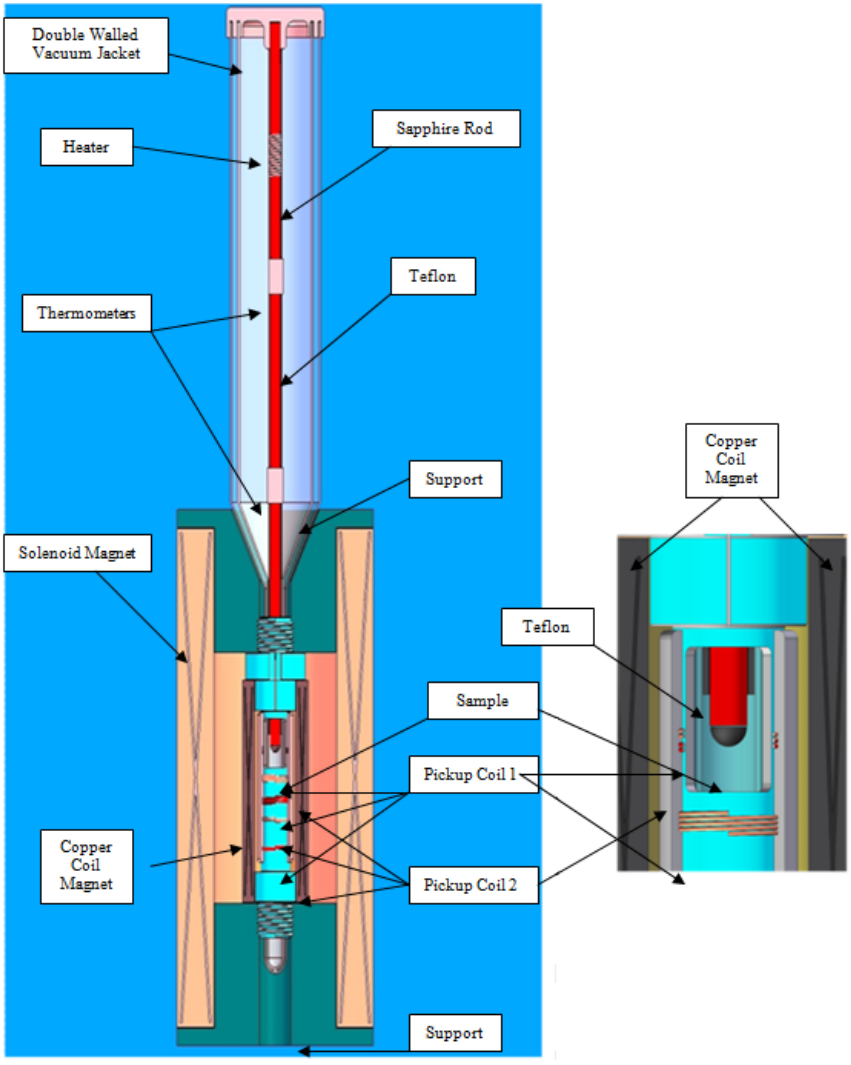


Figure 3.2: Internal Dewar schematic.

Inside the Dewar is the heart of this machine, shown in Fig. 3.2. The CuMn sample is connected to the very bottom of a single crystal sapphire rod, positioned in the top loop of a double axial gradiometer setup. Farther up the sapphire rod are two temperature sensor units, followed by a manganin heater coil. This setup sits centered vertically within the gradiometers, which in turn are centered within the solenoid. Above the solenoid are located two SQUIDs, connected to each pick-up coil (gradiometer) with superconducting NbTi wire. These components are secured to a G10 and stainless steel housing, and shielded with lead. A helium level detector runs vertically through the magnetometer housing to the bottom of the Dewar.

In this chapter, we will break down each of these components into their individual subsystems; describing their attributes and overall function, including automation sequence and programming.

## 3.1 SQUIDs and Signal Control

The Superconducting Quantum Interference Device (SQUID) is the most sensitive amplifier currently available for laboratory use. In our magnetometer, we use two Niobium thin-film DC SQUID sensors, both of which are model 50DCSQUID (Fig. 3.3) made by Quantum Design.

The main characteristics of this type of sensor are:

- Operating Temperature: < 1K-7K
- Input Inductance: 1.9 μH Nominal
- Input Sensitivity: 0.2 $\mu A/\Phi_0$
- White Noise Density, Matched Input: $4x10^{-6}\Phi_0$ Typical
- Modulation Coil Inductance: 0.07 μH Nominal

- Modulation Coil Sensitivity: 1.5 $\mu A/\Phi_0$
- Effective SQUID Bias Current: 15-30 μA
- Modulation Frequency: 500KHz Nominal
- Output Frequency Range: 200KHz – 1MHz

The SQUIDs are connected to two axial gradiometers, shown in Fig. 3.5, in vertical alignment. SQUID A (serial number A66.7) is connected to a third order gradiometer and SQUID B (serial number A66.4) is connected to a second order gradiometer via the input coil terminals located on each sensor. The measured resistance of each gradiometer at the input terminals is 1.8Ω and 1.7Ω, respectively. The gradiometers are wound around a fabricated G10 glass-epoxy laminate cylinder, adhered into alignment with General Electric (GE) Varnish.

The SQUID circuit, containing the Josephson junction, is encased in a Niobium (Nb) threaded cylinder, attached by a niobium/phosphor-bronze housing to a shielded cable leading to the connection point of the micro-preamplifier. This probe, also manufactured by Quantum Design (model DFP-1), allows for the SQUID to be placed in any position within the magnetometer without restriction due to rigidity. For a brief explanation and diagram of the probe, including pin assignments, refer to Fig. 3.4.

Located outside of the magnetometer housing, above the flange are the two micro-preamplifiers, one for each SQUID sensor. These low-noise micro-preamps connect directly into the flexible probe assembly and continue to the model dc5000 SQUID controller. The power consumption rating for each preamp is approximately 0.3W. Each micro-preamplifier connects to the controller by means of an individual multicard port located on the back panel of the controller. The multicards issued with this controller are model 500.

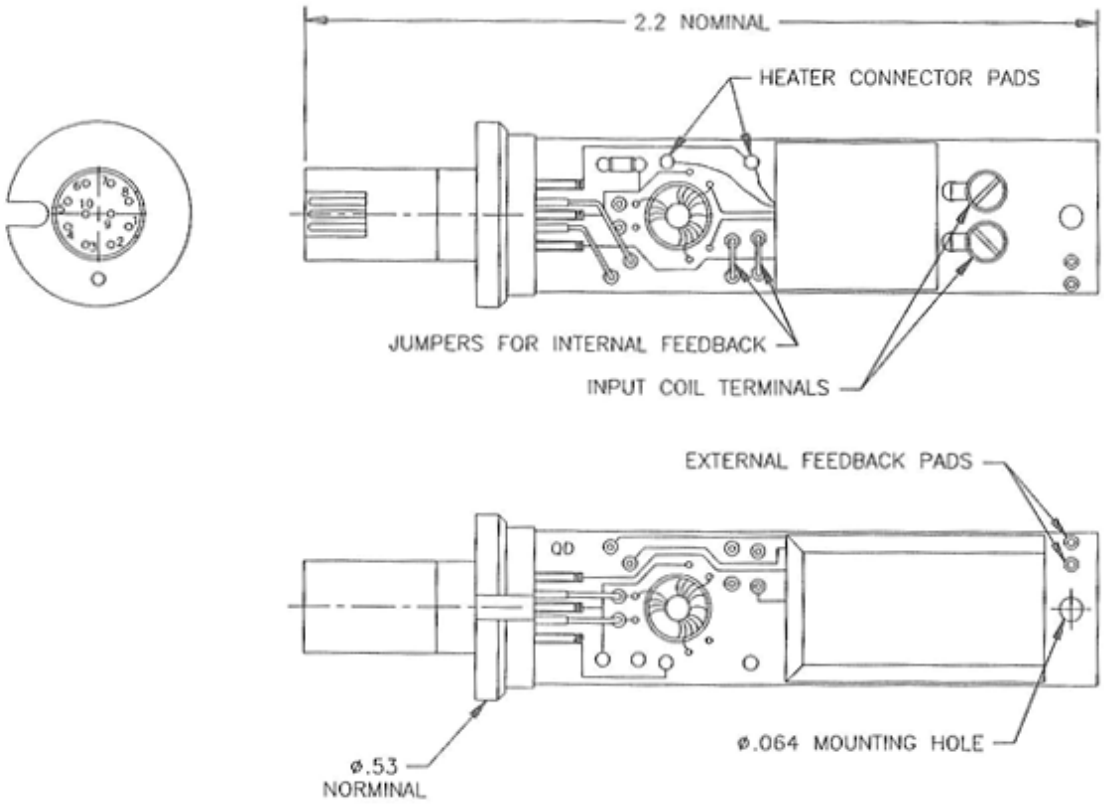


Figure 3.3: SQUID circuitry. *Diagram borrowed from Quantum Design.*

This model SQUID sensor has several variable features that allow for the most accurately sensitive measurements to be taken for individual experimental needs. The SQUID chip itself is in a unique symmetric arrangement where the modulation coils are located directly on the SQUID, a design patented by Quantum Design, Inc. For a full description of these features, refer to the dc5000 user manual. This chip is mounted on a printed circuit board, fastened securely to the housing flange.

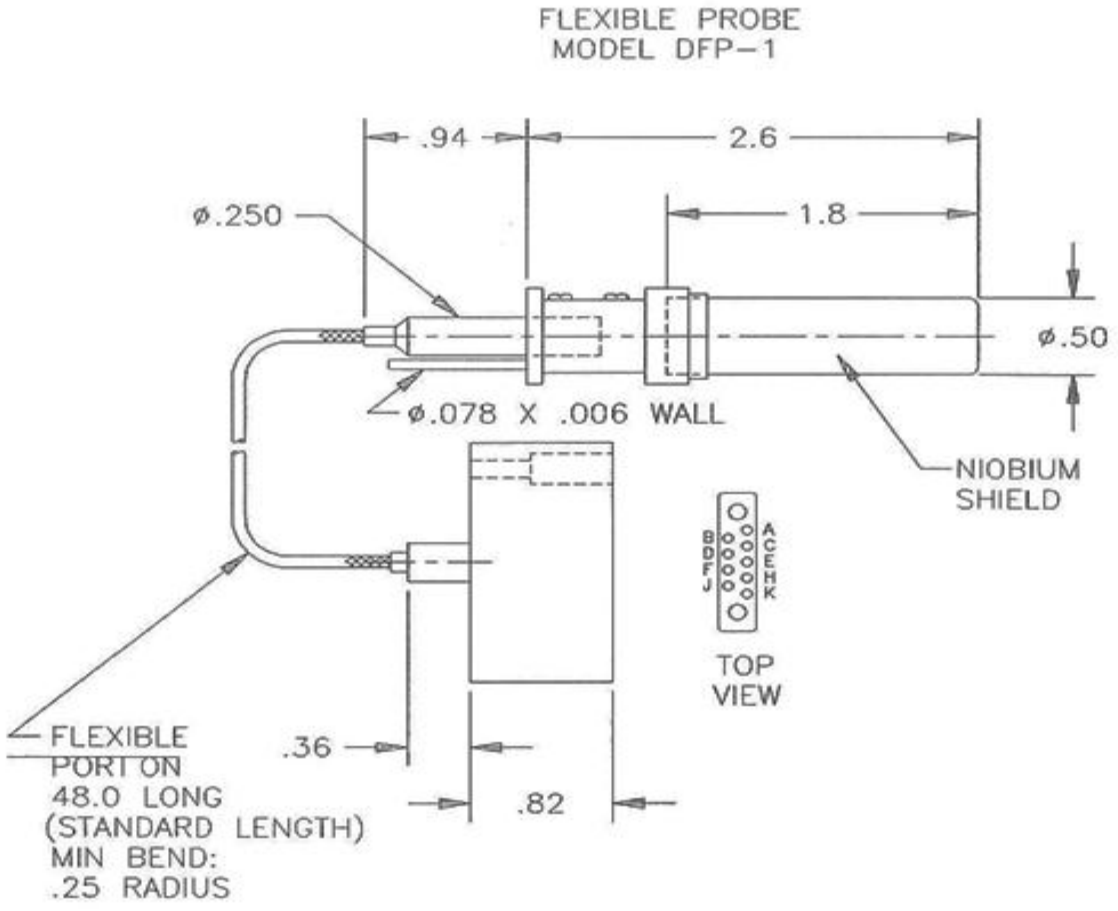


Figure 3.4: SQUID Probe Assembly. *Diagram borrowed from Quantum Design.*

The pin assignment is as follows:

- Pins 1 and 8 is the feedback loop.
- Pins 2 and 3 are signal modulation.
- Pins 4 and 5 is the signal generated by the Josephson junction.
- Pins 6 and 7 is the heater connection loop.
- Pins 9 and 10 is the signal bias.

The Model DFP-1 flexible probe was designed to be adjustable for a variety of system set-ups as well as physically streamlined to allow for a quick cool down to operating temperature. The ten pin connection from the SQUID chip is led through the flexible portion of the probe to the micro-preamp connector, located at the top of the magnetometer flange. The pin assignment of the top view of this connection is as follows:

- Pins A and C is the signal generated by the Josephson junction.
- Pins B and D is the feedback loop.
- Pins H and K is the signal modulation.
- Pins F and J is the signal bias.
- Pin E is the positive lead to the heater. The tenth pin, which is missing from this connection, is the ground to the heater.

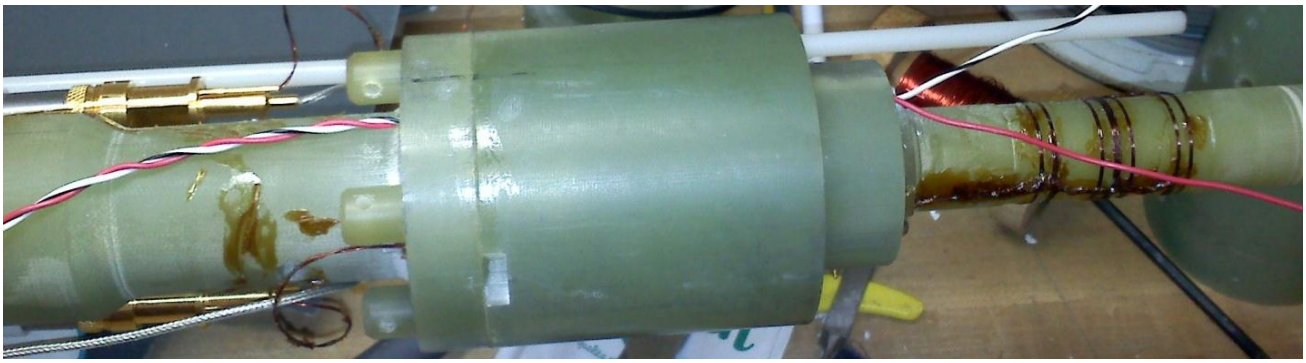

Figure 3.5: Axial Gradiometers.

## 3.2 Temperature Control

Although the SQUIDs are the primary focus of the experimental apparatus, temperature control is critical to ensure accurate and continually reliable experimentation. Our temperature control system consists of several components: a temperature controller, two temperature sensors, a heating coil with remote heat sink, and a single crystal sapphire rod. All of the components, with the exception of the remote heat sink, are located inside a double vacuum jacket within the magnetometer and are connected to their respective inputs on the controller by a 10-pin military style connector located at the very top of the magnetometer. Refer to Fig. 3.7 for the complete connection diagram.

### 3.2.1 Temperature Controller

The temperature controller chosen for the DDSM was a LakeShore Model 340, serial number 342861. Without customization, this controller has two closed-loop PID (proportional-integral-derivative) input channels and two heater outputs, the first of which can generate up to 100W of power. The front panel display can show readings in Kelvin, Celsius, or sensor units (Ω) with a

precision of 1-0.1mK when in the temperature setting. The input accuracy of the controller depends on the particular temperature sensor used, in this case the Cernox 1050-SD, which will be discussed in the next subsection. Pertinent specifications of the model 340 are:

- Number of inputs: 2
- Maximum update rate: Up to 20 readings/s per input
- PID Control Settings:
    - Proportional (gain): 0 to 1000 with 0.1 setting resolution
    - Integral (reset): 1 to 1000 with 0.1 setting resolution
    - Derivative (rate): 1 to 1000s with 1s resolution
    - Manual Output: 0 to 100% with 0.01% setting resolution
- Setpoint Ramping: 0.1K to 100K per minute

### 3.2.2 Temperature Sensors

Two Cernox 1050-SD thin-film resistive thermal devices (RTDs), figure 3.6, are used in conjunction with the controller due to their high sensitivity and low external field error. Each sensor follows a specific calibration curve calculated by LakeShore before shipment. Temperature sensor A (serial number x54875) follows curve 21 and sensor B (serial number x55088) follows curve 24. The specifications for conditions near 4.2K are as follows:

- Temperature Range: 0.3-325K
- Measurement Resolution (Temperature Equivalents): 90μK
- Calibrated Temperature Accuracy: ±8.4mK
- Electronic Control Stability (Temperature Equivalents): ±180μK

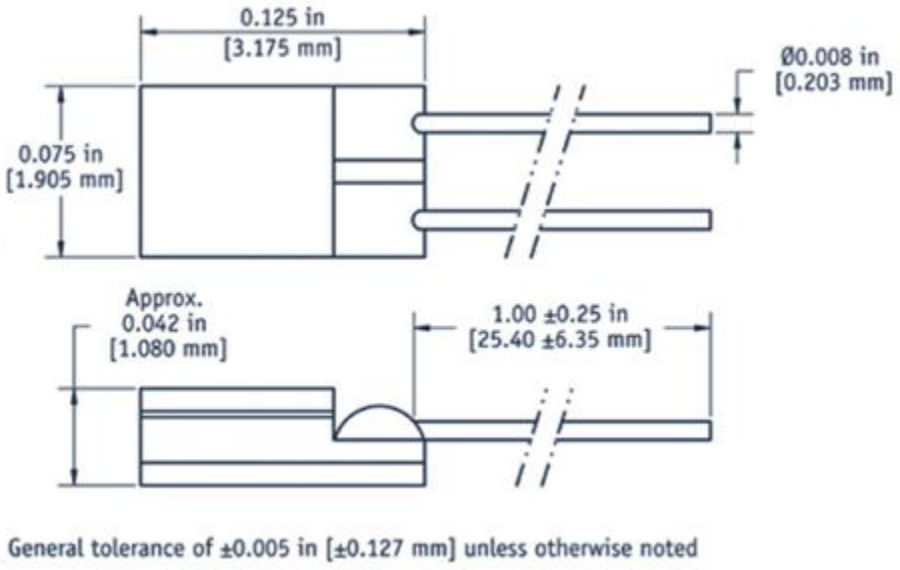


Figure 3.6: Cernox 1050-SD Temperature Sensor. *Diagram adapted from LakeShore.*

These sensors (Fig. 3.6) are connected to the inputs of the controller using a four-lead differential setup as shown in Fig. 3.9. They are placed linearly along the sapphire rod such that sensor A is closest to the sample as it is the temperature value that controls the heater output. Sensor B, set between sensor A and the primary heater coil, is used to gauge the rate of heat flow through the sapphire.

### 3.2.3 Heat Supply Circuit

The model 340 controller comes with two separate heater control loops. The first loop output is a variable DC current source with a maximum power rating of 100W. This channel is the power source for the DDSM's primary heating coil. The second channel, a manual output variable DC voltage source with a maximum power rating of 1W, is not used for this system.

The primary heating element used is a strand of 32 SWG Manganin wire, approximately 10cm long, double-wrapped, but not twisted, around the top of the sapphire rod and secured with GE varnish. The room temperature resistance is measured to be 4.8Ω. It is important to note that the temperature controller does not generate power through a heating element less than 10Ω in resistance, thus a secondary heating coil located outside of the magnetometer was installed to serve as a heat sink. This coil is secured to a solid aluminum rod and has a measured resistance of 28Ω. In series, these resistive heater loads act together to compensate for the minimal resistance of the primary coil due to limited space on the sapphire, as well as changes due to cryogenic conditions.

### 3.2.4 Sapphire Rod

Fig. 3.7 shows the thermal conductivity of sapphire compared to various other materials. The single-crystal sapphire rod is located at the very bottom of the magnetometer, secured from above with a G10 compression port. All of the temperature control elements as well as the spin-glass sample are fastened to the rod with GE varnish. For the arrangement, refer to figure 3.8. The entire sapphire rod, including all connected elements, is double-wrapped in a Mylar casing and sealed in Teflon.

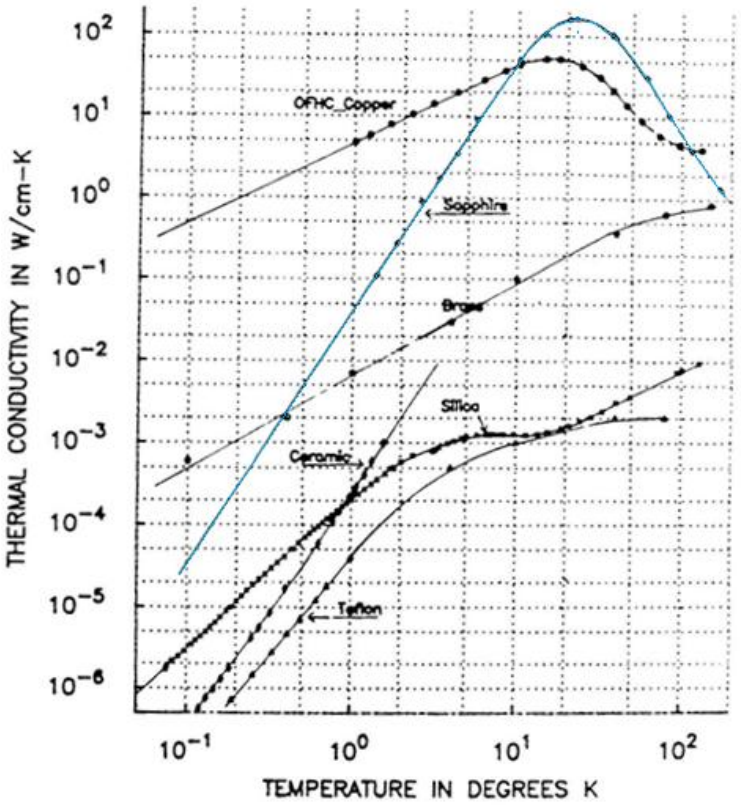

Figure 3.7: Thermal Conductivity of various materials [17].

It can be seen that sapphire has the highest conductivity of the listed materials at approximately 30K. The operating temperature range for our particular set of experiments is 30K-50K, making sapphire an excellent choice as a sample holder.

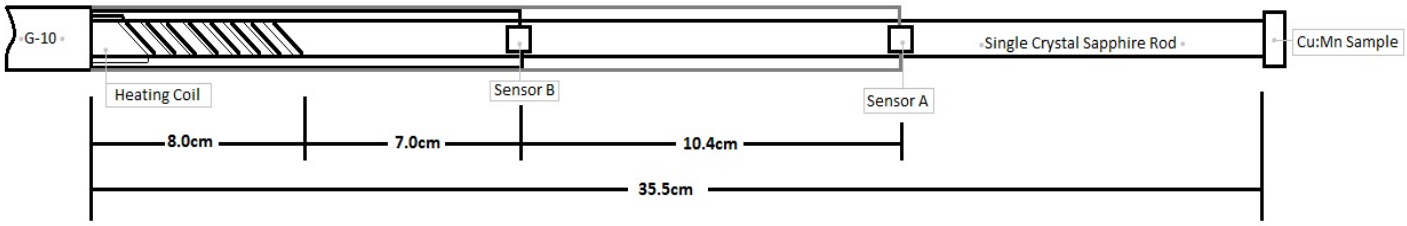

Figure 3.8: Sapphire Rod Configuration.

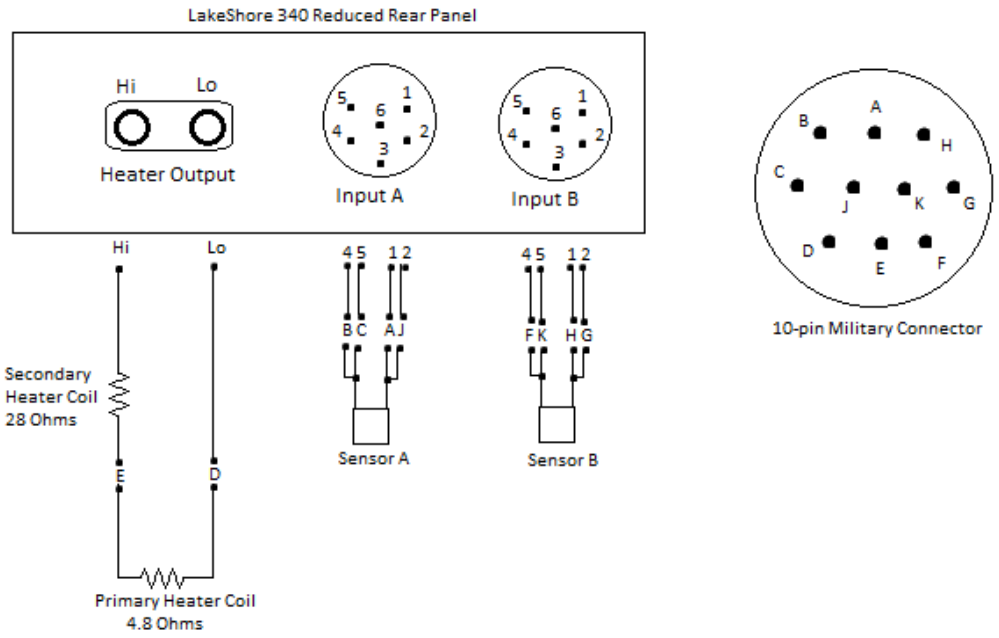


Figure 3.9: Temperature Control Connection Diagram.

The connections for each of the temperature control elements just described are illustrated in Fig. 3.9. The heater circuit consists of two separate coils. The secondary heater coil is located between the heater Hi output and the 10-pin connection on top of the magnetometer and the primary heater coil is secured to the sapphire rod located inside the magnetometer's double vacuum jacket. The total resistance of this circuit at room temperature is 32.8Ω.

Both temperature sensors are connected to the LakeShore inputs by means of a four-lead differential circuit. Input A has measured resistances 75.3Ω and 74.8Ω for the current and voltage, respectively. Input B has measured resistances 69.7Ω and 69.8Ω for its respective current and voltage. Pin assignment 6 for each input connector is not used.

The following table lists the appropriate connection for each pin assignment.

Table 3.1 Pin Assignments for Temperature Control System

| | Line Type | LakeShore Pin Assignment | 10-pin Military Assignment |
|---|---|---|---|
| Input A | I- | 1 | A |
| | V- | 2 | J |
| | Shield | 3 | N/A |
| | V+ | 4 | B |
| | I+ | 5 | C |
| Input B | I- | 1 | H |
| | V- | 2 | G |
| | Shield | 3 | N/A |
| | V+ | 4 | F |
| | I+ | 5 | K |
| Heater | Hi | Hi | E |
| | Lo | Lo | D |

## 3.3 Magnetic Field

The field source for the magnetometer is a hand-wound 1,062 turn, four-layer solenoid, powered by a DC power supply. The solenoid, shown in Fig. 3.10, consists of 28 AWG (American Wire Gauge) copper magnet wire, approximately 0.321mm in diameter, wrapped around a fabricated G10 hollow spool. The current load through the solenoid was calculated as though a maximum field of 100G was needed, however the standard operating field for these experiments is as little as one-tenth that.

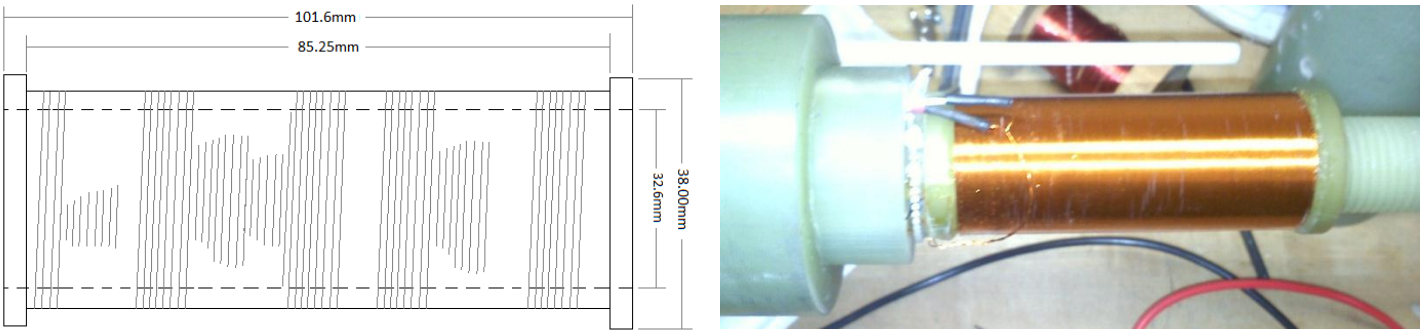


Figure 3.10: Solenoid. The solenoid fits tightly directly over the axial gradiometers, as shown on the right.

The current needed for maximum field output was calculated as follows:

$$B = \frac{\mu_0 NI}{L} \tag{3.1}$$

where:

L = 85.25mm

$\mu_0 = 4\pi \times 10^{-7}$ N/A$^2$

B = 100 G = 100 x $10^{-4}$ T

Determining the total number of complete turns, N, of the Solenoid:

$$N = \frac{4L}{D} \tag{3.2}$$

D = Wire Diameter = 28AWG = 0.321mm

N =1062.32 turns

Through algebraic manipulation:

$$I = \frac{BL}{\mu_0 N} \tag{3.3}$$

I = 0.6380A

Therefore, for 10G the current needed should be 0.0638 A.

The plotted current dissipation curve uses the equation:

$$I = I_0 e^{\frac{rt}{l}} \tag{3.4}$$

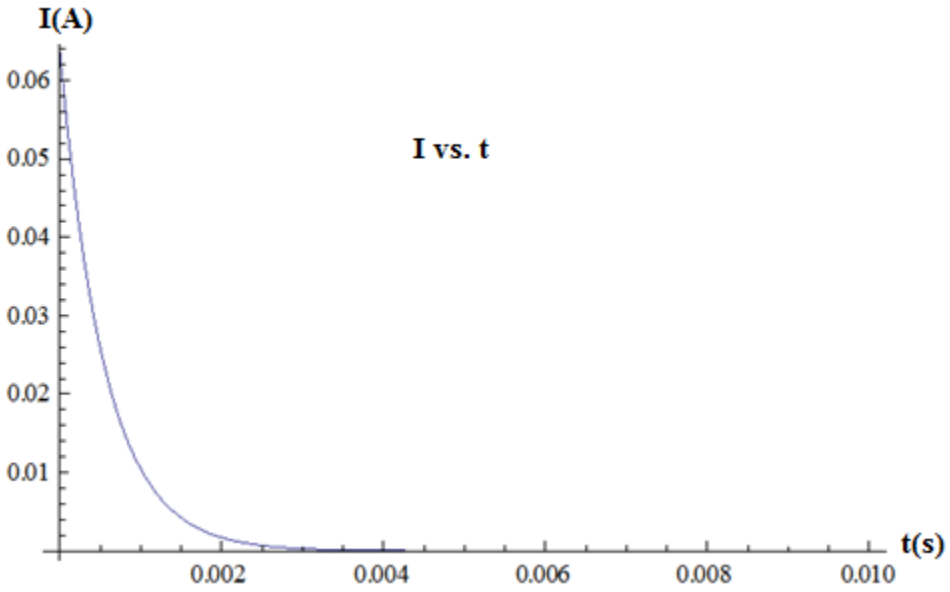


Fig. 3.11: Current dissipation rate.

Where:

r = resistance of the solenoid.

l = inductance.

$I_0$= initial current.

The power supply used to produce a field within the solenoid is the Agilent model 6611c DC power supply, serial number MY43001519. The specifications of this instrument are as follows:

- Output Voltage: 0-8V
- Output Current: 0-5A
- Programming Accuracy: 5mV ± 5% or 2mA ± 5%
- Ripple and Noise:
    - Voltage (rms/p-p): 0.5mV/3mV
    - Current (rms): 2mA

Due to an extraneous amount of noise produced by both the power supply and external field induction, modifications have been made to the field circuit. These modifications include a relay switch, rated at 12A/250VAC, powered by a second Agilent model 6611c (serial number MY43001520), and a 4.7µF capacitor placed in parallel with the solenoid. The amount of current needed to throw the relay is 0.06A. A diagram is shown in Fig. 3.12.

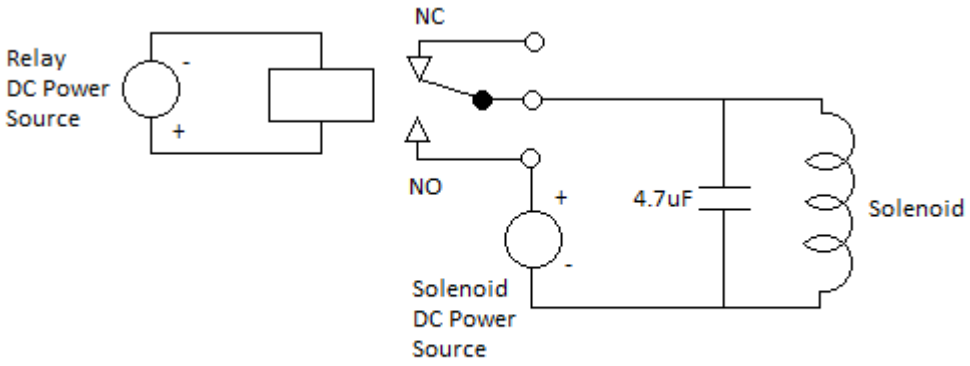


Figure 3.12: Solenoid Circuit. The solenoid is connected to a twisted pair of single core wires that lead to a 5-pin military style connector above the top of the flange. Only pins 1 and 4 are used; the positive and negative lead, respectively.

## 3.4 Data Collection

Data collection is done through the analog interface connector located on the rear panel of the Quantum Design Controller. Two Keithley model 2002 digital multimeters are connected to this interface, receiving and displaying each SQUID signal in Volts. Keithley A, serial number 1216354, is reading measurements from SQUID A and Keithley B, serial number 1216353, is reading SQUID B.

The connector used is a 26-pin high density "D" leading to four banana-style plugs. Pins 1 through 4 are the only pins used on this connector with the following assignments:

- Pin 1: Channel 1 Signal
- Pin 2: Channel 1 Return
- Pin 3: Channel 2 Signal
- Pin 4: Channel 2 Return

Each channel pin connects directly to its respective input on each multimeter.

## 3.5 Helium Dewar and Level Detection

The magnetometer apparatus is housed within a custom designed, super insulated helium Dewar manufactured by Precision Cryogenics Systems, Inc. shown in Fig. 3.13. This Dewar is model PVS-4.55/45.0 and the observed helium depletion rate, with the magnetometer installed, is approximately 0.25 L/hr. Operating depletion rate is approximately quadruple that, at .95L/hr. This means that the Dewar must be refilled every 28-36 hours during continual experimentation, depending on the heater output on the Lakeshore as well as the initial volume of helium transferred.

In order to allow the Dewar to cool to helium temperature without excessive boil-off, one must first fill the system with liquid nitrogen and cool to 77K. Then, using helium gas, pressurize the Dewar from the top flange and evacuate all of the nitrogen from the system. It is important to wait up to several hours until the temperature on the cryostat reads between 85 and 90K to ensure that all of the liquid has been depleted. If there is still liquid nitrogen remaining at the bottom of the Dewar, it is necessary to pressurize the system again with gas helium and force the liquid out. Once a completely empty, yet still cold Dewar has been confirmed, helium transfer can begin.

The helium level is monitored using a simple four-lead device, connected to the back of the Quantum Design Controller. This connection leads to a 109.25cm piece of NbTi superconducting wire, twisted and secured through a nylon tube that runs along the side of the magnetometer. The superconductor connects above the magnetometer flange with a 5-pin military style connector that continues to the back of the Quantum Design. The measured resistance at room temperature is 1.4Ω. Similar to that of the solenoid connection, only pins 1 and 4 are used.

- Pin 1 is the positive lead.
- Pin 4 is the negative lead.

From this connection, the leads are wired into a four-lead arrangement that connects to the Quantum design with the following pin assignments:

- Pin 1: Positive Current
- Pin 2: Negative Current
- Pin 3: Positive Voltage
- Pin 4: Negative Voltage

The heart of the magnetometer: the SQUIDs, gradiometers, solenoid, sapphire rod with temperature connections, and the sample are all contained within the double layer vacuum jacket located in the bottom third of the Dewar. These components are shielded with lead sheeting that is molded around the G10 structure. The majority of the helium is stored in the middle third, the largest part of the Dewar, capable of holding up to 70L. The magnetometer has no major components in this zone, limiting the amount of material needing cooled, in return reducing the overall rate of helium boil-off. The top third of the Dewar contains 5 separated copper disks leading to Styrofoam insulation just under the top flange. This aids in the reduction of interaction between the internal system temperature of 4.2K and the outside temperature of approximately 300K. A complete drawing of the magnetometer is shown in appendix A.

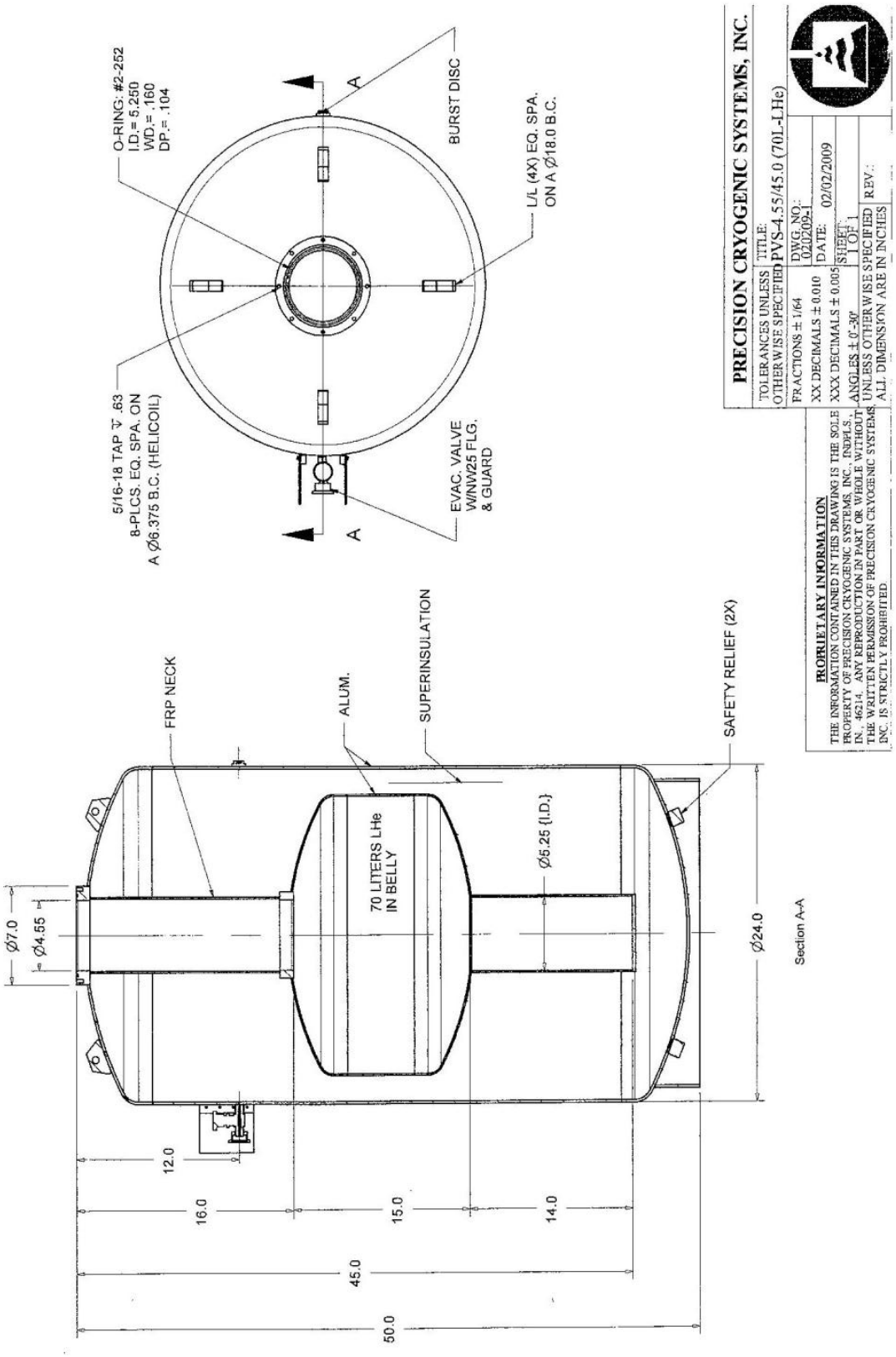


Figure 3.13: Helium Dewar.

## 3.6 Automation and Programming

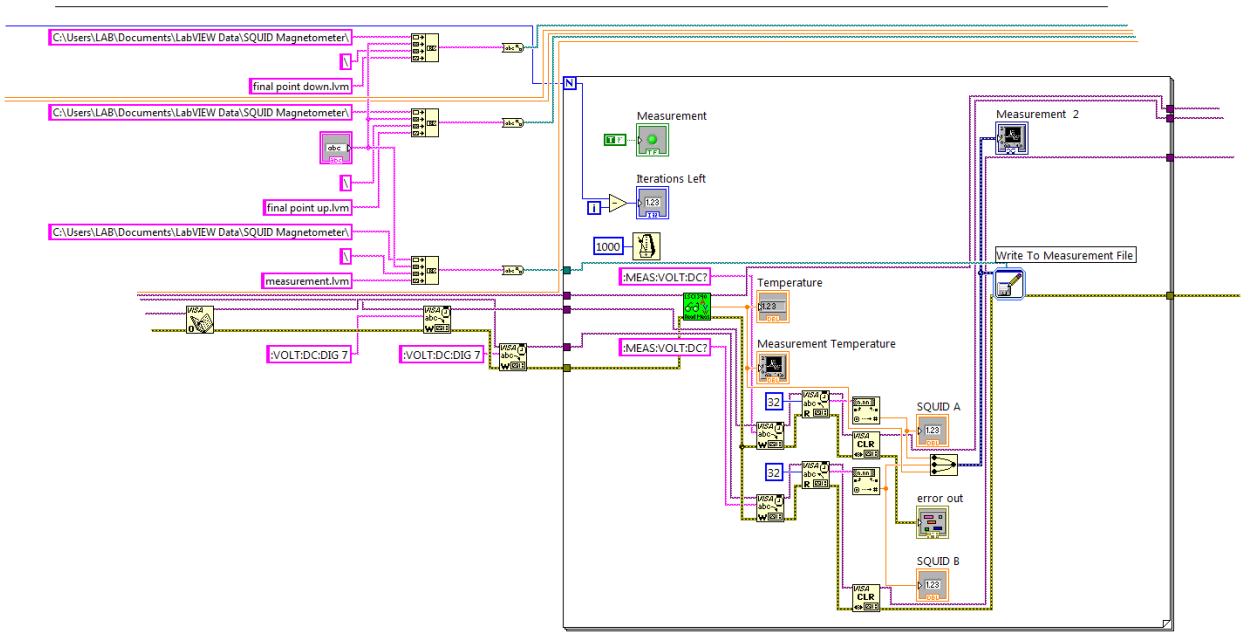


Figure 3.14: LabVIEW programming example.

With the number of active components utilized for the magnetometer, automation is necessary to ensure a repeatable sequence of experimental events. In order to automate the system, two programs have been written using National Instruments LabVIEW 8.6. In this chapter, we explain step-by-step the order of operations of each program, including code diagrams. We also include this section to act as an operations and troubleshooting guide.

### 3.6.1 Interface Set-Up

Each of the six control boxes described in the previous chapter are connected via General Purpose Interface Bus (GPIB) to the CPU. The CPU system used is a Dell Precision T3400 with an Intel Quad Core 2 processor. The physical connection arrangement can be seen in Fig. 3.14

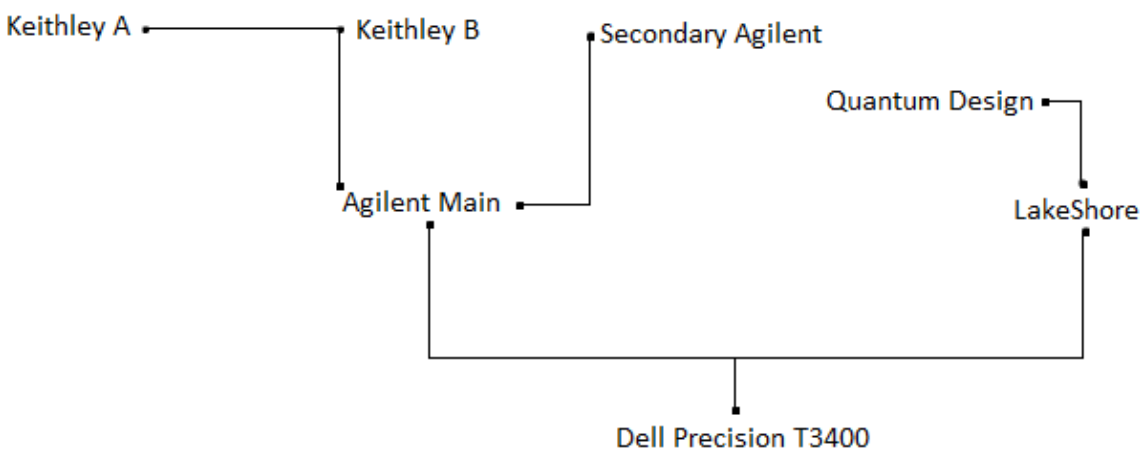


Figure 3.15 GPIB Connection Arrangement.

Each control unit is daisy-chained to the CPU such that no connection point exceeds three GPIB connectors. Keithleys A and B are connected in series (A to B) to the main Agilent, the power supply to the solenoid. The secondary Agilent, the power to the relay system, is connected directly to Agilent Main. Agilent Main connects directly into the CPU. The Quantum Design controller connects into the LakeShore, which in turn also connects directly to the CPU.

All of the control units used in this system are marketed as "plug and play", however, if an instrument is not recognized by the computer, one can troubleshoot or manually connect to a unit using the National Instruments Measurement and Automation Explorer, a secondary program installed with LabVIEW. Each device has its own individual GPIB address number recognized by the CPU that can be changed manually on the device. An alias may be assigned to an instrument to use instead of the GPIB assignment. Table 3.2 lists each device, its GPIB address,

and any alias assigned to an instrument. No two devices can share the same address concurrently.

Table 3.2 List of GPIB Addresses and Aliases

| **Instrument Name** | **GPIB Address** | **Alias** |
|---|---|---|
| Agilent Main | GPIB0::14::INSTR | N/A |
| Agilent Secondary | GPIB0::5::INSTR | N/A |
| Keithley A | GPIB0::16::INSTR | keithley00 |
| Keithley B | GPIB0::17::INSTR | keithley01 |
| LakeShore | GPIB0::12::INSTR | N/A |
| Quantum Design | GPIB0::15::INSTR | N/A |

### 3.6.2 Long Time TRM Decay Measurement Program

The long-time decay program was built for those experimental runs requiring essentially no waiting time and very long measurement times. Shown in Fig. 3.15, it is designed to operate one time per parameter set. The user can set parameters such as the measurement temperature, maximum temperature, glass transition temperature, field strength and number of data points. This section describes two aspects of the long-time decay program: the programming code itself and the interface arrangement.

The program begins with an initialization sequence connecting all six devices noted in the previous section to the CPU. A VISA Open command writes to each individual instrument, and upon response, the program opens communications through GPIB, as shown in Fig. 3.16. A dialog box will display, pausing the program and inquiring whether or not the parameters are

correct. If the parameters are indeed correct, a confirmation is sent to the program to continue operation. At this point all parameters are locked into the program and cannot be altered. If for some reason the parameters are incorrect, the program halts execution and any necessary changes can be made before restarting the run.

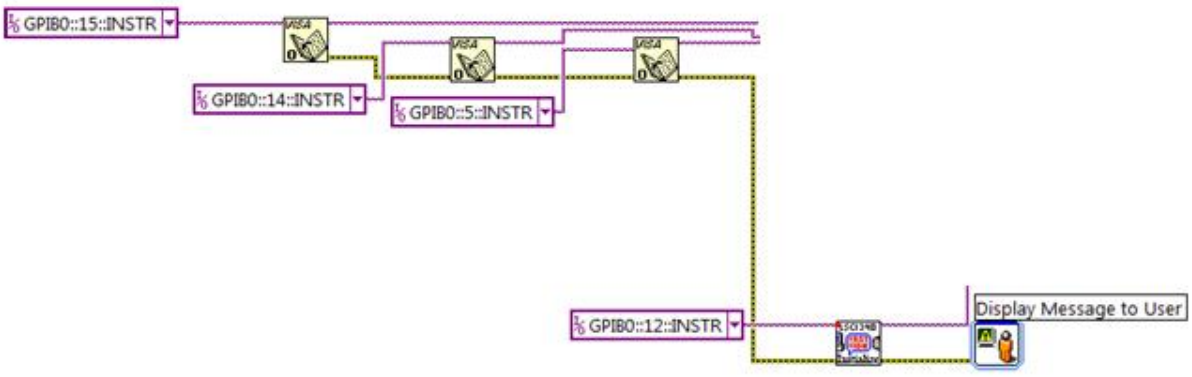


Figure 3.16: Initialization sequence for programming using VISA control standards. Keithley multimeters appear far later in the program due to GUI organization, however they still initialize with the other equipment.

The first step in a TRM experiment requires the LakeShore controller to heat the sample to above the glass transition temperature, Fig. 3.17. The system ramps from helium temperature to the high temperature in quarter increments, i.e. 25, 50, 75, 100 percent the set point value to avoid an overload, resulting in a burnt out heater coil. As the temperature is increasing, a command is sent to the primary Agilent to ensure there is no current output to the solenoid, in the event that the relay switch was on. Once the high temperature set point has reached its value with ±0.1K, both Agilents are turned on and the cooling protocol begins.

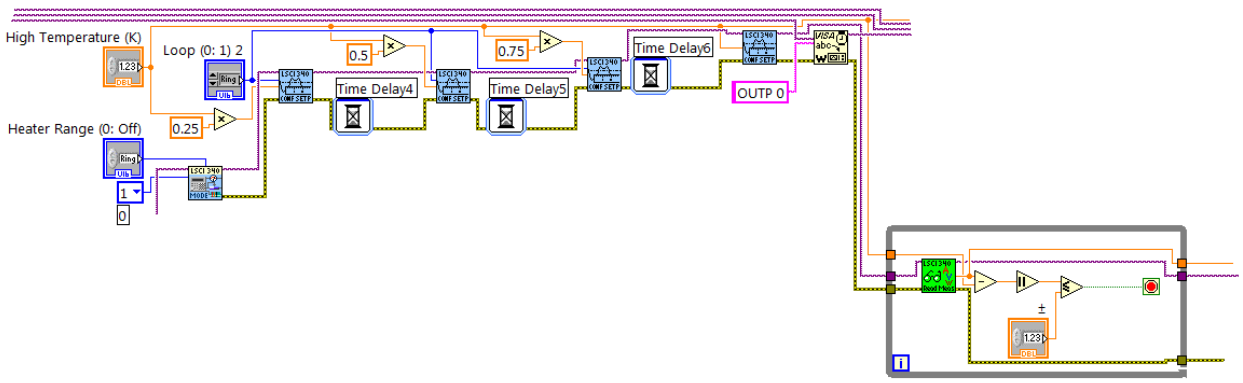


Figure 3.17: LakeShore heating protocol.

The cooling protocol is perhaps the most important section of the program, as the sample's TRM response pattern is dependent on a quick transition below $T_g$ [16]. The optimum cooling process should take approximately 20 seconds or less. This cool down procedure sets the temperature at which the measurement takes place, below the glass transition temperature, and lowers the heater power just enough for a quick decrease in temperature. Once the glass transition temperature is surpassed, the system introduces small increases in heater power at 5 second intervals to bring the temperature back up to its measurement set point. The point of manually controlling the heating coil is to avoid any harmonic oscillation caused by the temperature controller as this slows down the cooling protocol significantly.

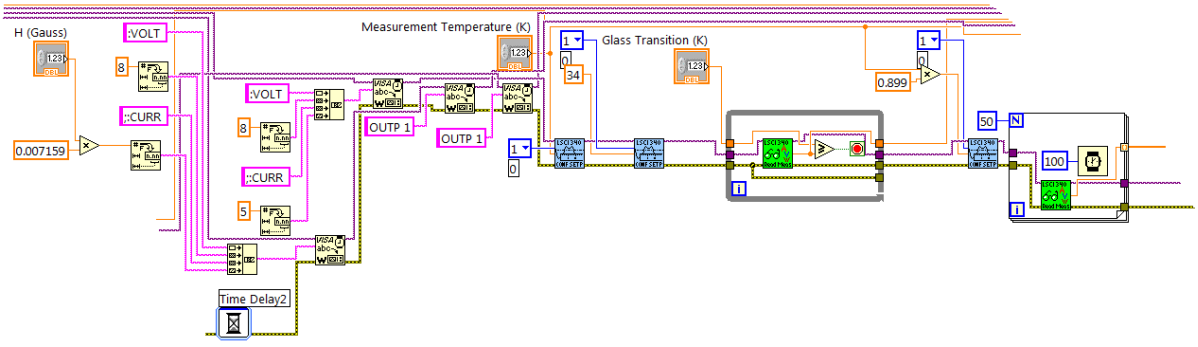


Figure 3.18: LakeShore cooling protocol.

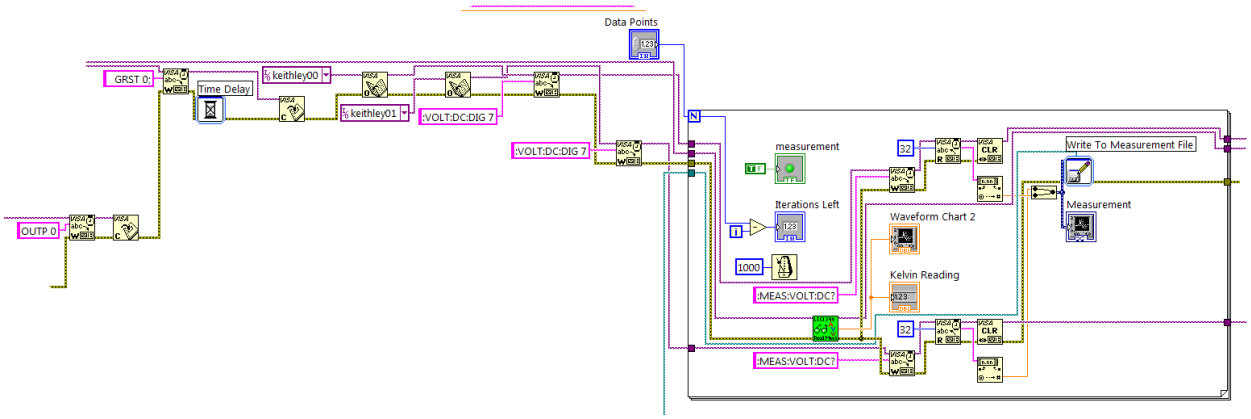


Figure 3.19: The Agilents turn off the solenoid, the SQUID controller performs a global reset, the Keithleys set precision, and measurements begin.

Once the cooling protocol is complete, a chart should appear under the interface tab 'Temperature' displaying the cooling curve. At this point both Agilents will shut off output and the Quantum Design with perform a global reset on the SQUIDs. There will be a 2 second delay as the SQUIDs come back online, and the Keithley multimeters will adjust to a 7-digit display. The measurement light on the status panel should illuminate and a countdown of data points left should begin, as the system takes decays measurements (Fig. 3.19). A real-time display can be viewed of the TRM decay under the 'Measurement' tab. The data collected is saved to the folder named before the program started. This folder can be found under C:\Users\LAB\Documents\LabVIEW Data\SQUID Magnetometer. In this folder will be three files: a temperature file, measurement file and a final point file.

Once the measurement loop is finished, the system heats back up slowly in increments above the glass transition temperature and the Keithleys record the final point of the measurement. After this point is taken, the GPIB buffers are cleared and the Keithleys are reset (Fig. 3.20). The temperature set point is set to 0 K to allow the system to cool back down to helium temperature, avoiding unnecessary boil off. The VISA is closed and the program has finished.

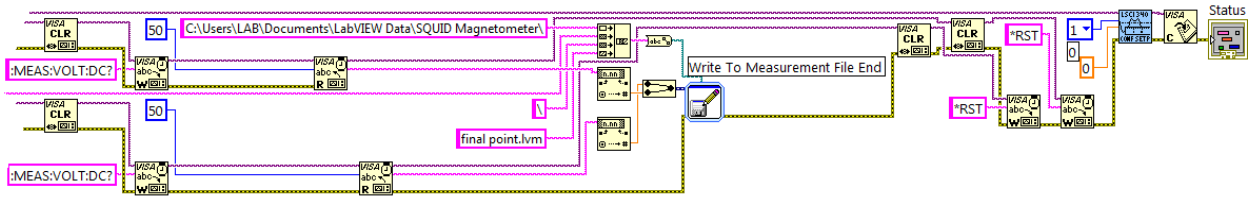


Figure 3.20: Final data point measurement.

The interface panel (Fig. 3.21) is divided into four separate tab categories: experiment set-up, temperature, measurement, and experiment status. The experiment set-up tab is where all parameters, as well as the experiment's folder name are entered before the run. The temperature tab allows the user to view the temperature curve of the cool down protocol as well as a live chart of the temperature fluctuations that may occur during measurement. The measurement tab displays a live chart for each measurement point relayed through the Keithleys. The experiment status tab displays all pertinent information relating to the run. This includes start and stop time stamps, current readings from each Keithley as well as the LakeShore, what step the program is on, and error statuses.

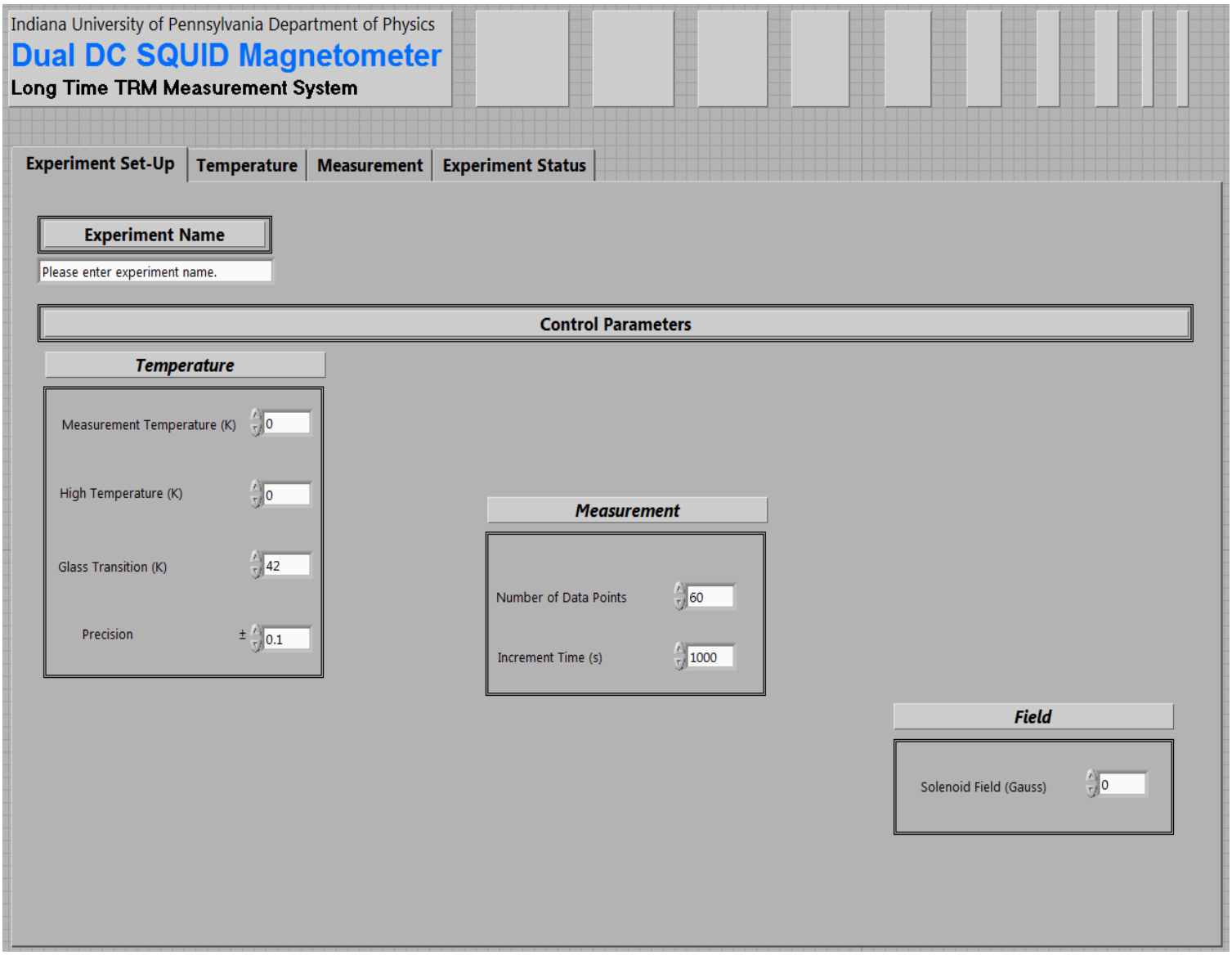


Figure 3.21: Long Time TRM Measurement System Interface.

### 3.6.3 Standard TRM Measurement Program

The standard TRM measurement program is designed for sets of shorter measurement times, each with its own waiting time. The interface can be seen in figure 3.22.

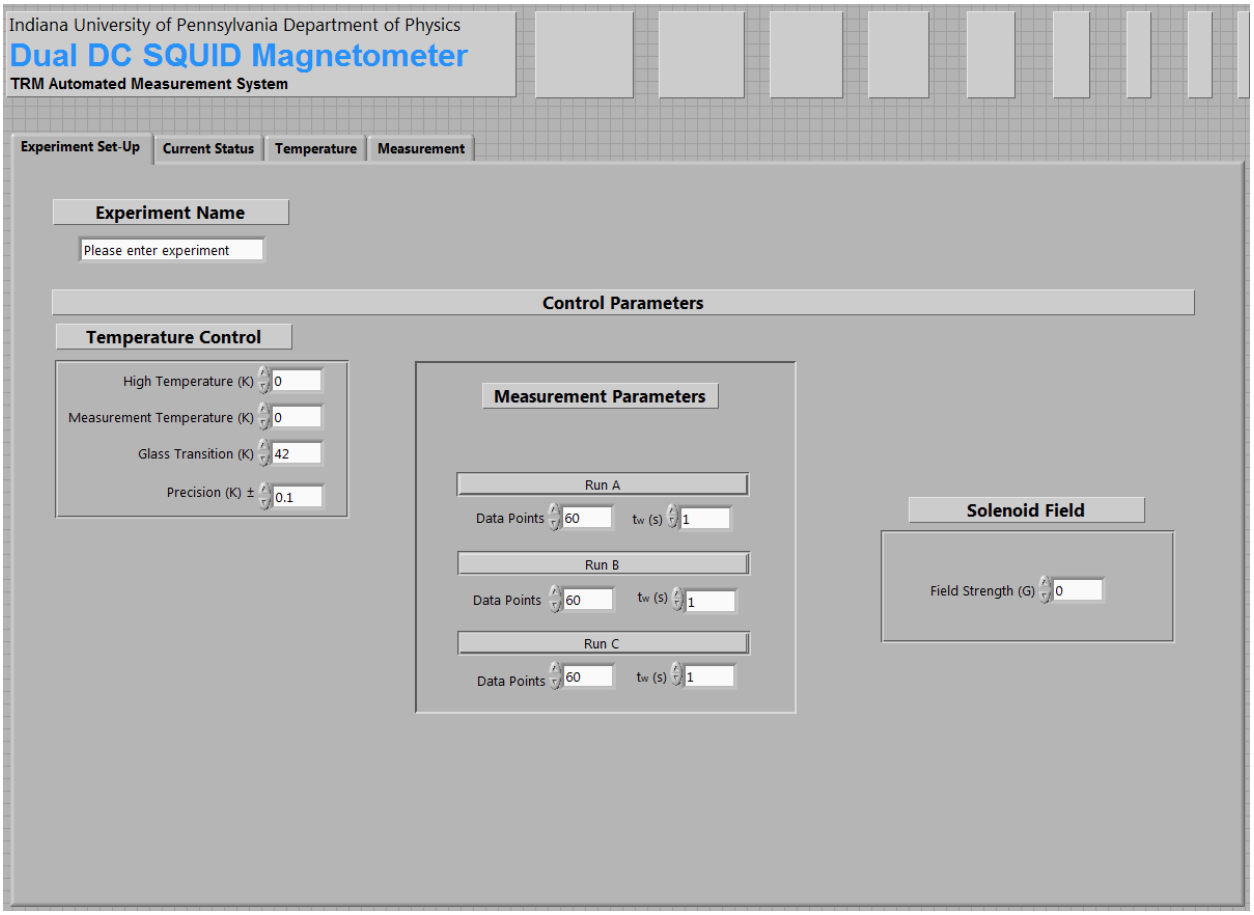


Figure 3.22: Standard TRM measurement system interface.

This program operates in the same manner as the long-time decay system with a few exceptions:

- The program is set to loop a total of five times, each iteration involving a different set of parameters for both the waiting time and the measurement time. If for any reason an iteration fails, the system will shut down.

- The parameters for each iteration should be entered before the experiment is started.

The programming diagrams can be seen in in appendix B; Part 1 is the Standard Measurement program and Part 2 is the Long-Time Measurement program.

# CHAPTER 4

# DATA

Much of this thesis project was spent developing the magnetometer itself, through thorough multidisciplinary research endeavors and many iterations of trial and error. Even with the amount of effort put into the physical and programming aspects of the machine, nothing surmounts to the value of the initial data output of the system. These crucial curves tell everything about the magnetometer, from signal to noise ratio to potential reasons for data distortion. This chapter begins with our sample characterization data, followed by the initial data output of the system as well as the process in which improvements were made thereupon.

## 4.1 Sample Characterization

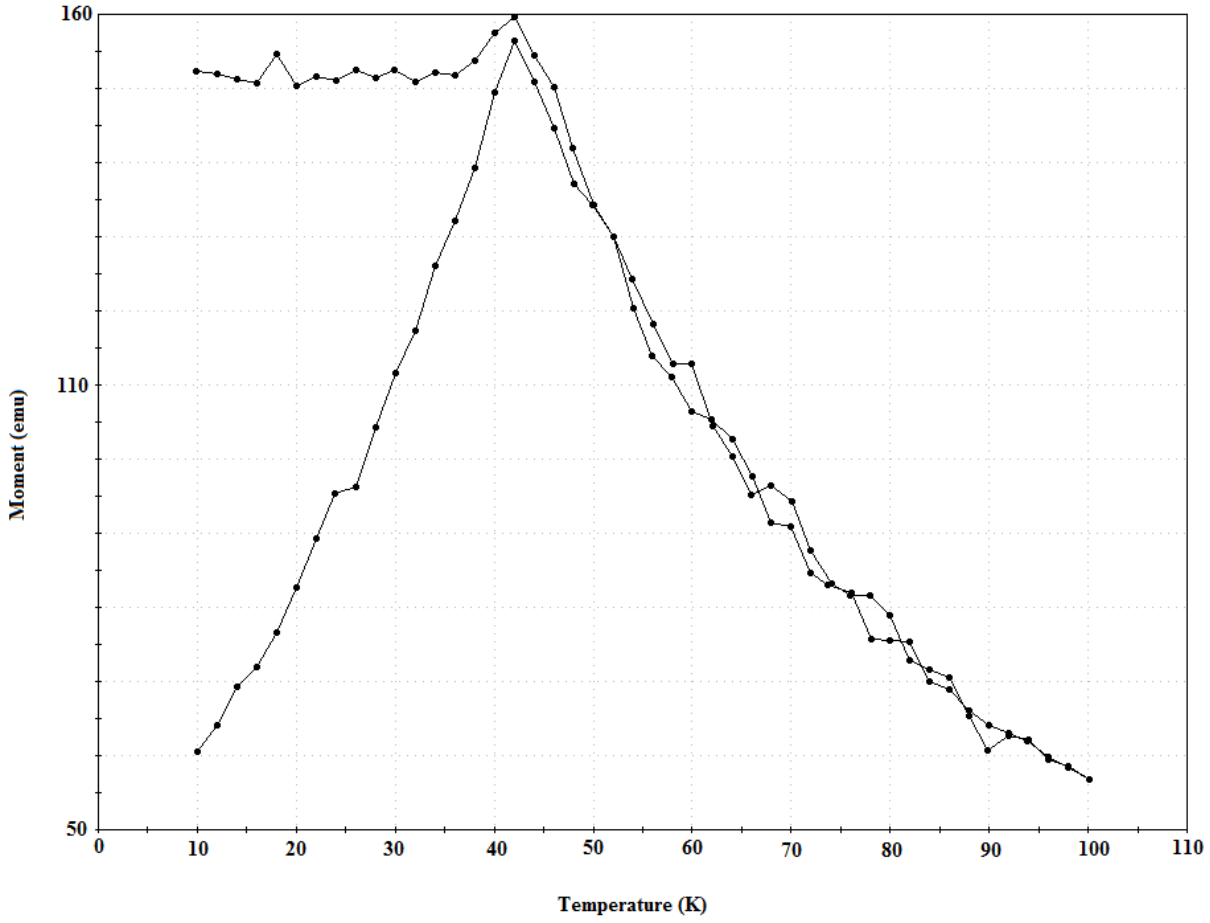


Figure 4.1: FCZFC sample characterization.

The spin glass sample used for this work was CuMn (10%) , machined into a 4mm diameter by 2mm thick disc and annealed at 600°C for 24 hours. After annealing, the sample was quenched in ice water and etched in nitric acid to remove any surface impurities from the machining process. A field-cooled, zero-field cooled (FCZFC) measurement was taken of the sample using a LakeShore Vibrating Sample Magnetometer (VSM) in order to determine the glass transition temperature. The process of which is as follows: the sample is cooled through $T_g$ with an applied

field of zero. Then the temperature is raised and when it reaches its initial value, the applied field is turned on and the sample is cooled once again. What should be noticed is that the field - cooled curve branches away from the initial zero-field cooled curve at a cusp. This cusp indicates the glass transition temperature. The difference between the two curves at temperature below $T_g$ is the overall amplitude of the TRM curve for said temperature [11]. The parameters for this run included field strength of 10 Gauss and a temperature span from 10K to 100K. The resulting curve (Fig. 4.1) displays a notable cusp, denoting $T_g$, at 42K.

While the sample's $T_g$ was determined in a field of 10G, the experimental procedure followed using the DDSM was at a field of 100G. A higher applied field shifts the Almeida-Thouless (AT) line, Fig. 4.2, the line that separates the paramagnetic state from the spin glass state in the (T,H) plane [19], and changing $T_g$ in such a way that is becomes lower as the field increases. Therefore the adjusted glass transition temperature was approximated to be 39.9K.

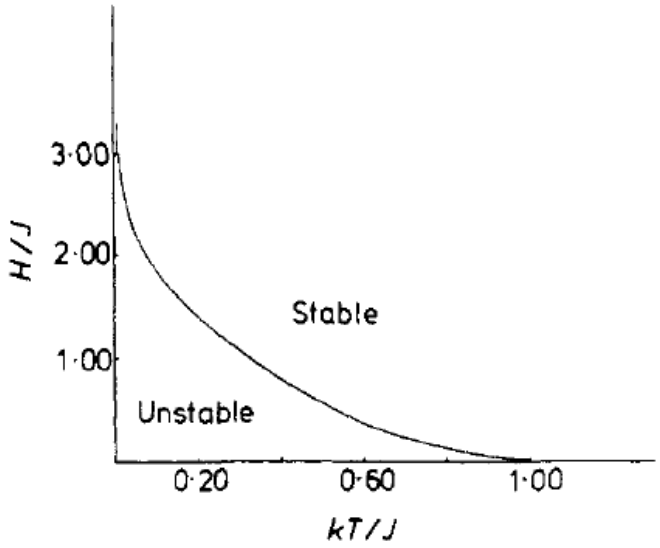


Figure 4.2: Plot of the de Almeida-Thouless line, corresponding to the boundary between paramagnetic and spin-glass states [19]. Stable and unstable refer to stability of replica symmetry.

## 4.2 Initial Data Output

As with any sort of experimental work, it is usually recommended to take preliminary data that follows previously established procedure. Thus, the first experiment attempted was the measurement of a $0.95T_g$ curve set at $t_w$ = 100s, 300s, 1000s and a ZTRM [16]. The initial settings of the DDSM included a SQUID range setting of 5V, the applied external field set to 20G and the total operation time set at approximately 17 hours. While the resulting data was not analyzable for a spin-glass (ZTRM sample in Fig. 4.3), this data was used to look at the system settings as a whole.

A very quick decay can be seen from Fig. 4.3; however the curve in its entirety has far too many random jumps to correct. These jumps are due to excess flux becoming trapped and then purged from the SQUID circuit in random intervals of time, offsetting the initial amplitude of the signal. Not only does this make detecting spin glass behavior difficult, it makes the baseline measurement untrustworthy in accuracy.

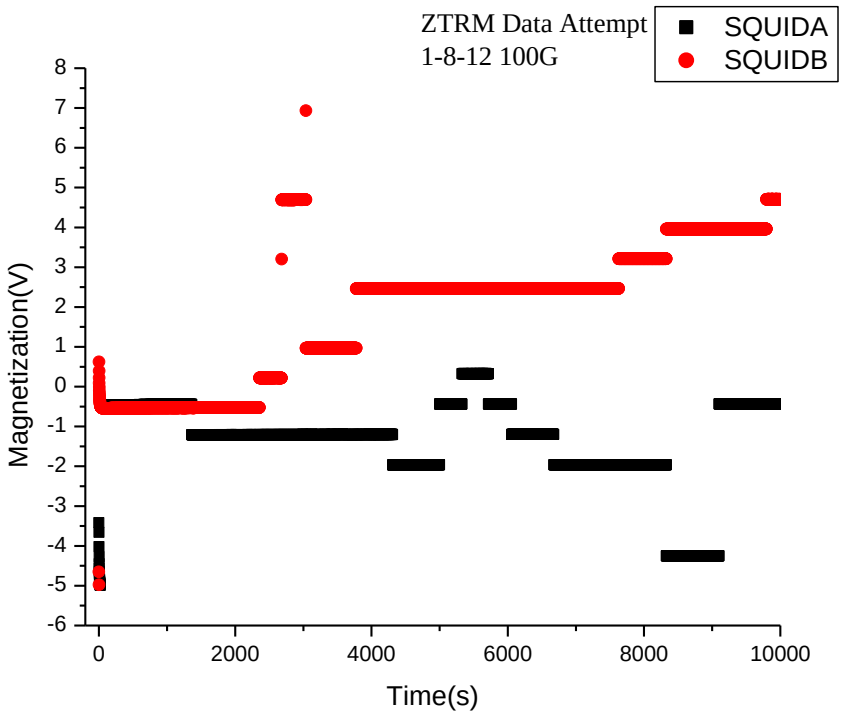


Figure. 4.3: ZTRM measurement before machine adjustments.

By adjusting the SQUID range to 5s (the "s" standing for "stable" or "slow"), the system readjusts into a more stable state, in turn reading the signal from the sample much slower. This decreased the amount of jumps significantly, from 30+ to approximately 2-4 per curve. The SQUID heater was also implemented by programming it to heat each SQUID during the last 20s of each $t_w$. This process completely purges the circuit of any trapped flux due to the excitation of the applied field. Another noted issue with this run was that the ZTRM decay reached a constant quickly and remained horizontal for the rest of the 10,000s run. In a spin glass, this decay does not reach any sort of equilibrium value in a tangible amount of time, if at all. This meant that the magnetometer was not necessarily seeing the sample. After further investigation, it was found that the sample was moved from its position in the pick-up coil by more than a centimeter.

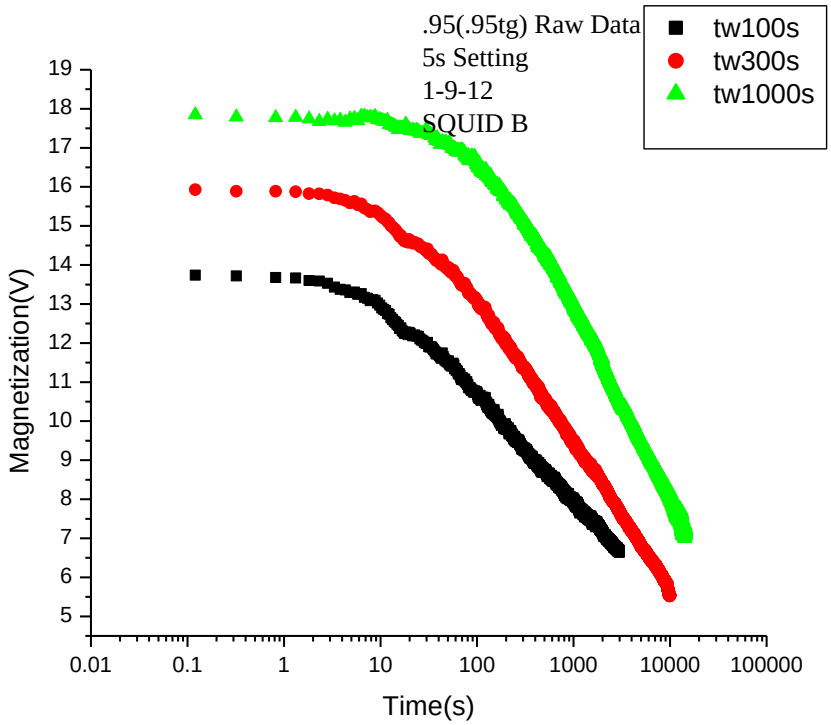


Figure 4.4: Initial TRM decay measurement after setting corrections.

Fixing the noted issues as well as changing the applied field to 100G, to amplify the signal, the curve output improved dramatically. Shown in figure 4.4, the TRM decays display notable curves showing that the sample is being measured as well as a lack of flux jumps. With this issue corrected, the next step is to take a look at the baseline measurements.

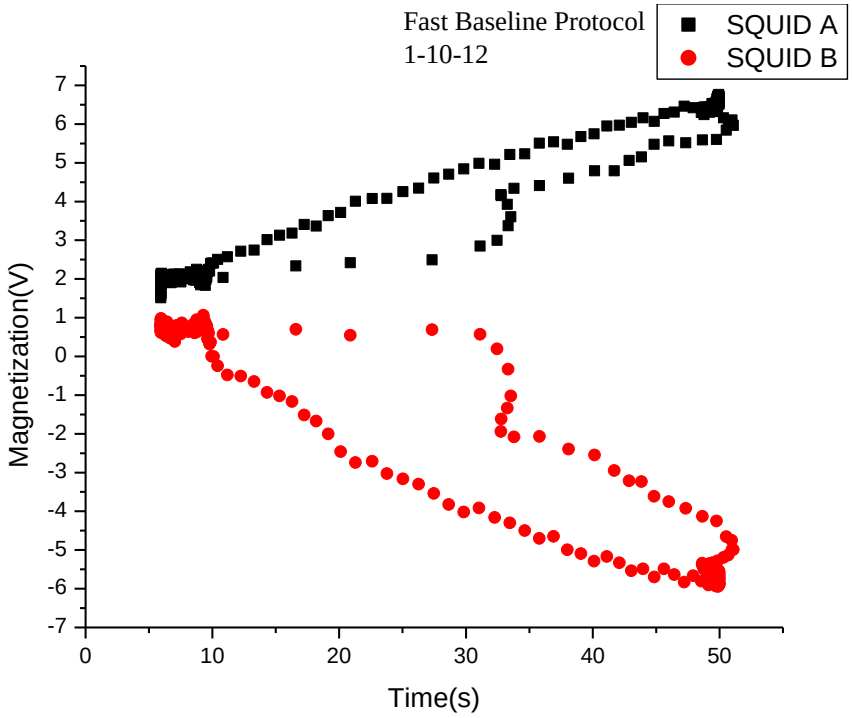


Figure 4.5: Fast Baseline Protocol.

The baseline measurement is perhaps one of the most important pieces of information needed to correct the spin-glass data taken from the SQUIDs. These numbers provide an absolute value for the last data point; they correct the offset of each individual curve due to SQUID resets. In other words, when each SQUID begins to read from the sample, the initial value is arbitrary in nature. The baseline shifts the entire curve to its actual value. Taking a look at the curves from the original protocol code in the programming in Fig. 4.5, the baselines were heavily distorted because of the rate in which the temperature was increased. The curve tells us that there is a delay in the temperature adjustment of the sample, most likely due to the heat gradient of the sapphire and surrounding Mylar. With this information, it was necessary to completely change the baseline protocol from a quick ramp in temperature to a much slower series of steps. As can

be viewed in appendix B, this sequence takes a magnetization reading every degree K from the measurement temperature to above the $T_g$, and then steps down again. This process takes about 20 additional minutes, but the output curve is clear (Fig. 4.6), and the baseline magnitude can be determined by measuring the greatest distance between each curve.

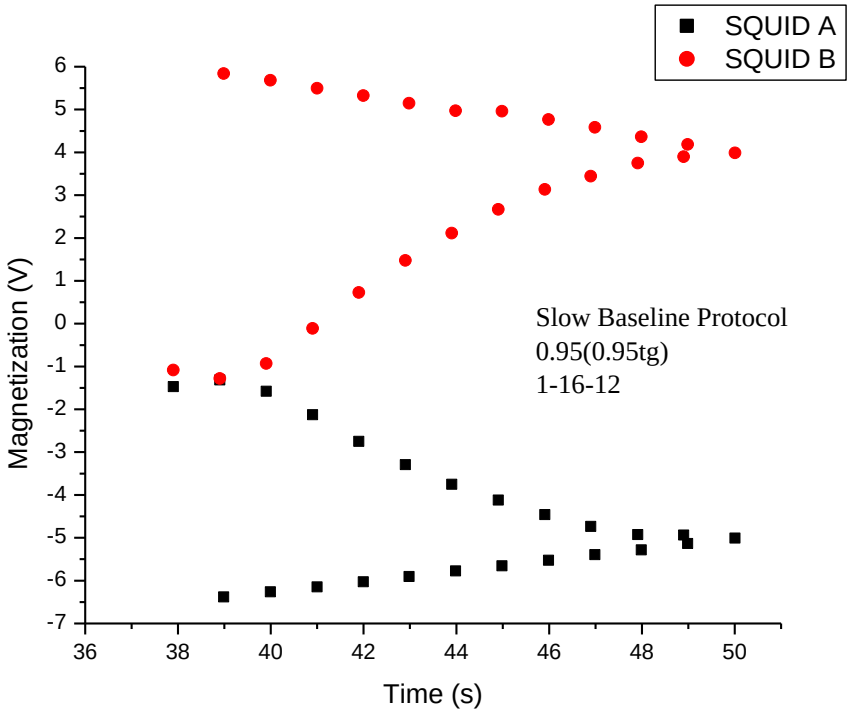


Figure 4.6: Slow Baseline Protocol.

With the baseline measurement established, four TRM sets were performed at 0.9, 0.95, 0.96, and $0.97T_g$. Fig. 4.8 displays all eight curve sets, from both SQUID A and SQUID B. From an initial inspection of the curve sets, it can be seen that the baseline is properly implemented and each individual $t_w$ curve shows its time dependence. S (t) calculations were performed confirming the location of each $t_w$, and an example of such curve sets is shown in Fig. 4.7. An overall look at the curves for each temperature shows that the farther the measurement

temperature is below the glass transition, the larger the amplitude of the signal becomes; characteristic of spin glass measurements.

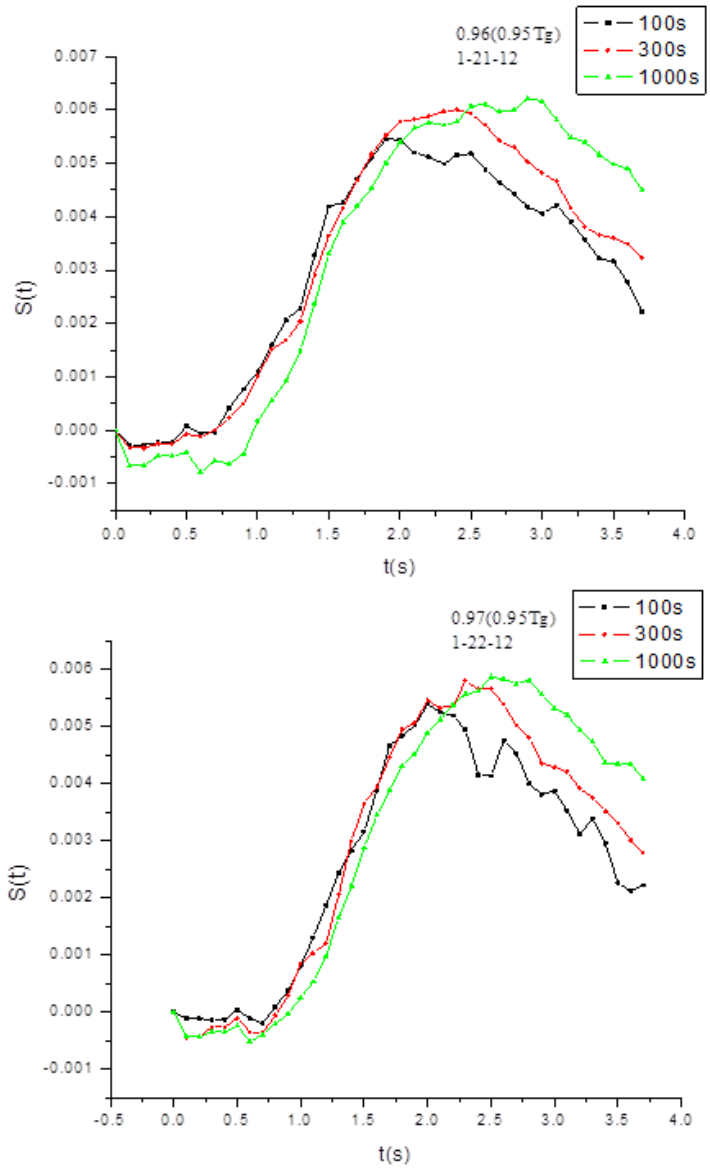


Figure 4.7: S(t) curve for $0.96(0.95T_g)$ and $0.97(0.95T_g)$.

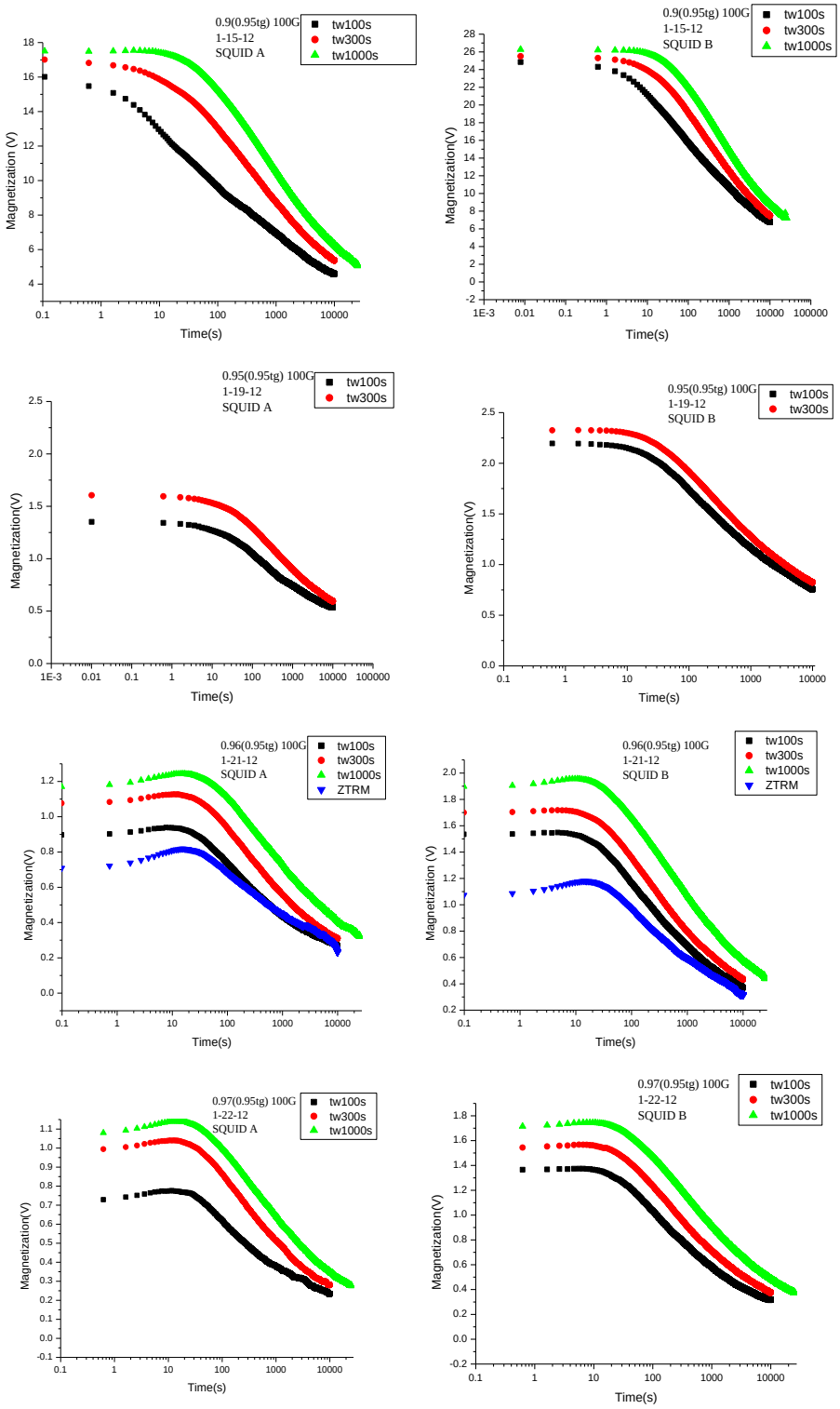


Figure 4.8: 0.9, 0.95, 0.96. 0.97$t_g$ runs.

The last question pertaining to the data, which is perhaps the most perplexing, shown from each curve, is the bending upward at the beginning of each decay. In comparison to the example decay shown in chapter 2, this is an abnormal response in a spin glass curve. Much thought has been put into the cause of this particular problem, and it has been determined by process of elimination to be the background remanence of the machine. Several attempts have been made to take a reasonable background measurement, all of which displaying similar patterns of a quick drop (less than 200s) to zero.

An interesting thing about these background decays is that they do not necessarily collapse perfectly on one another. That, and with one of the SQUIDs occasionally producing a drifting pattern, it is difficult to pin this inconvenience on one particular cause. When a function was determined that gave the best fit curve of the background decay, an attempt was made at subtracting the background from a set of TRM decays. From the results, it seems that one background curve does not work for all curves, thus one TRM measurement may be corrected but the next would be further flawed. There must be something unaccounted for in the decay. The only material that is notably different in this machine than the original, developed over 20 years ago, is Mylar.

Hysteresis measurements have been made on a sample of Mylar using the VSM. Through averaging the values obtained through each run, it has been determined that while Mylar is primarily paramagnetic, it does exhibit a small hysteresis (Fig. 4.9). This could be due to the process in which Mylar (biaxially-oriented polyethylene terephthalate) is manufactured, resulting in magnetic impurities. It was found that common impurities in Mylar can include Ca, P, Sb, Fe and Zn.

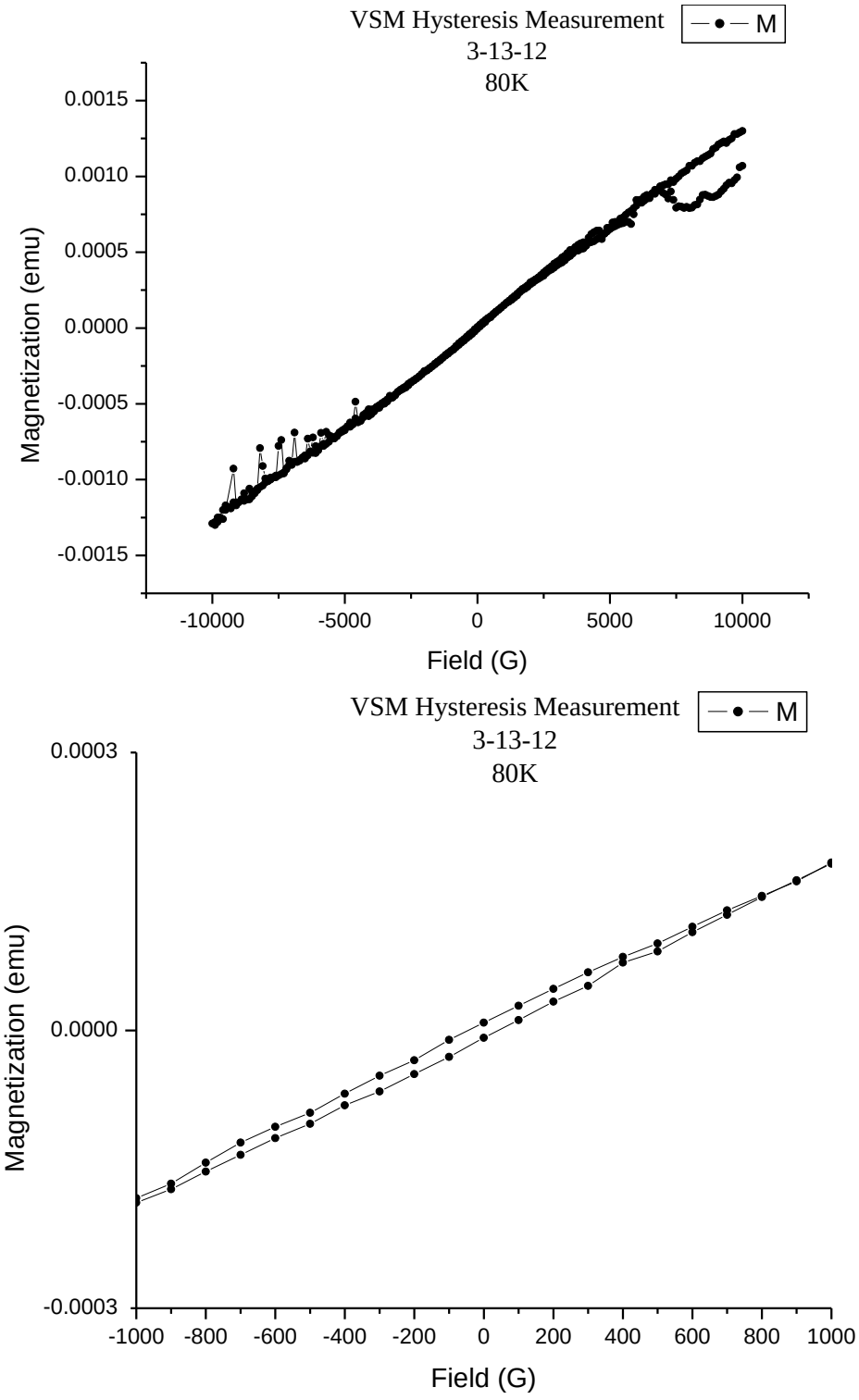


Figure 4.9: Mylar Hysteresis. Top: Full Hysteresis Curve. Bottom: Magnified curve about field = 0.

# CHAPTER 5

# CONCLUSIONS

This work was done under the presumption that data would be acquired pertaining to the end of aging in the spin glass phase. Through the use of statistical mechanics and thermodynamics principles, the evolution of the spin glass model was interpreted and further confirmed through experimentation with TRM measurements. The majority of the time spent was in preparation of the search for the 'End of Aging', thus almost two years of work was put into the dual DC SQUID magnetometer.

In comparison to the previous generation of this machine, there were a few changes made that were both proactive and inhibitive of proper data output. The most obvious difference is the addition of the second SQUID sensor. This sensor has allowed for the comparison between TRM decay curves, confirming reliability of the output data. In most cases, both SQUIDs operated beautifully with mirroring curves. Occasionally one SQUID would become hyperactive and remain in reset mode, or demonstrate drifting, but other one was there to continue the measurement.

The second most crucial change was the addition of the Mylar insulation over the sapphire rod. This change was not as rewarding as it was found that Mylar has a small hysteresis. This issue is amplified in our measurements due to the sensitivity of the SQUID magnetometer versus the VSM. The next step in the continuation of our experiments in spin glass dynamics would be to remove the Mylar casing from the sapphire, hopefully improving the TRM decay curves, and working from that point.

Overall, the time and effort invested into the building of the SQUID magnetometer was well worth the results. The ‘SQUID’ is a highly functional, sophisticated machine (sans the Mylar), and will prove to be a valuable piece of equipment when we are ready to find the ‘End of Aging’.

REFERENCES


1. Cannella, V.; Mydosh, J. A. *Phys. Rev. B.***1972**, *6*, 4220.
2. Edwards, S. F.; Anderson, P. W. *J. Phys. F*. **1975**, *5*, 965.
3. Sherrington, D.; Kirkpatrick, S. *Phys. Rev. Lett.* **1975**, *35*, 1792.
4. Parisi, G. *Phys. Rev. Lett*. **1979**, *43*, 1754.
5. Mattis, D. C. *The Theory of Magnetism: An Introduction to the Study of Cooperative Phenomena*.; Harper & Row: New York, **1965**; Chapter 2.
6. Weiss, P. *J. Phys*. **1907**, *6*, 661.
7. Griffiths, J. *Introduction to Electrodynamics*, 3rd ed.; Prentice-Hall: Upper Saddle River, 1999.
8. Binder, K.; Young, A. P.; *Rev. Mod. Phys*. **1986**, *58*, 801.
9. Istrail, S. *Statistical mechanics, three-dimensionality and NP-completeness: I. Universality of intractability for the partition function of the Ising model across non-planar surfaces*; STOC '00 Proceedings of the thirty-second annual ACM symposium on Theory of computing. **2000**, 87-96.
10. Gould, H.; Tobochnik, J. *Statistical and Thermal Physics with Computer Applications*.; Princeton: Princeton, **2010**; Chapter 5.
11. Joh, Y. G. Spin Glass Dynamics: Developing a Hierarchical Model from Experiment. Ph.D. Dissertation, University of California Riverside, Riverside, CA, **1997**.
12. Lederman, M.; Orbach, R.; Hammann, J. M.; Ocio, M.; Vincent, E. *Phys. Rev. B.* **1991**, *44*, 7403.
13. Joh, Y. G.; Orbach, R. *Phys. Rev. Lett*. **1996**, *77*, 4648.
14. Kenning, G. G.; Rodriguez, G. F., Orbach, R. *Phys. Rev. Lett.* **2006**, *97*, 057201-1.

15. Hammann, J. M.; Ocio, M.; Vincent, E. *Europhys. Lett.* **1986**, *2*, 45.

16. Sibani, P.; Kenning, G. G. *Phys. Rev. E.* **2010**, *81*, 011108-1.

17. Rodriguez, G. F.; Kenning, G. G.; Orbach, R. *Phys. Rev. Lett.* **2003**, *91*, 037203-1.

18. Lederman, M. Dynamics of Random Systems: Spin-Glasses and Random Fields. Ph.D. Dissertation, University of California Los Angeles, Los Angeles, CA, **1991**.

19. de Almeida, J. R. L.; Thouless, D. J. J. *Phys. A: Math. Gen.* **1978**, *11*, 983.

# Appendix A- Magnetometer Drawings

This appendix contains drawings of the magnetometer structure. Fig. A.1 is a three-dimensional view of the entire magnetometer, without dimensions. Figs. A.2 and A.3 display a more detailed draft of the top and bottom halves of the magnetometer, respectively. These figures include all pertinent dimensions of the structure. The final figure, A.4, is a detailed close-up of the very bottom of the structure. This is where the sample rests inside the superconducting pick-up coils and the solenoid, encased in G10 housing and shielded with lead.

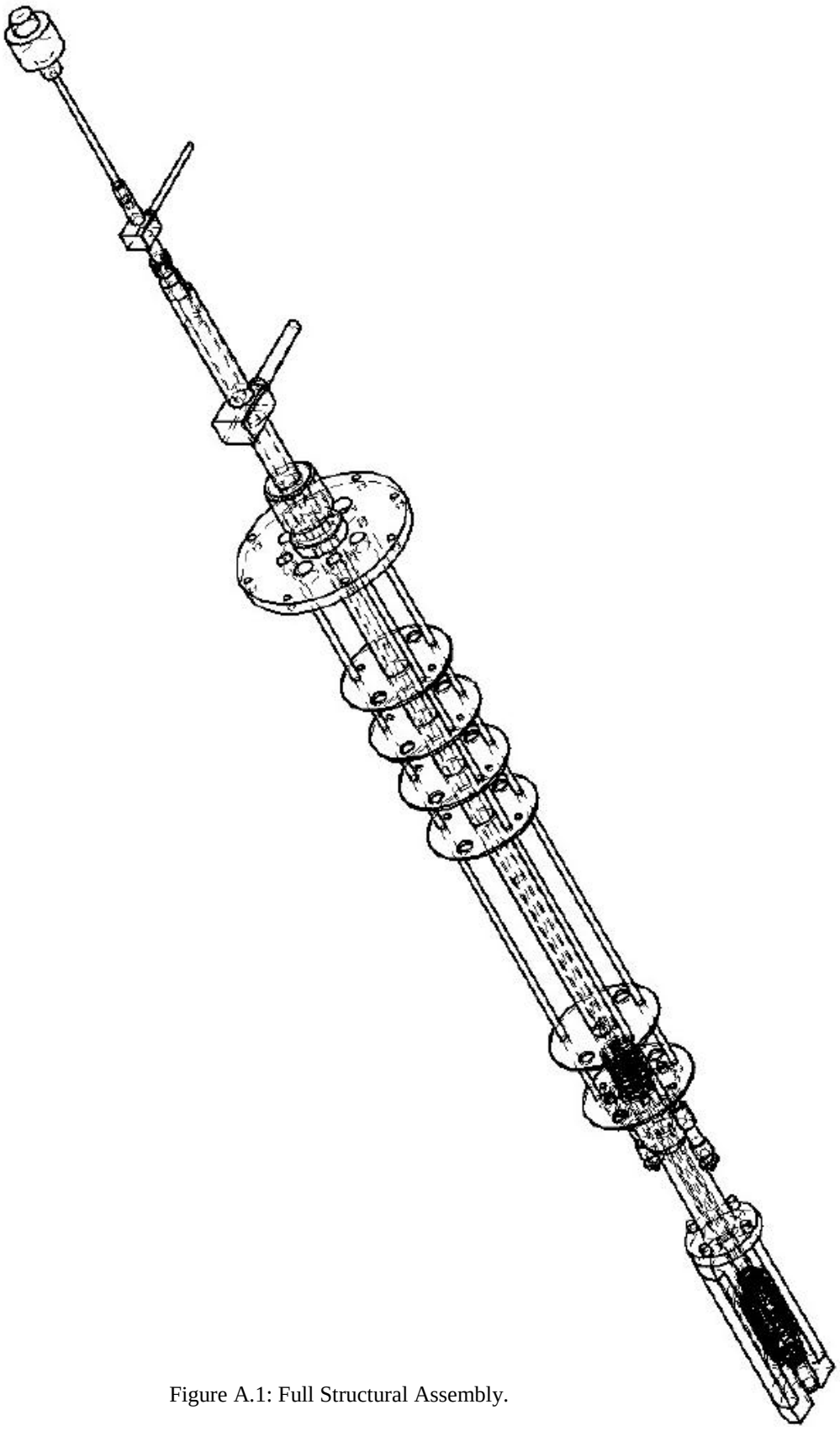

Figure A.1: Full Structural Assembly.

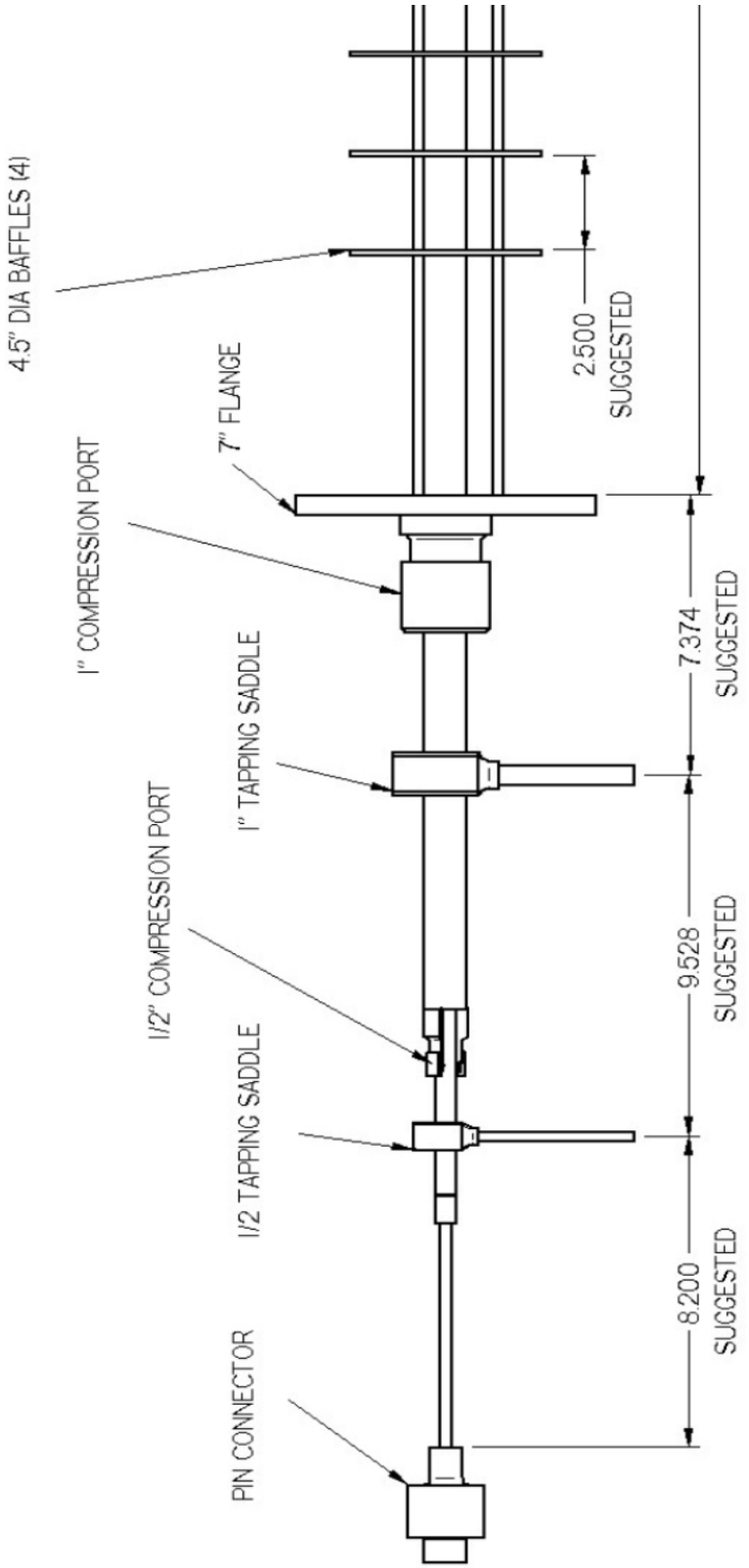


Figure A.**2**: Top half of magnetometer.

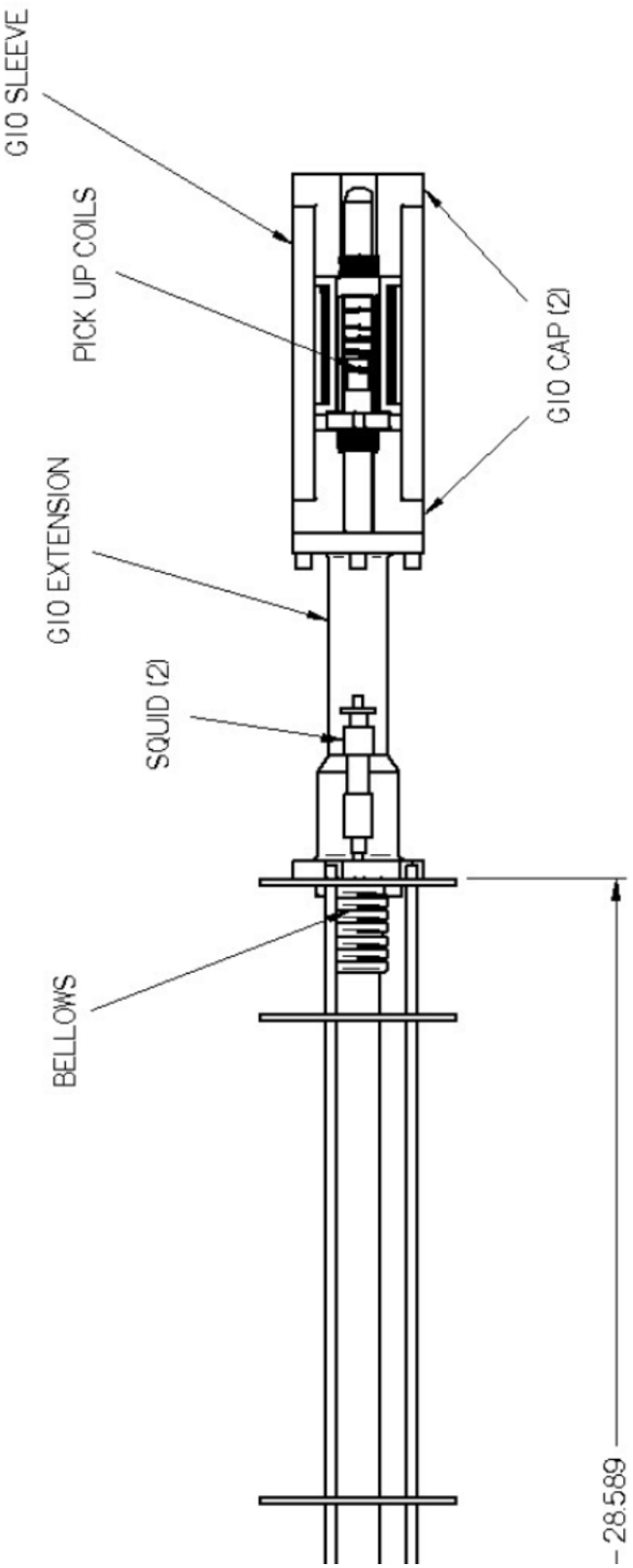


Figure A.**3**: Bottom half of magnetometer.

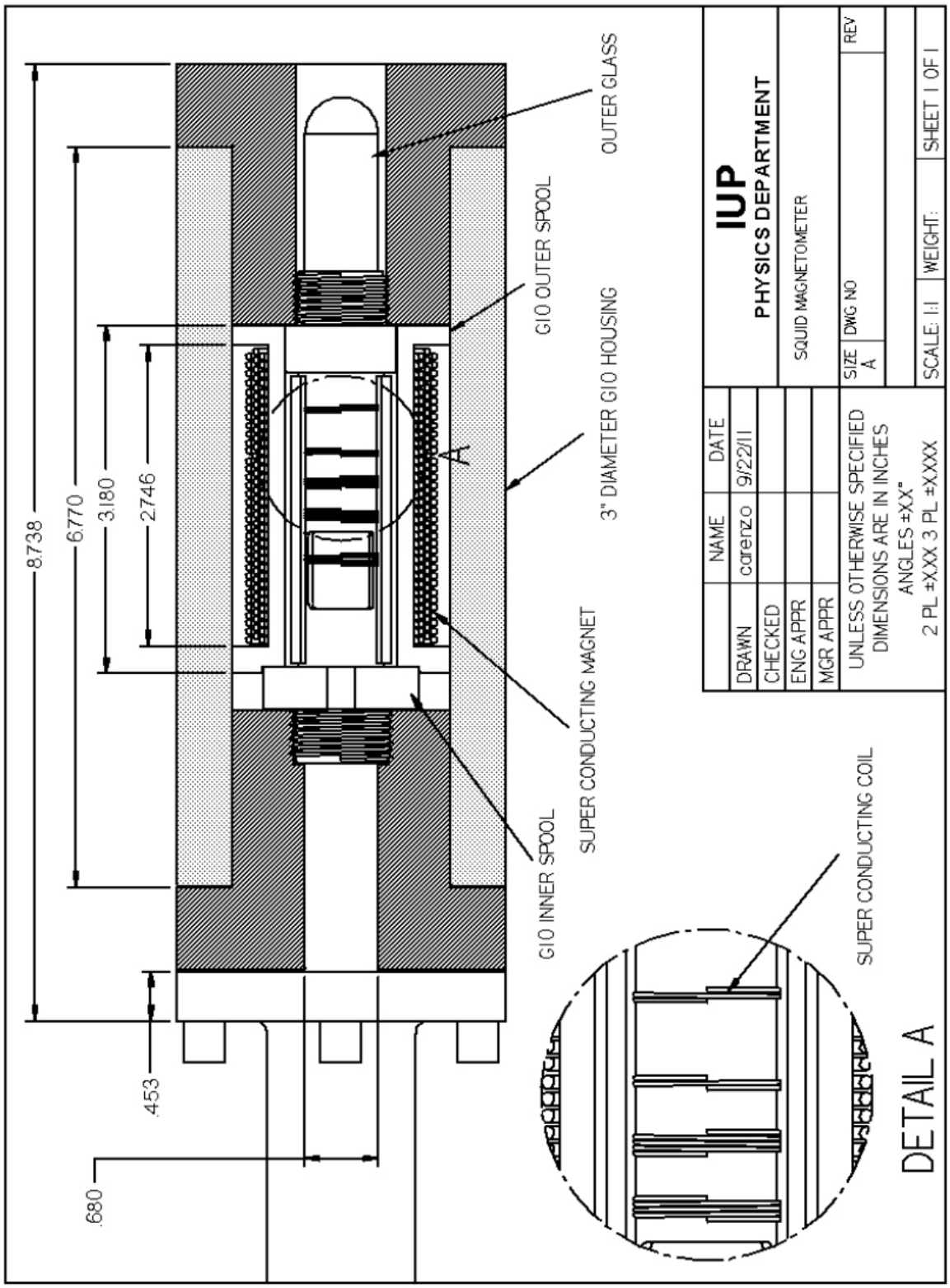


Figure A.4: Close-up of pick-up coils and solenoid in G10 encasement.

# Appendix B- Automation Programming

This appendix breaks down each of the two automation programs: the standard TRM program, and the TRM long-time decay program. Each program is divided into several sections, each of which describing a specific sequence of events. The following pages should be viewed in order, and it can be seen that each connection point has a corresponding letter to allow for a much simpler program reconstruction guide. Every icon in this program denotes a specific set of commands or functions. A detailed decription of each function can be found either by searching through the help menu of LabVIEW or by simply right clicking the icon in question.

## B.1. DDSM Standard Measurement Program

The standard TRM decay program is meant to perform measurements on relatively short time scales, with varying waiting times. For each experiment, the system will cycle up to a total of five times, each time changing parameters such as waiting time and measurement time. Once the experiment is set up, complete with a folder directory, the program may begin. Fig. B.1 displays the program in its entirety and spans pages 83 -87 .

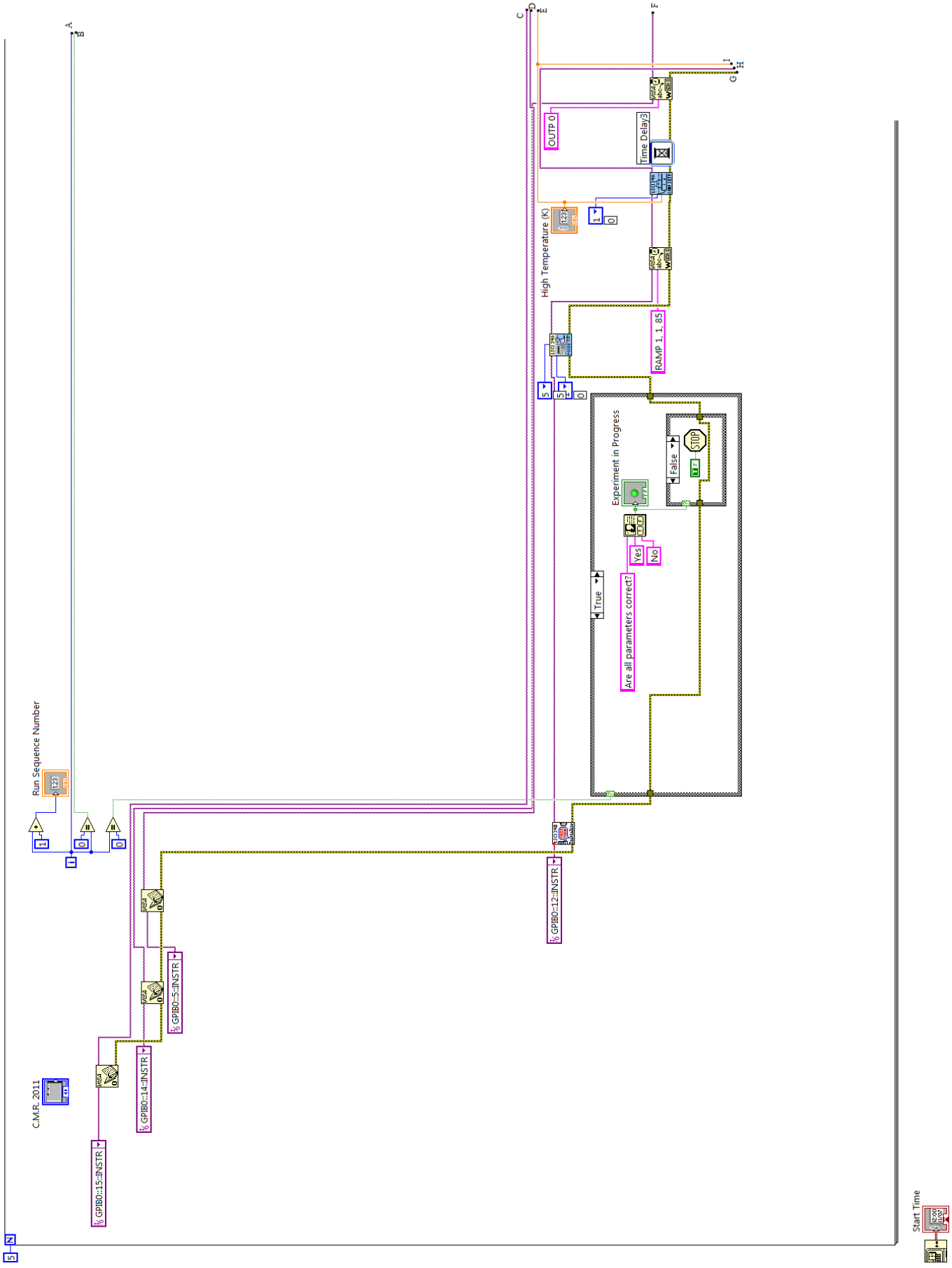
Run Sequence Number
C.M.R. 2011
GPIB0::15::INSTR
GPIB0::14::INSTR
GPIB0::5::INSTR
GPIB0::12::INSTR
High Temperature (K)
OUTP 0
Time Delay3
RAMP 1, 1.85
Experiment in Progress
Are all parameters correct?
Yes
No
True
False
STOP
Start Time

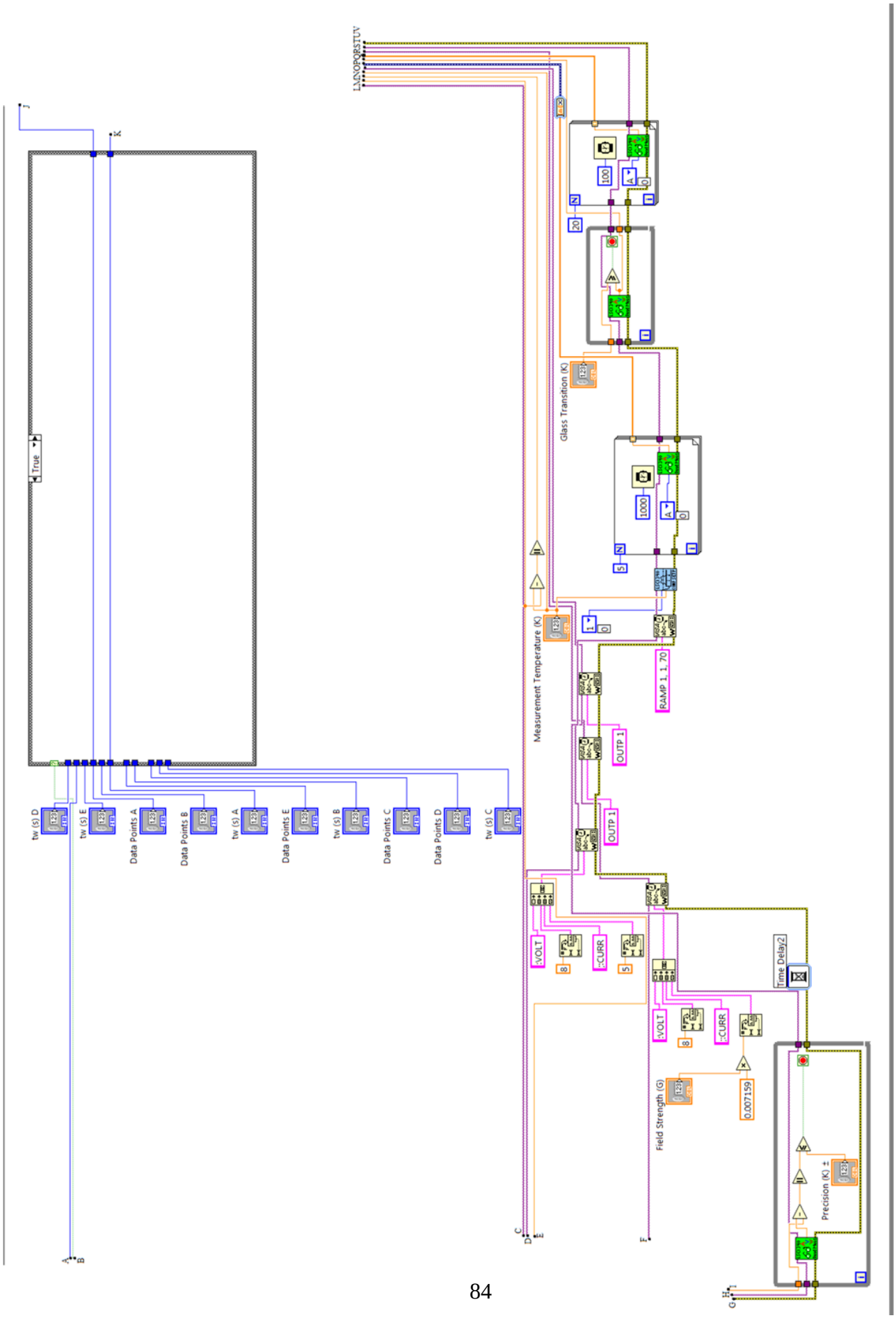
LMNOPQRSTUV
True
tw (s) D
tw (s) E
Data Points A
Data Points B
tw (s) A
Data Points E
tw (s) B
Data Points C
Data Points D
tw (s) C
Glass Transition (K)
Measurement Temperature (K)
RAMP 1, 1, 70
OUTP 1
OUTP 1
:VOLT
:CURR
:VOLT
:CURR
Time Delay2
Field Strength (G)
0.007159
Precision (K) ±

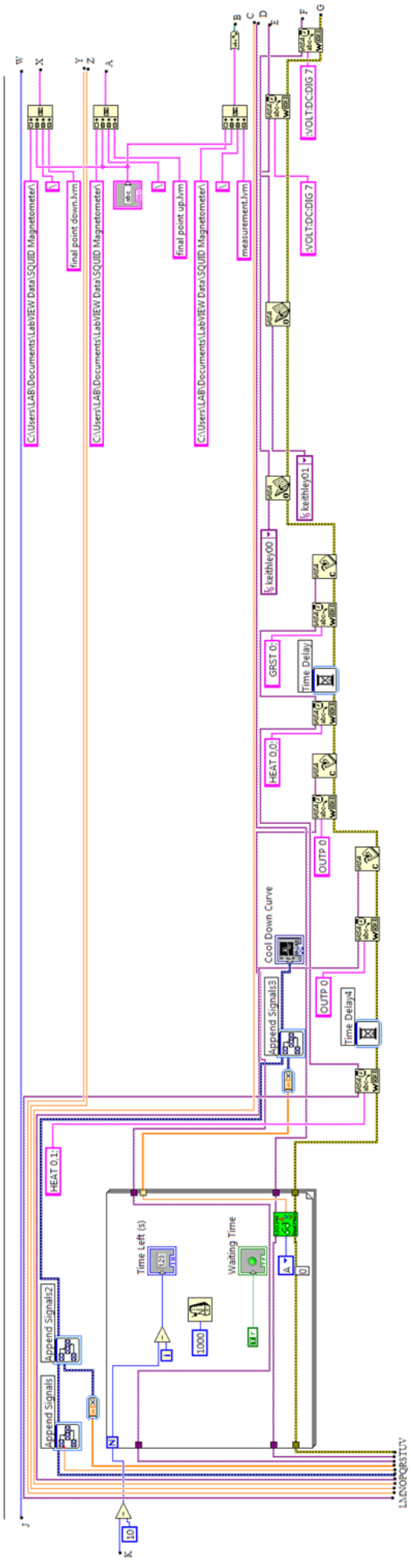
C:\Users\LAB\Documents\LabVIEW Data\SQUID Magnetometer\
final point down.lvm
final point up.lvm
measurement.lvm
VOLT:DC:DIG 7
keithley01
keithley00
GRST 0
Time Delay
HEAT 0.0
OUTP 0
Cool Down Curve
Append Signals3
Time Delay4
HEAT 0.1
Time Left (s)
Waiting Time
1000
Append Signals2
Append Signals

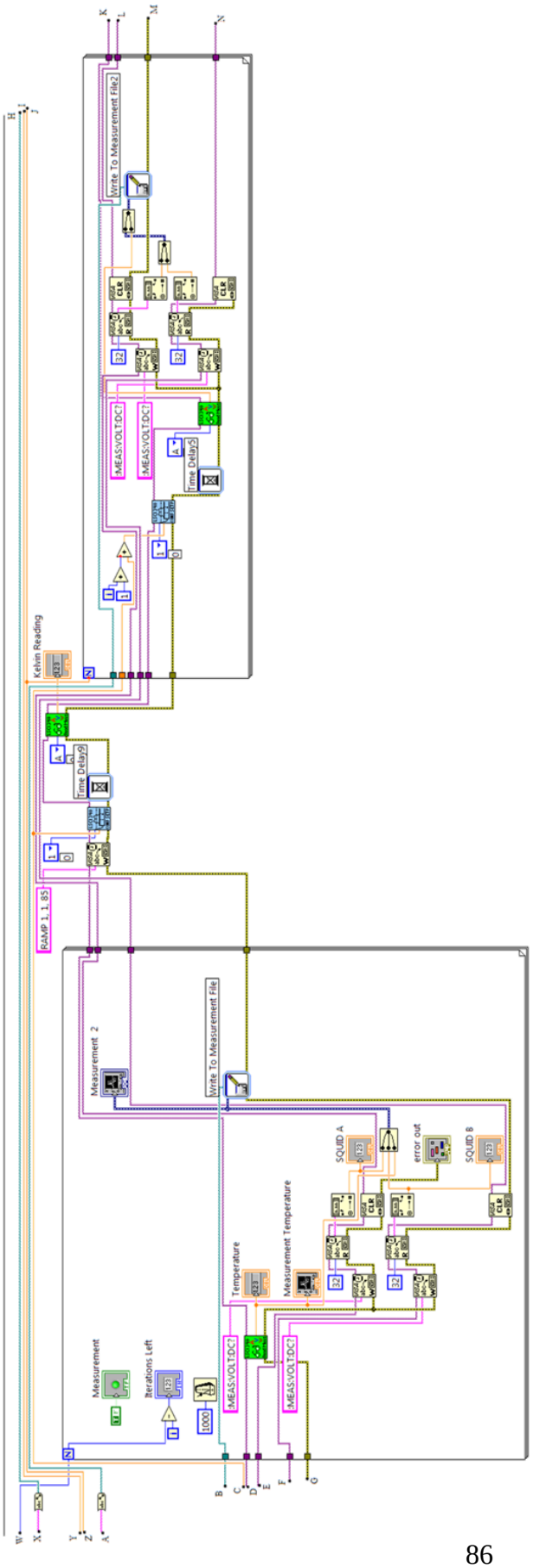
Write To Measurement File2
MEASVOLTDC?
MEASVOLTDC?
Time Delay5
Kelvin Reading
Time Delay6
RAMP 1, 1, 85
Measurement 2
Write To Measurement File
SQUID A
error out
SQUID B
Measurement Temperature
Temperature
Measurement
Iterations Left
1000
MEASVOLTDC?
MEASVOLTDC?

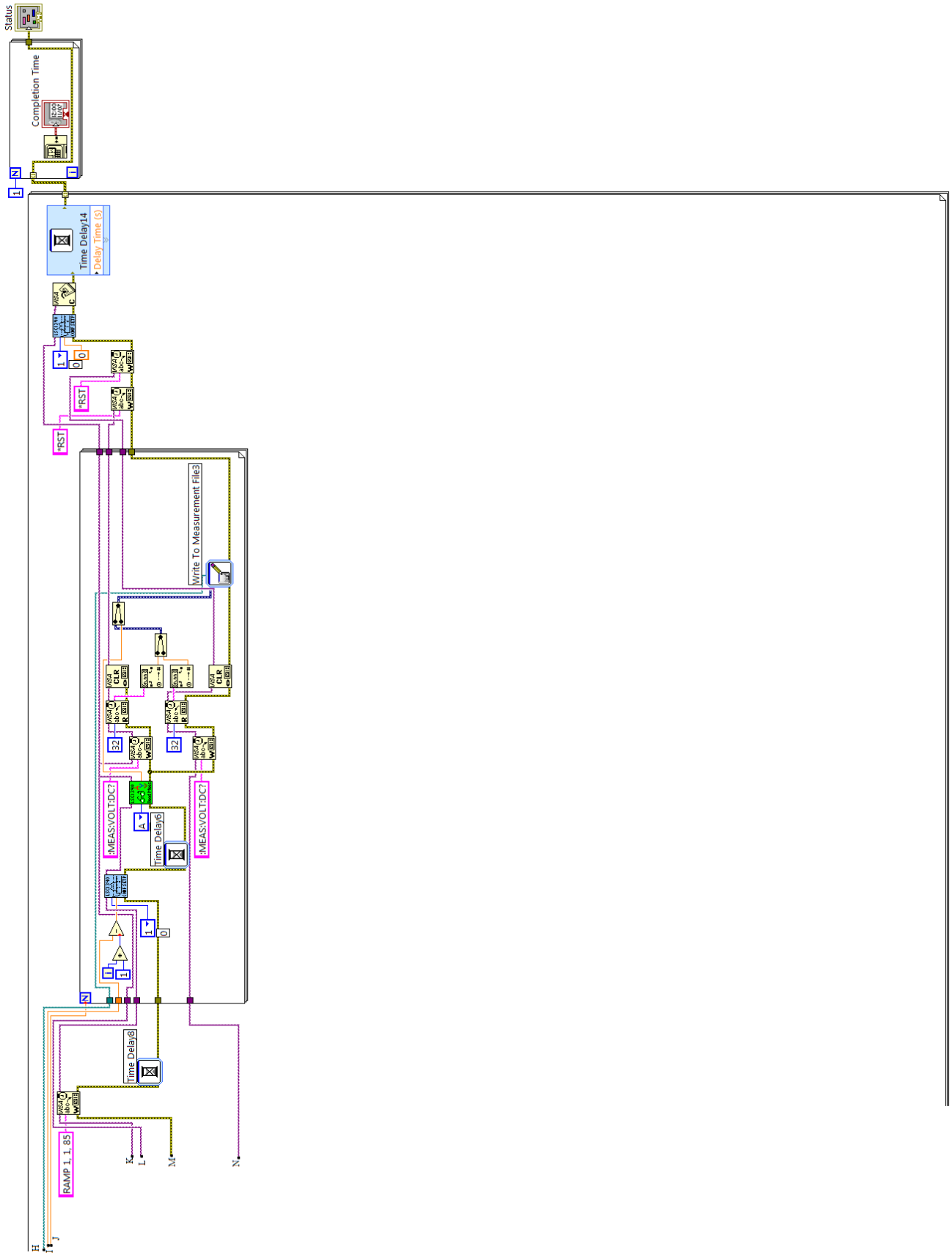
Status
Completion Time
Time Delay14
Delay Time (s)
RST
RST
Write To Measurement File3
MEAS:VOLT:DC?
MEAS:VOLT:DC?
Time Delay6
Time Delay8
RAMP 1.1 85
H
I
J
K
L
M
N

Part 2. DDSM Long-Time Measurement Program

The long-time ZTRM decay program is built to measure very long perioud of time with a zero waiting time protocol. The system can only run once per parameter set. Fig. B.2 spans pages 89 - 95.

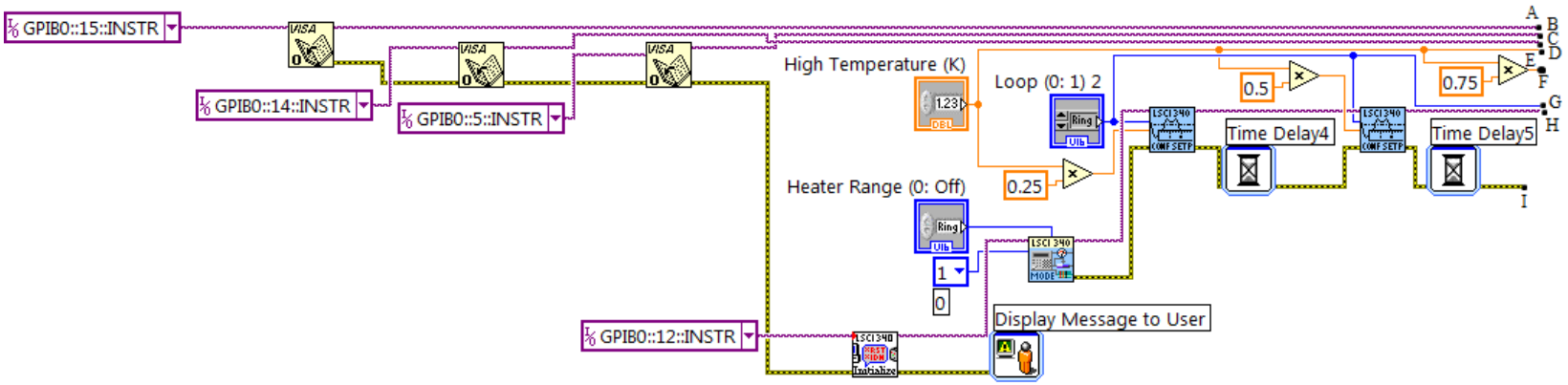
GPIB0::15::INSTR
GPIB0::14::INSTR
GPIB0::5::INSTR
GPIB0::12::INSTR
VISA
High Temperature (K)
Loop (0: 1) 2
Heater Range (0: Off)
0.5
0.75
0.25
Time Delay4
Time Delay5
Display Message to User
A
B
C
D
E
F
G
H
I

Tab Control

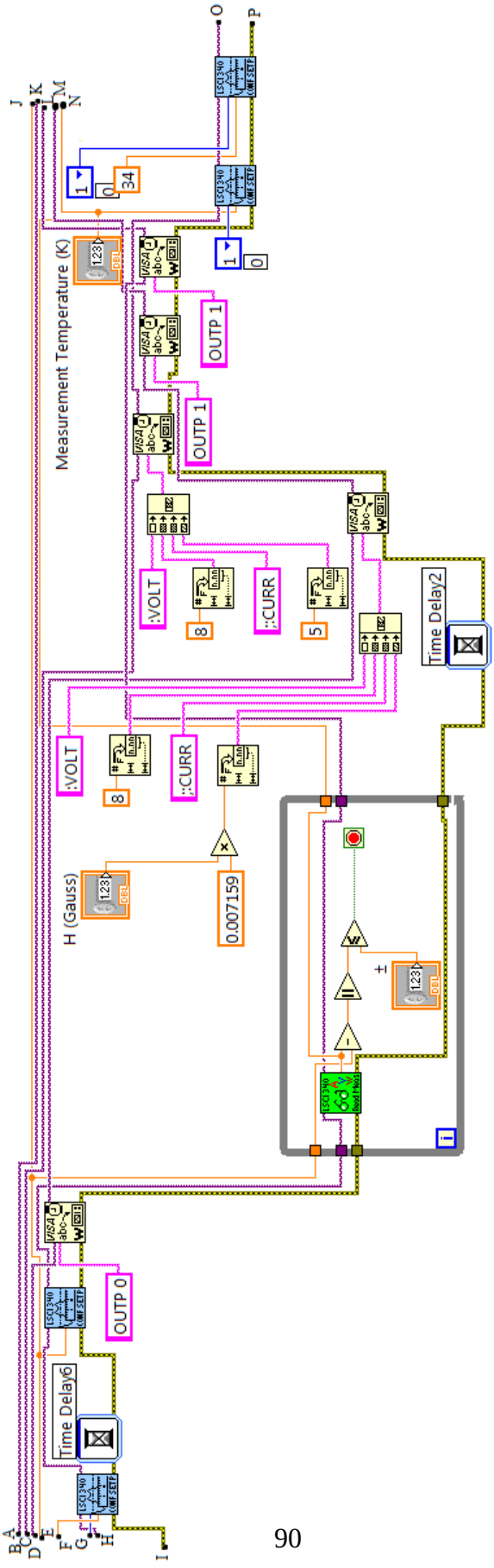
Measurement Temperature (K)
OUTP 1
OUTP 1
:VOLT
::CURR
5
8
Time Delay2
:VOLT
::CURR
8
H (Gauss)
0.007159
OUTP 0
Time Delay6
34
0

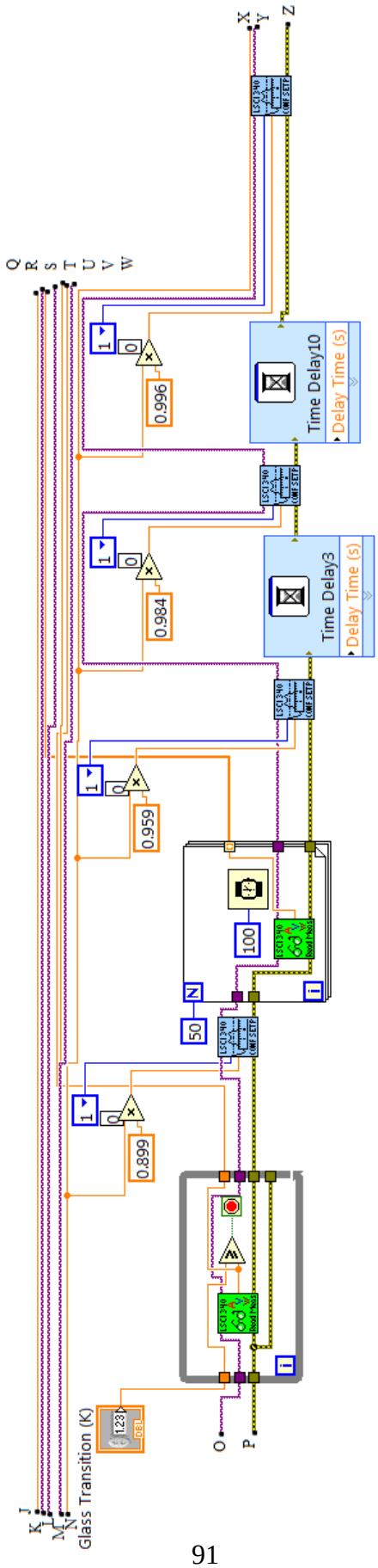
X
Y
Z
Q
R
S
T
U
V
W
Time Delay10
Delay Time (s)
Time Delay3
Delay Time (s)
0.996
0.984
0.959
0.899
100
50
Glass Transition (K)
O
P
J
K
L
M
N

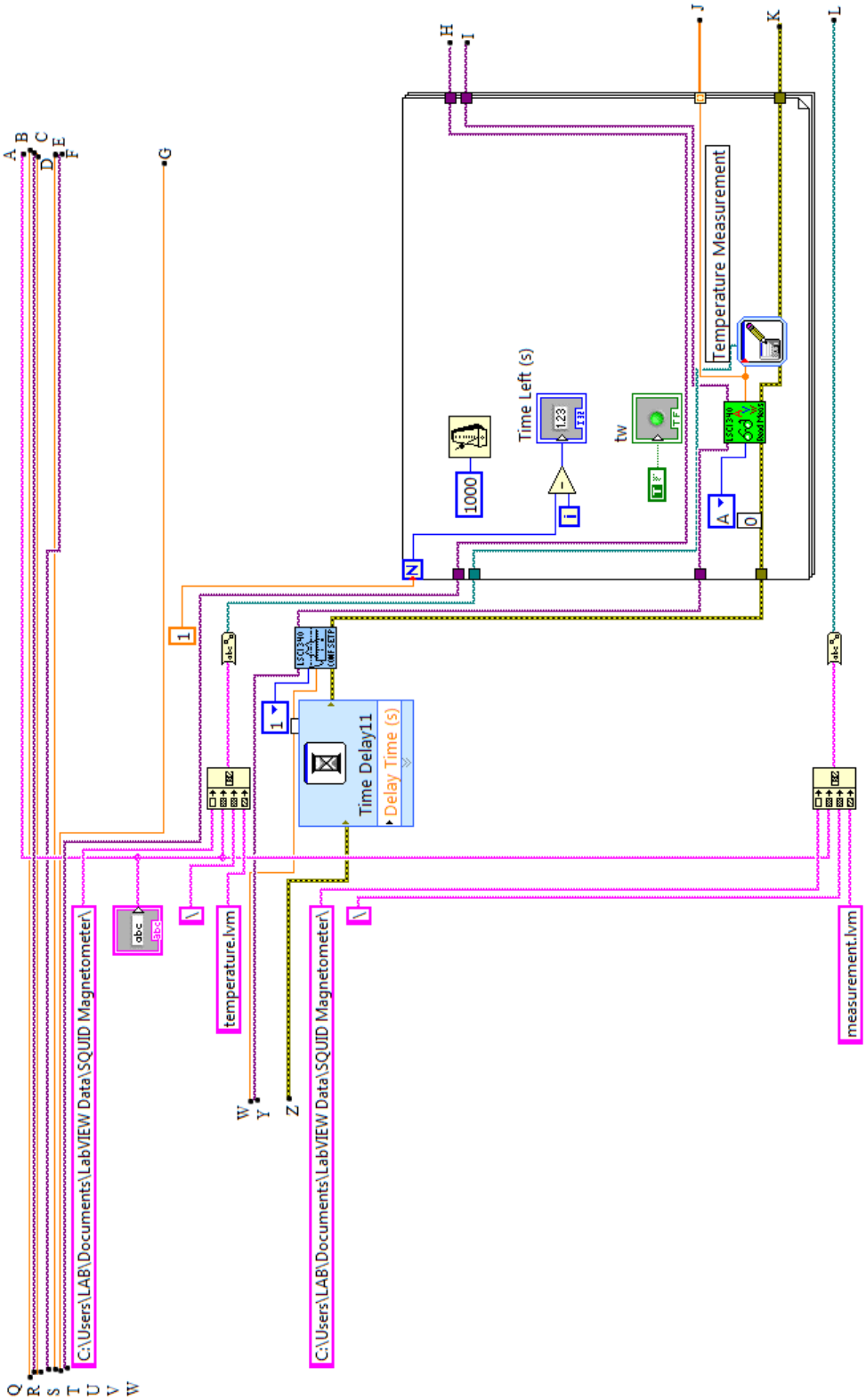
A
B
C
D
E
F
G
H
I
J
K
L
Q
R
S
T
U
V
W
W
Y
Z
Temperature Measurement
Time Left (s)
tw
1000
Time Delay11
Delay Time (s)
C:\Users\LAB\Documents\LabVIEW Data\SQUID Magnetometer\
temperature.lvm
C:\Users\LAB\Documents\LabVIEW Data\SQUID Magnetometer\
measurement.lvm

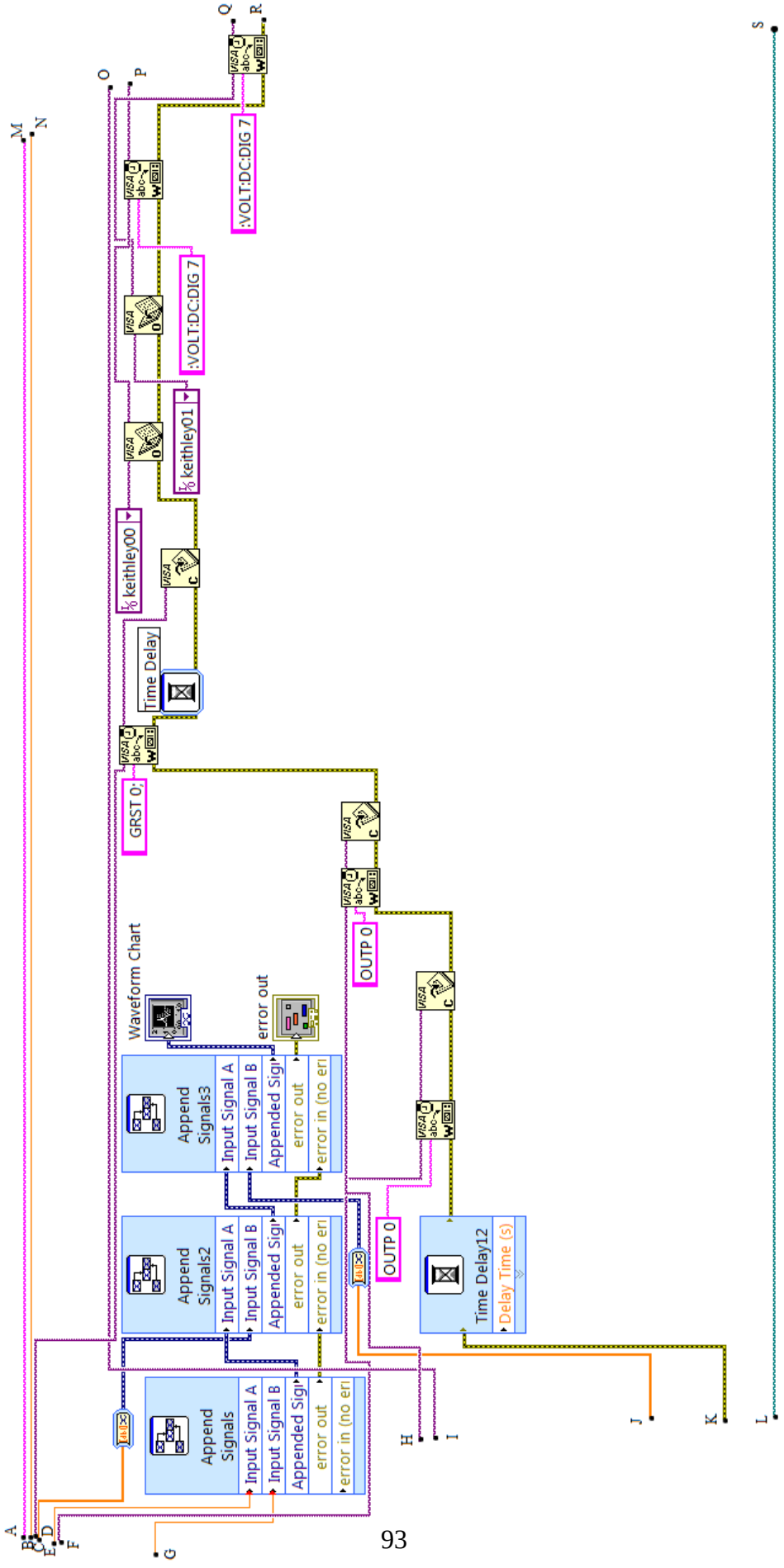
A
B
C
D
E
F
G
H
I
J
K
L
M
N
O
P
Q
R
S
:VOLT:DC:DIG 7
:VOLT:DC:DIG 7
keithley01
keithley00
Time Delay
GRST 0;
Waveform Chart
error out
OUTP 0
OUTP 0
Append Signals3
Append Signals2
Append Signals
Input Signal A
Input Signal B
Appended Sig
error out
error in (no err
Time Delay12
Delay Time (s)

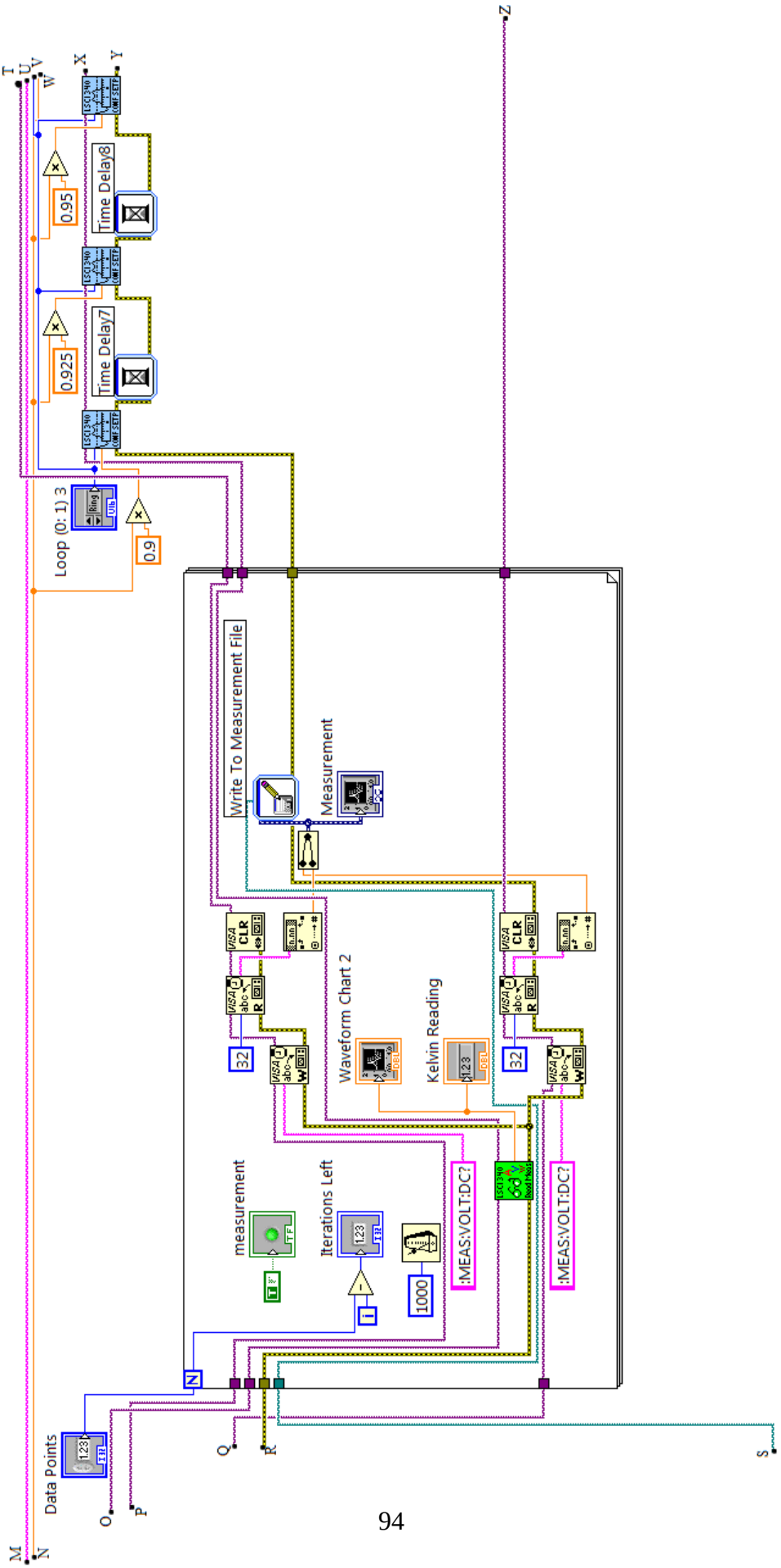
Time Delay8
Time Delay7
0.95
0.925
0.9
Loop (0: 1) 3
Write To Measurement File
Measurement
Waveform Chart 2
Kelvin Reading
measurement
Iterations Left
1000
:MEAS:VOLT:DC?
:MEAS:VOLT:DC?
Data Points
32
32

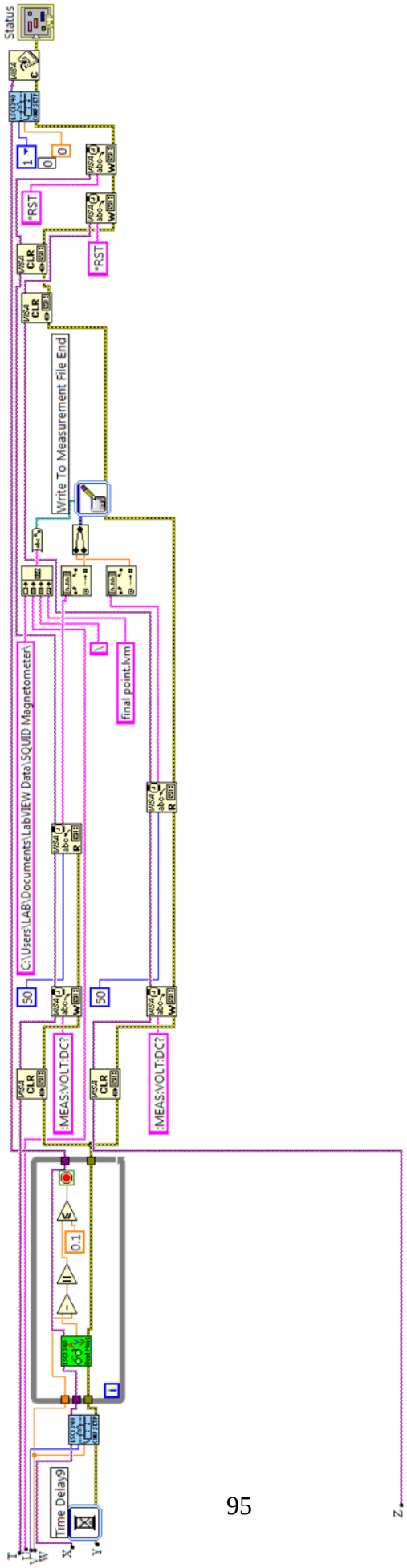
Status
*RST
*RST
Write To Measurement File End
final point.lvm
C:\Users\LAB\Documents\LabVIEW Data\SQUID Magnetometer\
50
50
:MEAS:VOLT:DC?
:MEAS:VOLT:DC?
0.1
Time Delay9